OPTICAL PROPERTIES OF ALN AND DEEP UV PHOTONIC STRUCTURES STUDIED BY PHOTOLUMINESCENCE

by

ASHOK SEDHAIN

B. Sc., Tribhuvan University, Nepal, 1998
M. Sc., Tribhuvan University, Nepal, 2001

AN ABSTRACT OF A DISSERTATION

submitted in partial fulfillment of the requirements for the degree

DOCTOR OF PHILOSOPHY

Department of Physics
College of Arts and Sciences

KANSAS STATE UNIVERSITY
Manhattan, Kansas

2011

Abstract

Time-resolved deep ultraviolet (DUV) Photoluminescence (PL) spectroscopy system has been employed to systematically monitor crystalline quality, identify the defects and impurities, and investigate the light emission mechanism in III-nitride semiconducting materials and photonic structures. A time correlated single photon counting system and streak camera with corresponding time resolutions of 20 and 2 ps, respectively, were utilized to study the carrier excitation and recombination dynamics. A closed cycle He-flow cryogenic system was employed for temperature dependent measurements. This system is able to handle sample temperatures in a wide range (from 10 to 900 K). Structural, electrical, and morphological properties of the material were monitored by x-ray diffraction (XRD), Hall-effect measurement, and atomic force microscopy (AFM), respectively. Most of the samples studied here were synthesized in our laboratory by metal organic chemical vapor deposition (MOCVD). Some samples were bulk AlN synthesized by our collaborators, which were also employed as substrates for homoepilayer growth.

High quality AlN epilayers with (0002) XRD linewidth as narrow as 50 arcsec and screw type dislocation density as low as $5x10^6$ cm^{-2} were grown on sapphire substrates. Free exciton transitions related to all valence bands (A, B, and C) were observed in AlN directly by PL, which allowed the evaluation of crystal field (Δ_{CF}) and spin-orbit (Δ_{SO}) splitting parameters exerimentally. Large negative Δ_{CF} and, consequently, the difficulties of light extraction from AlN and Al-rich AlGaN based emitters due to their unique optical polarization properties have been further confirmed with these new experimental data. Due to the ionic nature of III-nitrides, exciton-LO phonon Frohlich interaction is strong in these materials, which is manifested by the appearance of phonon replicas accompanying the excitonic emission lines in their PL spectra.

The strength of the exciton-phonon interactions in AlN has been investigated by measuring the Huang-Rhys factor. It compares the intensity of the zero phonon (exciton emission) line relative to its phonon replica.

AlN bulk single crystals, being promising native substrate for growing nitride based high quality device structures with much lower dislocation densities ($<10^4$ cm^{-2}), are also expected to be transparent in visible to UV region. However, available bulk AlN crystals always appear with an undesirable yellow or dark color. The mechanism of such undesired coloration has been investigated. MOCVD was utilized to deposit ~0.5 μm thick AlN layer on top of bulk crystal. The band gap of strain free AlN homoepilayers was 6.100 eV, which is ~30 meV lower compared to hetero-epitaxial layers on sapphire possessing compressive strain. Impurity incorporation was much lower in non-polar m-plane growth mode and the detected PL signal at 10 K was about an order of magnitude higher from a-plane homo-epilayers compared to that from polar c-plane epilayers.

The feasibility of using Be as an alternate p-type dopant in AlN has been studied. Preliminary studies indicate that the Be acceptor level in AlN is ~330 meV, which is about 200 meV shallower than the Mg level in AlN.

Understanding the optical and electronic properties of native point defects is the key to achieving good quality material and improving overall device performance. A more complete picture of optical transitions in AlN and GaN has been reported, which supplements the understanding of impurity transitions in AlGaN alloys described in previous reports.

OPTICAL PROPERTIES OF ALN AND DEEP UV PHOTONIC STRUCTURES STUDIED BY PHOTOLUMINESCENCE

by

ASHOK SEDHAIN

B. Sc., Tribhuvan University, Nepal, 1998
M. Sc., Tribhuvan University, Nepal, 2001

A DISSERTATION

submitted in partial fulfillment of the requirements for the degree

DOCTOR OF PHILOSOPHY

Department of Physics
College of Arts and Sciences

KANSAS STATE UNIVERSITY
Manhattan, Kansas

2011

Approved by:

Major Professor
Jingyu Lin

Abstract

Time-resolved deep ultraviolet (DUV) Photoluminescence (PL) spectroscopy system has been employed to systematically monitor crystalline quality, identify the defects and impurities, and investigate the light emission mechanism in III-nitride semiconducting materials and photonic structures. A time correlated single photon counting system and streak camera with corresponding time resolutions of 20 and 2 ps, respectively, were utilized to study the carrier excitation and recombination dynamics. A closed cycle He-flow cryogenic system was employed for temperature dependent measurements. This system is able to handle sample temperatures in a wide range (from 10 to 900 K). Structural, electrical, and morphological properties of the material were monitored by x-ray diffraction (XRD), Hall-effect measurement, and atomic force microscopy (AFM), respectively. Most of the samples studied here were synthesized in our laboratory by metal organic chemical vapor deposition (MOCVD). Some samples were bulk AlN synthesized by our collaborators, which were also employed as substrates for homoepilayers.

High quality AlN epilayers with (0002) XRD linewidth as narrow as 50 arcsec and screw type dislocation density as low as 5×10^{6} cm^{-2} were grown on sapphire substrates. Free exciton transitions related to all valence bands (A, B, and C) were observed in AlN directly by PL, which allowed the evaluation of crystal field (Δ_{CF}) and spin-orbit (Δ_{SO}) splitting parameters exerimentally. Large negative Δ_{CF} and, consequently, the difficulties of light extraction from AlN and Al-rich AlGaN based emitters due to their unique optical polarization properties have been further confirmed with these new experimental data. Due to the ionic nature of III-nitrides, exciton-LO phonon Frohlich interaction is strong in these materials, which is manifested by the appearance of phonon replicas accompanying the excitonic emission lines in their PL spectra. The strength of the exciton-phonon interactions in AlN has been investigated by measuring the

Huang-Rhys factor. It compares the intensity of the zero phonon (exciton emission) line relative to its phonon replica.

AlN bulk single crystals, being promising native substrate for growing nitride based high quality device structures with much lower dislocation densities ($<10^4$ cm^{-2}), are also expected to be transparent in visible to UV region. However, available bulk AlN crystals always appear with an undesirable yellow or dark color. The mechanism of such undesired coloration has been investigated. MOCVD was utilized to deposit ~0.5 μm thick AlN layer on top of bulk crystal. The band gap of strain free AlN homoepilayers was 6.100 eV, which is ~30 meV lower compared to hetero-epitaxial layers on sapphire possessing compressive strain. Impurity incorporation was much lower in non-polar m-plane growth mode and the detected PL signal at 10 K was about an order of magnitude higher from a-plane homo-epilayers compared to that from polar c-plane epilayers.

The feasibility of using Be as an alternate p-type dopant in AlN has been studied. Preliminary studies indicate that the Be acceptor level in AlN is ~330 meV, which is about 200 meV shallower than the Mg level in AlN.

Understanding the optical and electronic properties of native point defects is the key to achieving good quality material and improving overall device performance. A more complete picture of optical transitions in AlN and GaN has been reported, which supplements the understanding of impurity transitions in AlGaN alloys described in previous reports.

Table of Contents

List of Figures ... ix

List of Tables ... xiv

Acknowledgements ... xv

Dedication ... xvii

Chapter 1 - Introduction ... 1

1.1 Brief overview of III-nitride materials and devices ... 1

1.2 AlN and Al-rich AlGaN alloys for deep UV photonics ... 4

1.3 AlN band structure ... 8

1.4 Substrate issue in deep UV photonics ... 12

1.5 Formation and optical properties of native point defects in AlN and AlGaN alloys ... 15

1.6 P-type doping issue in AlN and Al-rich AlGaN alloys ... 18

1.7 III-nitrides on non-polar and semi-polar substrates ... 20

1.8 Overview of the thesis ... 22

Chapter 2 – Experimental facilities ... 23

2.1 Deep UV time-resolved photoluminescence system for optical studies ... 23

2.1.1 Ultrafast laser system ... 23

2.1.1.1 Pump laser ... 25

2.1.1.2 Ti-sapphire laser ... 25

2.1.2 Super Quadrupler ... 26

2.1.3 Detection systems ... 28

2.1.3.1 Monochromator ... 28

2.1.3.2 Time-correlated single photon counting ... 29

2.1.3.3 Streak camera ... 33

2.1.4 Cryogenic system ... 35

2.2 Material synthesis by MOCVD ... 37

2.3 Characterization tools ... 38

2.3.1 Optical Microscope ... 38

2.3.2 Atomic force microscope (AFM) ... 39

2.3.3 X-ray diffraction (XRD) ... 40

2.3.4 Photoluminescence (PL) 43
2.3.5 Secondary ion mass spectroscopy (SIMS) 44
Chapter 3 – Experimental Results and Discussions 46
3.1 Valence band structure of AlN probed by photoluminescence 46
3.2 Photoluminescence properties of AlN homoepilayers 56
3.3 Beryllium acceptor in AlN 67
3.4 Probing exciton-phonon interaction in AlN by photoluminescence 76
3.5 Origin of 2.78 eV PL emission and yellow coloration in bulk AlN 85
3.6 Nature of deep center emissions in GaN 98
Chapter 4 – General Conclusion 108
Chapter 5 – References 111
Appendix A - Publications 123

List of Figures

Figure 1.1 Energy bandgap (left scale) and corresponding wavelengths (right) of AlGaN alloys as function of Al-content (x) 5

Figure 1.2 Maximum external quantum efficiencies (EQE) of III-nitride based UV emitters observed at various laboratories worldwide (Ref. 10,11,29) 6

Figure 1.3 Schematic band structure diagram of AlN showing the crystal-field and the spin-orbit splittings on top of the valence band at Γ-point. Band structure for GaN is also included for comparision 10

Figure 1.4 Output power of UV LEDs at 50 mA drive current with GaN active layer on various AlGaN with different dislocation densities (Ref. 35) 13

Figure 1.5 Carrier concentration and mobility of a Si-doped n-type $Al_{0.34}Ga_{0.66}N$ as functions of dislocation density measured at room temperature (Ref. 36) 14

Figure 1.6 Formation energies of various native point defects and their complexes in AlN plotted as functions of the fermi level position (Ref. 41) 16

Figure 1.7 Deep acceptor levels of $(V_{III}\text{-complex})^{1-}$(black squares), $(V_{III}\text{-complex})^{2-}$ (gray quares), and V_{III}^{3-} (open circles) plotted together with E_c, E_v, as functions of Al content (x) (Ref. 45) 17

Figure 1.8 Schematic diagram showing the donor levels of nitrogen vacancies (V_N^{3+} and V_N^{1+}) and acceptor levels of Be^0, Mg^0, Zn^0, and C^0 in AlN. 19

Figure 1.9 Schematic diagram showing the band bending in polar c-plane AlGaN/GaN QW (left) and no band bending in similar QW in non-polar orientation (right) (Ref. 53) 21

Figure 2.1 Experimental setup of time-resolved PL spectroscopy system with detection capability from deep UV to IR (185 nm-3 μm) intergrated with the NSOM system (Ref. 67) 24

Figure 2.2 Schematic block diadram of single photon counting system (Ref. 56)....................... 30

Figure 2.3 Schematic representation showing the single photon pulses separated from noise background with adjustable discriminator threshold (Ref. 56)................................... 31

Figure 2.4 Schematics of the photon pulse (TAC Start signal) and the reference laser pulse (TAC stop signal) in reversed start-stop mode (Ref. 56)... 32

Figure 2.5 System response (gray circles) and temporal profiles of donor-bound exciton transition (I_2) in AlN recorded with single photon counting system... 33

Figure 2.6 Streak image of the bandedge transition in an AlN bulk crystal measured at low temperature (10 K) 34

Figure 2.7 AFM images of AlN epilayers with different concentrations of oxygen impurity (N_O) for a 2 μm x 2 μm scan area 40

Figure 2.8 XRD rocking curves measured on symmetric (002) and asymmetric (102) planes of AlN epilayer 42

Figure 2.9 Room temperature (300 K) PL spectra of undoped- (top) and Si-doped (bottom) AlN epilayers.. 43

Figure 2.10 SIMS results showing the depth profiles of O (blue line) and C (black lines) in AlN epilayer 45

Figure 3.1 Low temperature (10 K) PL spectra of an AlN epilayer measured under different polarization configurations with (a) **E||c** and (b) **E⊥c**. Schematic diagram of the measurement setup is shown in the inset of (a)... 48

Figure 3.2 Low temperature PL spectra of an AlN eppilayer for **E⊥c** polarization in narrow spectral range.. 51

Figure 3.3 Energy level diagram of AlN near the Γ-point constructed from the low temperature PL results 53

Figure 3.4 Low temperature (10 K) PL spectra of c-plane, a-plane, and m-plane AlN homoepilayers measured in a (a) wide spectral range from 2 to 6.2 eV and (b) narrow spectral range from 5.8 to 6.2 eV 58-59

Figure 3.5 The Arrhenious plot of the PL intensity [Ln (I_{emi}) vs 1/T] of free exciton transition (6.025 eV at 10 K) for a-plane AlN homoepilayer. The solid line is the least square fit of the data with Eq. (1). The inset shows the temperature dependence of the band-edge emission between 100 and 300 K 61

Figure 3.6 Low temperature (10 K) PL spectra of c-AlN/c-Al_2O_3, a-AlN/r-Al_2O_3 and a-plane AlN homo-epilayer measured in a (a) wide spectral range from 2 to 6.2 eV and (b) narrow spectral range from 5.8 to 6.2 eV 64-65

Figure 3.7 Low temperature (10 K) PL spectra of undoped, Mg doped and Be doped AlN epilayers measured in a (a) wider spectral range from 2 to 6.2 eV and (b) narrower spectral range from 5.8 to 6.2 eV 70

Figure 3.8 Temperature dependence of the I_1 transition in Be doped AlN epilayers measured from 10 to 300 K 72

Figure 3.9 The Arrhenius plot of the PL intensity [Ln (I_{emi}) vs 1/T] of the I_1 transition (6.03 eV at 10 K) for Be doped AlN epilayers. The solid line represents the least square fit of the data with Eq. (1) 73

Figure 3.10 Temporal responses of the I_1 transition in (a) Mg and (b) Be doped AlN epilayer measured at 10 K. Measured decay lifetimes were 119 and 93 ps for Mg and Be doped AlN epilayers, respectively 75

Figure 3.11 Low temperature (10 K) PL spectra of an AlN hetero-epilayer collected with the polarization of emitted light (a) parallel ($\vec{E} \parallel \vec{c}$) and (b) perpendicular ($\vec{E} \perp \vec{c}$) to the crystallographic c-axis 79

Figure 3.12 Normalized PL intensities of nth order phonon replicas with respect to the zero phonon line measured in an AlN hetero-epilayer in two different polarization configurations 80

Figure 3.13 Low temperature (10 K) PL spectra of (a) an AlN hetero-epilayer grown on sapphire and (b) an AlN homoepilayer grown on bulk AlN substrate 83

Figure 3.14 (a) Room temperature (300 K) and (b) low temperature (10 K) PL spectra of AlN hetero-epilayer, polycrystalline AlN, and AlN bulk single crystal under above band-gap excitation scheme with 197 nm laser 87-88

Figure 3.15 Low temperature (10 K) PL spectra of AlN hetero-epilayer, polycrystalline AlN, and AlN bulk single crystal under: (a) above (197 nm) and (b) below (262 nm) band gap excitation 89-90

Figure 3.16 (a) Temperature dependent PL spectra of m-AlN bulk around 2.78 eV with 262 nm excitation from 10 to 400 K. (b) The Arrhenius plot of the PL intensity of 2.78 eV emission line in m-AlN bulk 91-92

Figure 3.17 (a) Excitation intensity dependent PL spectra measured on m-AlN bulk single crystal around 2.73 eV emission line with 197 nm excitation. (b) Peak emission intensity at 2.73 eV as a function of excitation intensity 94

Figure 3.18 Energy level diagram of AlN including two charge states, V_{Al}^{3-} and V_{Al}^{2-}, of $V_{Al}^{3-/2-}$ defect with a small lattice relaxation (SLR) between these two states 96

Figure 3.19(a) 300 K and (b) 150 K PL spectra of unintentionally doped n-GaN epilayer in the IR spectral region 100

Figure 3.20(a) Excitation intensity (I_{exc}) dependent PL spectra of GaN around 1.23 eV at 300 K and (b) PL emission intensity (I_{emi}) as a function of I_{exc} (solid squares) and least squares fit of data with $I_{emi} = aI_{exc}^{\beta}$ (solid line) 101-102

Figure 3.21 Room temperature PL spectra of unintentionally doped n-GaN epilayer in UV and visible spectral regions 103

Figure 3.22(a) Atomic geometries of the $(V_{Ga}\text{-}O_N)^{2-/1-}$ complex in GaN for oxygen replacing the nitrogen from (a) π-bonding (along c-axis) and (b) σ-bonding (one of the other three equivalent positions). (b) Energy level diagram of GaN including the charge states $(V_{Ga}\text{-}O_N)^{2-}$ and $(V_{Ga}\text{-}O_N)^{1-}$ of $(V_{Ga}\text{-}O_N)^{2-/1-}$ center. SLR stands for small lattice relaxation 104-105

List of Tables

Table 1.1 A brief summary of interesting properties of AlN and its technological importance..... 2

Table 1.2 Material properties of AlN and GaN 11

Table 3.1Theoretically calculated and experimentally observed spin-orbit splitting parameter (Δ_{SO}), Crystal-field splitting parameter (Δ_{CR}), energy spacing between the A and B valence bands (E_{AB}), and the B and C valence bands (E_{BC}) in WZ AlN 54

Table 3.2Comparision of PL emission properties of a-, c-, and m-plane AlN homo-epilayers, c-AlN/c-Al_2O_3, and a-AlN/r-Al_2O_3 hetero-epilayers including PL peak position (E_p), PL peak intensity (I_p), full width at half maximum (FWHM), and binding energy (BE) at 10 K and 300 K 63

Acknowledgements

First of all, I owe my deepest gratitude to my supervising advisors Professor Jingyu Lin and Professor Hongxing Jiang for their persistent encouragement and the guidance thoroughout the course of this work. Through their depth of knowledge and the stimulating way to approach the research problems, I am priviledged to develop the quality of an independent scientist within myself.

It is my pleasure to thank Prof. Michael J. O'Shea and Prof. James H. Edgar for kindly agreeing to serve as the members of my supervisory committee and Prof. Stephen A. Dyer as the chairperson.

It is an honor for me to thank Dr. Neeraj Nepal, who has taught me a great deal on using the experimental facilities in this laboratory. Many thanks are due to Dr. Jing Li and Dr. Talal Al Tahtamouni for sharing the MOCVD grown samples, providing valuable information, and having insightful discussions. I would like to thank all the former and current members of my research group including Dr. Zhaoyang Fan, Dr. Sixuan Jin, Dr. Mim Lal Nakarmi, Dr. Cris Ugolini, Dr. Neelam Khan, Dr. Bed Nidhi Pantha, Dr. Rajendra Dahal, Mrs. Weiping Zhao, and Ms. I-Wen Feng for their help, feedback, and moral support. I would also like to thank Mr. Frank Jiang for his time and effort in proof-reading this thesis.

I acknowledge the Physics department at Kansas State University for providing me this opportunity to pursue my graduate studies and the financial support for the same. Thanks to Electrical and Computer Engineering department, Texas Tech University as well for providing me the internship to complete the last part of this thesis.

Last but not least; I thank to my parents Til Kumari Sedhain (aama) and Chandra Kanta Sedhain (buwa) for continuous love, support and encouragement. I am grateful to my wife, Samjhana, and son, Shrijan, for being constant sources of inspiration.

Dedication

To my loving parents Til Kumari and Chandra Kanta, wonderful wife Samjhana, and lovely son Shrijan.

Chapter 1 - Introduction

1.1 Brief overview of III-nitride materials and devices

The nitrides of group III metals (Al, Ga, and In) and their ternary/quaternary alloys have emerged as important semiconductor materials in various applications partly due to their direct bandgaps: ~0.7 eV in InN [1] to 3.4 eV in GaN [2] and 6.1 eV in AlN [3]. The invention of low temperature (LT) buffer technology [4-6] has successfully enabled lower background electron concentration and allowed for the realization of p-type conductivity in GaN [7,8] after 1980's. GaN based current injection near ultraviolet (UV) laser diode has been commercialized and employed in various applications such as blue ray DVD for high density optical data storage capacity. In 2002, the bandgap of InN was reviewed and a much lower (~0.7 eV) than the previously assumed value (~1.9 eV) has been suggested [1]. In addition to its conventional application in light emitting devices, the finely tunable energy gap of InGaN alloys, which covers the entire solar spectrum, has made InGaN alloys a very promising material system for energy generation, such as photovoltaics, photoelectrochemical cells, and thermoelectricity. Aluminum nitride (AlN) and Al-rich AlGaN alloys have emerged as promising materials for deep UV (DUV) photonics [9-11]. In addition, AlN seems to be the most promising substrate material for producing III-nitride UV/DUV photonic devices and high power/high temperature radio frequency devices [12,13].

In the last 10 years, AlN and Al-rich AlGaN alloys have attracted tremendous research interest due to their application in UV and DUV photonic devices, such as light emitting diodes (LEDs) and laser diodes (LDs) with operating wavelengths as short as ~207 nm and solar blind photodetectors. The outstanding physical properties of $Al_xGa_{1-x}N$ alloys include wide bandgap,

high breakdown voltage, and high saturation velocity. All of these properties are advantageous for delivering high speed and high power electronic devices capable of operating in harsh environment. Single crystal AlN is an ideal choice as a substrate for III-nitride due to its good thermal stability (melting point ~3000 K), high thermal conductivity and electrical resistivity, deep UV transparency, similar coefficient of thermal expansion, and only a small lattice constant mismatch with GaN. Its high surface acoustic wave (SAW) propagation velocity (~5800 ms^{-1})

Table 1.1 A brief summary of interesting properties of AlN and its technological importance.

Property of AlN	Potential Application	Competing Technology	Why AlN ?
E_g = 6.1 eV (direct) τ_{FX} = 50 ps Ability to form alloy	AlGaN based DUV emitter	Hg lamps	Miniaturized size, environmentally friendly, power efficient, and finely tunable λ
Hardness Resistant to high T, chemicals, & radiation	DUV Photodetector	Si-detectors	Better for space application • No cooling hardware & optical filter required • Light weight, durable High DUV/visible rejection
κ =319 $Wm^{-1}K^{-1}$ Low $\Delta\alpha/\alpha$ and $\Delta a/a$ Transparent to DUV	Substrate for III-nitrides (AlGaN)	Al_2O_3, SiC, Si, GaN	Improved device performance and lifetime: • Better heat management • Reduced dislocations
ϕ~negative (or low) Highly stable, Low α	Cold cathode (Field emitter)	Thermionic emitters	Low E_{TO} (1.8 V/μm) High β (3271)
V_{SAW}= 5700 ms^{-1} Piezoelectric, K^2= 0.65	SAW devices	Quartz $LiNbO_3$	Easy to make GHz band device Superior stop-band rejection Low loss, suitable for high T

and large piezoelectric constant e_{33} (1.5 C/m^2) [14,15] leading to an excellent electromechanical coupling constant K^2 make AlN suitable for SAW devices. The conduction band electron in AlN can be ejected easily into vacuum due to its low work function, which has made it possible to use as a cold cathode in various applications including commercial field emission display (FED). Table 1.1 briefly summarizes the technological importance of AlN.

Even though the first synthesis of AlN was reported in 1907 [16], epilayer growth began only after Manasevit *et al* synthesized GaN by metal organic chemical vapor deposition (MOCVD) in 1971. Slack and McNelly developed the sublimation-recondensation method [17] in 1976 for growing bulk single crystals with a high growth rate of 0.5-1.0 mm/hr. Single crystal AlN is typically grown by high temperature (>1800 ^{0}C) sublimation of sintered AlN powder. For the thin film growth, there are two methods in common use. The chemical reaction of ammonia with metal organic (MO) source (e.g. trimethylaluminum, TMAl) is utilized in MOCVD growth [18-20]. MOCVD method provides a good control over the growth parameter and the deposition temperature is relatively low (~1200 ^{0}C). Molecular beam epitaxy (MBE) is an alternative way currently being used to grow thin layers [21-23]. Due to the unavailability of native substrates, growth of these materials relied on foreign substrates, such as Al_2O_3, SiC, Si etc. It leads to dislocations and grain boundary formation due to large lattice and thermal expansion coefficient mismatch between the epilayer and substrate.

Early AlN crystals were optically characterized by measuring the fundamental absorption edge, which indicated that AlN is a direct gap material with room temperature bandgap of ~6.2 eV [24]. X-ray diffraction measurement is utilized in order to monitor the crystal quality, estimate the threading dislocation (TD), and determine the alloy composition (x) in $Al_xGa_{1-x}N$ alloys. Even though, XRD and energy dispersive x-ray (EDX) are good for elemental analysis,

secondary ion mass spectroscopy (SIMS) is preferred for precisely determining the concentration of elements present in small fractions, which may be <1% in most cases of doping or unintentionally incorporated foreign impurities. Hall-effect measurement is widely used to characterize the electrical properties, such as conductivity type, carrier concentration, resistivity, and mobility. However, the highly resistive nature of undoped and Mg-doped AlN and Al-rich AlGaN alloys causes very limited (if any) use of electrical characterization of these materials. Optical studies and the time resolved photoluminescence (TR PL) in particular, have become critically important for testing the crystalline quality of these ultra-large bandgap materials. The presence of native point defects are recognized by measuring relative intensities of near band edge (NBE) to impurity emissions and their decay lifetimes. Other optical characterization methods include absorption, reflectance, transmission, and cathodoluminescence (CL) measurements.

1.2 AlN and Al-rich AlGaN alloys for deep UV photonics

UV and DUV light sources are crucially important for various applications such as water/air purification, medical tools sterilization, bio-agent detection for research and national security, identification of sensitive documents, spectroscopic studies, general and special lighting etc. However, the conventional UV light sources, mercury lamps, are bulky, expensive, and have only a few discrete emission lines in this spectral region. In addition, mercury lamps are toxic, produce ozone and hazardous waste, and require relatively high voltage to operate. In contrast, wide-bandgap materials, such as diamond and AlGaN alloys are highly promising for these applications. III-nitride semiconductor based DUV LED technology offers any desired emission wavelength down to 200 nm by selecting the proper AlN/GaN mole fraction in the active AlGaN layer as clearly demonstrated in Al-content dependent bandgap in Fig. 1.1. AlGaN based UV

LEDs are miniaturized in size, do not produce any toxic elements or hazardous waste, and use low voltage (6-12 Volts). Very fast response time (nanoseconds or even faster), longer lifetime (100,000 vs 8,000 hours of Hg lamp), and their easy integration into a chip are advantageous, which have made it possible for LED technology to go beyond replacing mercury lamps and make even new applications feasible.

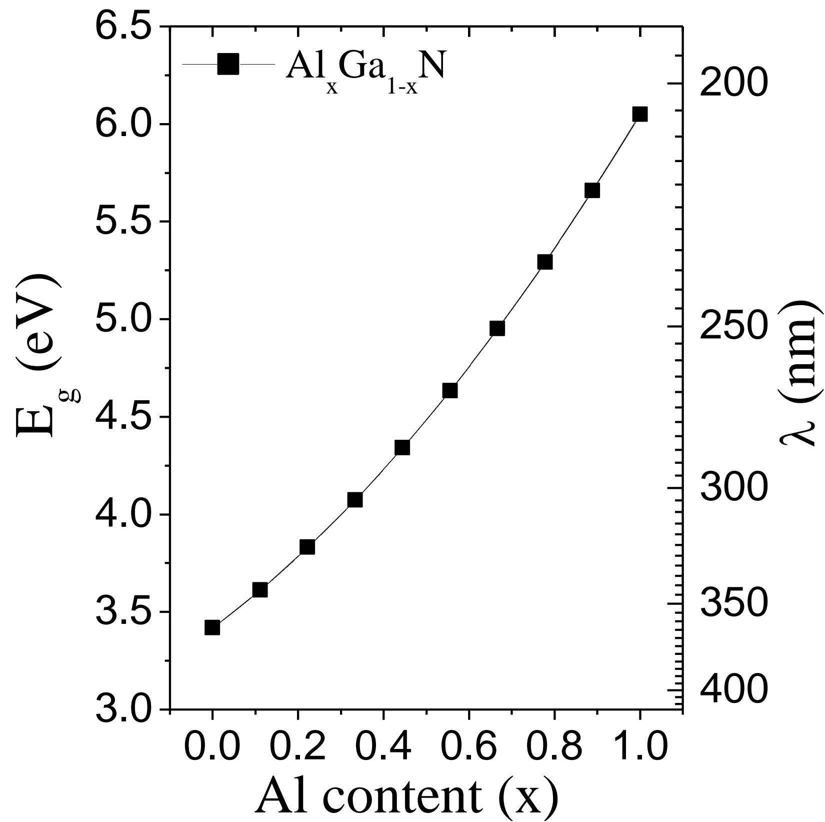

Fig. 1.1 Energy bandgap (left scale) and corresponding wavelengths (right scale) of AlGaN alloys as functions of Al-content (x).

Significant progress is being made in improving the material quality of AlN and Al-rich AlGaN alloys and optimization of their device structures. Light output power of ~1-2 mW is generally achieved around 270 nm with 20 mA driving current [25-28]. External quantum

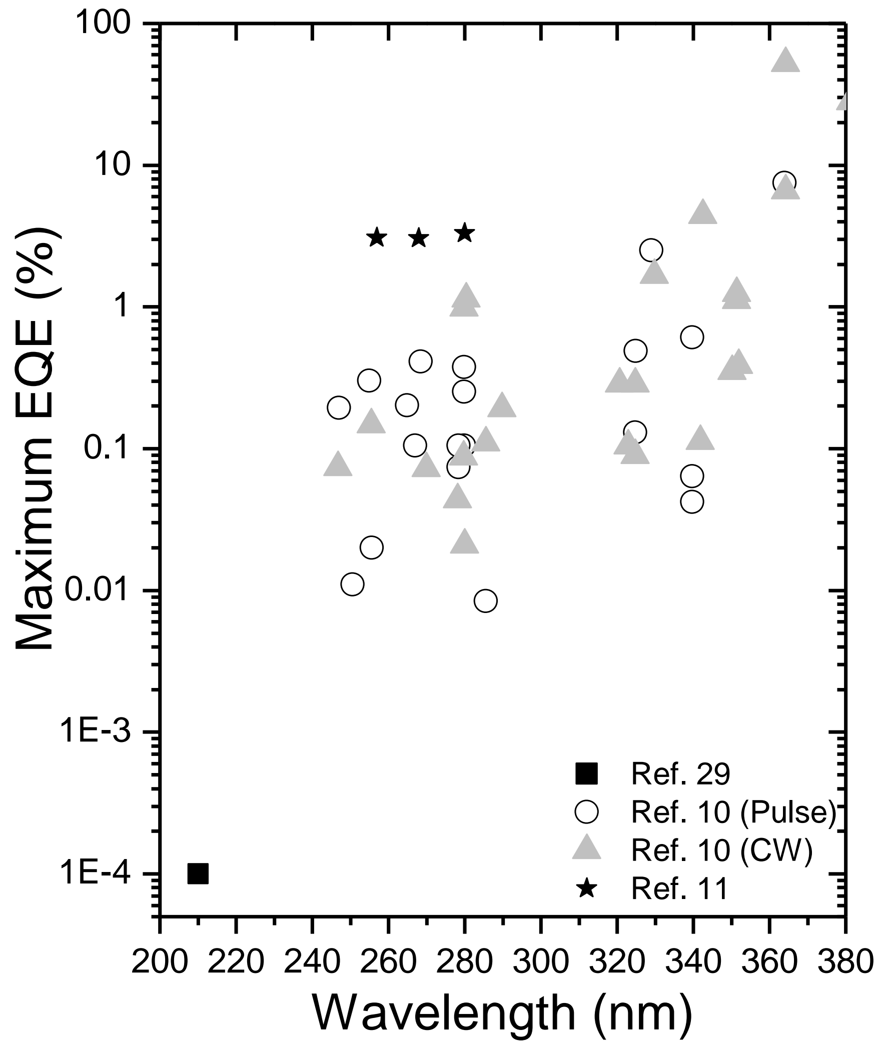

Fig. 1.2 Maximum external quantum efficiencies (EQE) of III-nitride based UV emitters observed at various laboratories worldwide (Refs. 10,11,29).

efficiencies (EQE) of 6.7% for 345 nm LEDs [30] and close to 3% for 255-285 nm LEDs [11,25,28] have been reported. However, for DUV LEDs emitting in 200-255 nm wavelength range, EQE remains well below 2%. EQE decreases dramatically with decreasing wavelength, as shown in Fig. 1.2. Since a single UV LED chip typically produces an output power of around 1-1.5 mW, applications requiring high power utilize multiple chip lamps. The highest CW power of a 280 nm multi-chip LED is more than 50 mW at 700 mA current. The characteristic switching time of these devices is on the order of a nanosecond, which allows for modulation frequencies up to 1 GHz or higher. Recently, the maximum CW optical power of 30 and 6 mW was achieved from single chip deep UV LEDs emitting at 273 and 247 nm, respectively, by fabricating the large chip devices with junction area up to 1 mm^2 [31]. These DUV LEDs have found some applications, such as all-LED spectrometers in >250 nm wavelengths, water purification units, and personal UV sterilization pens [32] etc. More than one order of magnitude improvement is expected in the fairly low wall-plug efficiency of DUV LEDs. By improving the light extraction efficiency, more important applications of deep UV LEDs will be realized.

Low wall plug efficiency (~1-2%) and device reliability are the key issues preventing the large scale production of these LEDs. It is now well established that the EQE of AlGaN DUV light emitting devices decreases with decreasing emission wavelength i.e. with an increase of AlN mole fraction in active region. There are a few factors, that limit the EQE, including the large number of dislocations ($\sim 10^{10}$ cm^{-2}) in the active region, inefficient p-type doping of AlN and Al-rich AlGaN alloys, low light extraction efficiency due to dominant in-plane propagation in Al-rich c-plane devices, and an excessive rise in junction temperature with time. Improvement in the device performance by addressing each of these areas promises a bright future for AlGaN based deep UV LED technology. However, each of these improvements requires a great deal of

effort. Research activities with the aim to address these issues are currently underway in many research groups around the world. We have investigated the optical properties of available AlN bulk susbstrates and AlN homoepilayers of different crystallographic orientations. The feasibility of using Be as a p-type dopant to address p-type issue in AlN has also been assessed.

A large fraction of the AlGaN alloys based deep UV devices fabricated and tested so far have been grown heteroepitaxially on sapphire or SiC. Due to the lattice and thermal expansion mismatch with the substrate, strain is accumulated in active AlGaN epilayers generating a high density of TDs, which act as nonradiative recombination centers and also degrade the p-type layers. TDs are the major factors affecting the output power and operation lifetime of these devices. DUV LEDs based on conventional c-plane AlGaN heterostructures also exhibit blueshift of the emission wavelength at higher injection currents.

1.3 AlN band Structure

In AlN or GaN, the top of the valence band mainly arises from N 2*p* states, where as the bottom of the conduction band originates from N and cation (Al or Ga) *s* states. Using the irreducible representation of the group theory, the top of the valence band is labelled as Γ_{15}. Due to the hexagonal symmetry of the wurtzite structure, the interaction energy with electrons of neighboring atoms in tetrahedral structure is different in the directions parallel and perpendicular to the hexagonal plane. The electrons in the atoms lying closer experience stronger repulsion and possess higher energy compared to those lying farther apart. This difference in interaction energy leads to the splitting of the top of the *p*-like valence band into two groups with an energy difference of Δ_{CF}, which is called the crystal-field splitting parameter. These states are labelled as Γ_6 and Γ_1. The wave functions of the Γ_6 state transform like x and y, where as those of the Γ_1 state

transform like z. The order of the Γ_6 and Γ_1 levels and the magnitude of the splitting energy depend on the nature of the cation involved, the ratio of the two lattice constants (c/a), and the cell internal parameter (u). The internal parameter u denotes the relative displacement of the N sublattice with respect to the cation sublattice along the c-axis expressed in terms of c lattice constant. Due to the spin-orbit coupling, the twofold degenerate Γ_6 state is further split into the Γ_9^v and Γ_7^v levels and the non-degenerate Γ_1 state is labelled as Γ_7^v. The magnitude of the spin-orbit splitting (Δ_{SO}) is much smaller compared to Δ_{CF}.

The measured values of the valence band splitting energies [$\Delta_{CF} = \varepsilon(\Gamma_6^v)- \varepsilon(\Gamma_1^v)$ and $\Delta_{SO}= \varepsilon(\Gamma_9^v)- \varepsilon(\Gamma_{7-}^v)$] scatter in a wide range for different samples synthesized in different ways on a variety of substrates. Uncertainty arises primarily from the influence of strain on the bandgap. It has been established that the lattice mismatch between the film and the substrate is correlated with the bandgap of the film. However, it is now accepted that the value of Δ_{CF} is much larger and negative in AlN compared to that in GaN and InN, which results in different ordering of the valence bands in AlN as illustrated schematically in the Fig. 1.3.

Optical transitions between the conduction band (Γ_7^c) and the three valence band states in AlN are labeled as A ($\Gamma_7^c \leftrightarrow \Gamma_{7+}^v$), B ($\Gamma_7^c \leftrightarrow \Gamma_9^v$), and C ($\Gamma_7^c \leftrightarrow \Gamma_{7-}^v$) in the order of increasing energy. In the case of strain-free AlN, band-to-band transition A is allowed only for $\vec{E} \parallel \vec{c}$ configuration while B and C transitions are allowed only for $\vec{E} \perp \vec{c}$ configuration. The optical and transport properties of AlN are mainly determined by the holes in the uppermost valence band due to a huge energy difference (~0.2 eV) between the topmost level and the other two valence bands. However, the Γ_9^v state becomes the uppermost valence band in GaN due to positive values of both Δ_{CF} and Δ_{SO} so that the fundamental optical transitions would be A ($\Gamma_7^c \leftrightarrow \Gamma_9^v$), B ($\Gamma_7^c \leftrightarrow \Gamma_{7+}^v$), and C ($\Gamma_7^c \leftrightarrow \Gamma_{7-}^v$) in order of increasing energy. These transitions are

polarized in $\vec{E} \perp \vec{c}$, $\vec{E} \perp \vec{c}$, and $\vec{E} \parallel \vec{c}$ configurations, respectively. These inherent properties of emitted light polarization have huge consequences on emission efficiency, leading to a weak (strong) surface emission of light emitting devices employing the conventional c-plane AlGaN active layers in Al (Ga) rich side.

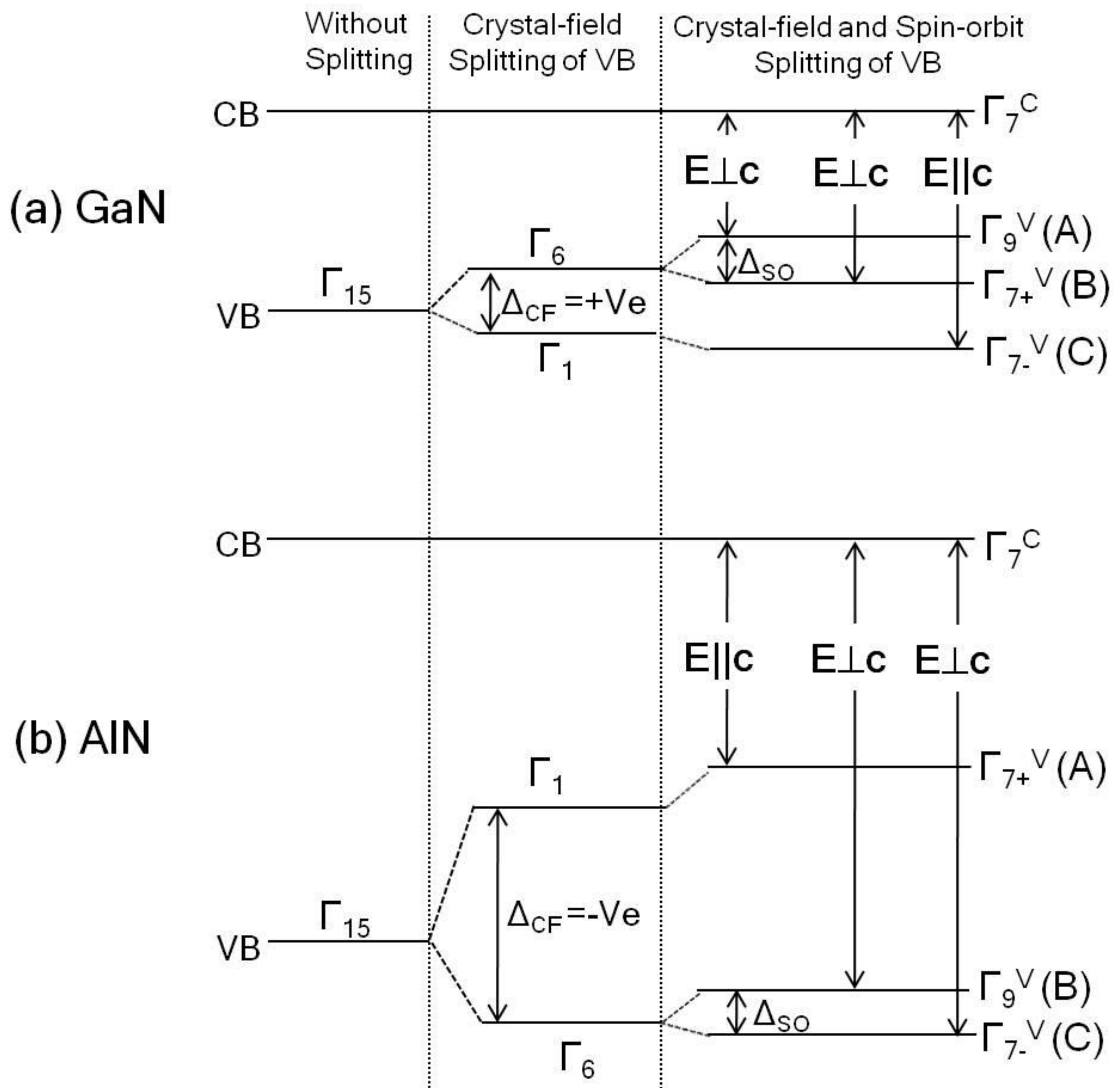

Fig. 1.3 Schematic band structure diagram of AlN showing the crystal-field and the valence band splittings on top of the valence band at Γ-point. Band structure for GaN is also included for comparison.

Table 1.2 Material properties of AlN and GaN from various sources.

Property	AlN	GaN
Lattice parameters (A^0)	a=3.1111 (c=4.9788)	a=3.190 (c=5.189)
Thermal expansion coeff. (x $10^{-6,}$ K^{-1})	α_a=4.2 (α_c=5.3)	α_a=3.17 (α_c=5.59)
Thermal conductivity (κ, W/cm K)	3.19	1.3
Atomic density (atoms/cm^3)	9.58 x 10^{22}	8.9 x 10^{22}
Density (gm/cm^3)	3.255	6.07
Melting Point (K)	3025	2791
Bulk modulus (dyne/cm^2)	21x10^{11}	20.4x10^{11}
Elastic const. (C_{11},C_{12},C_{13},C_{33})(GPa)	296, 130, 158, 267	377, 160, 114, 209
Piezoelectric coefficient (e_{33}, C/m^2)	1.46	0.73
Effective masses (m_0)	$m_e^{\parallel}$=0.33 ($m_e^{\perp}$=0.25) $m_{h,A}^{\parallel}$=3.53 ($m_{h,A}^{\perp}$=11.14) $m_{h,B}^{\parallel}$ =3.53 ($m_{h,B}^{\perp}$= 0.33) $m_{h,C}^{\parallel}$=0.26 ($m_{h,C}^{\perp}$= 4.05)	$m_e^{\parallel}$=0.20 ($m_e^{\perp}$=0.18) $m_{h,A}^{\parallel}$=1.1($m_{h,A}^{\perp}$=1.65) $m_{h,B}^{\parallel}$=1.1($m_{h,B}^{\perp}$= 0.15) $m_{h,C}^{\parallel}$=0.15($m_{h,C}^{\perp}$= 1.1)
Refractive Index	2.15 @ 3.0 eV	2.67 @ 3.38 eV
Dielectric constant	ε_0=9.14 $\varepsilon_\infty^{\parallel}$=4.93 ($\varepsilon_\infty^{\perp}$=4.71)	$\varepsilon_0^{\parallel}$=10.4 ($\varepsilon_0^{\perp}$=9.5) $\varepsilon_\infty^{\parallel}$=5.8 ($\varepsilon_\infty^{\perp}$=5.35)
$E_{g,}$ eV (free exciton B.E., meV)/10 K	6.1 (47-80)	3.5 (20)
E_A, E_B, E_C (eV) [on Al_2O_3 @ 10 K]	6.050, 6.249, 6.262	3.475, 3.482, 3.493
VB splitting parameters (meV)	Δ_{CF}=-206 (Δ_{SO}=20)	Δ_{CF}=40 (Δ_{SO}=8)
Varshni coefficients (T dep. of E_g)	α=2.59 meV/K β=2030 K	α=0.84 meV/K β=789 K
Phonon wavenumbers, cm^{-1} [(E_2^1, A_1(TO), E_2^2, E_1(TO), A_1(LO), E_1(LO)]	248.6, 611, 657.4, 670.8, 890, 912	145, 533, 567, 560, 735, 742
Effective CB density of states Effective VB density of states	6.3 x 10^{18} cm^{-3} 4.8 x 10^{20} cm^{-3}	2.3 x 10^{18} cm^{-3} 4.6 x 10^{19} cm^{-3}

1.4 Substrate issue in deep UV photonics

Crystals grown on foreign substrate of different lattice constant contain misfit dislocations, which extend up to the subsequent layers and form TDs. If not properly managed, different thermal expansion coefficients between the substrate and film may lead to cracks while cooling down to room temperature from high growth temperature [33]. III-nitride deep UV LED structures are grown on foreign substrates, such as sapphire, SiC, or Si. Sapphire is preferred for its optical transparency to DUV wavelengths. However, large lattice (13-16%) and thermal expansion coefficient mismatches lead to a high TD density on the order of 10^{10} cm^{-2}. Due to the low thermal conductivity of sapphire (35 vs 319 W/m K in AlN), it is difficult to drain accumulated heat out of the device, leading to an increase in junction temperature and output power degradation.

High power light emitting devices require very high pump current density. It heats up the device and causes the output power to saturate. This kind of premature power saturation is more pronounced in devices with a higher number of dislocations [34]. Dislocation density has to be lowered in order to improve both the efficiency and lifetime of the light sources. Almost four orders of magnitude improvement in output power of a set of AlGaN/GaN based UV LEDs operating at 360 nm has been observed by reducing TD density [35], as shown in Fig. 1.4. Electrical properties are also affected severely by dislocation. It is illustrated by the linearly decreasing electron mobility in Si doped n-$Al_{0.34}Ga_{0.66}N$ from 80 to 10 cm^2/V s as TDD increases [36]. Electron concentration has been decreased by almost 50%, which is shown in Fig. 1.5.

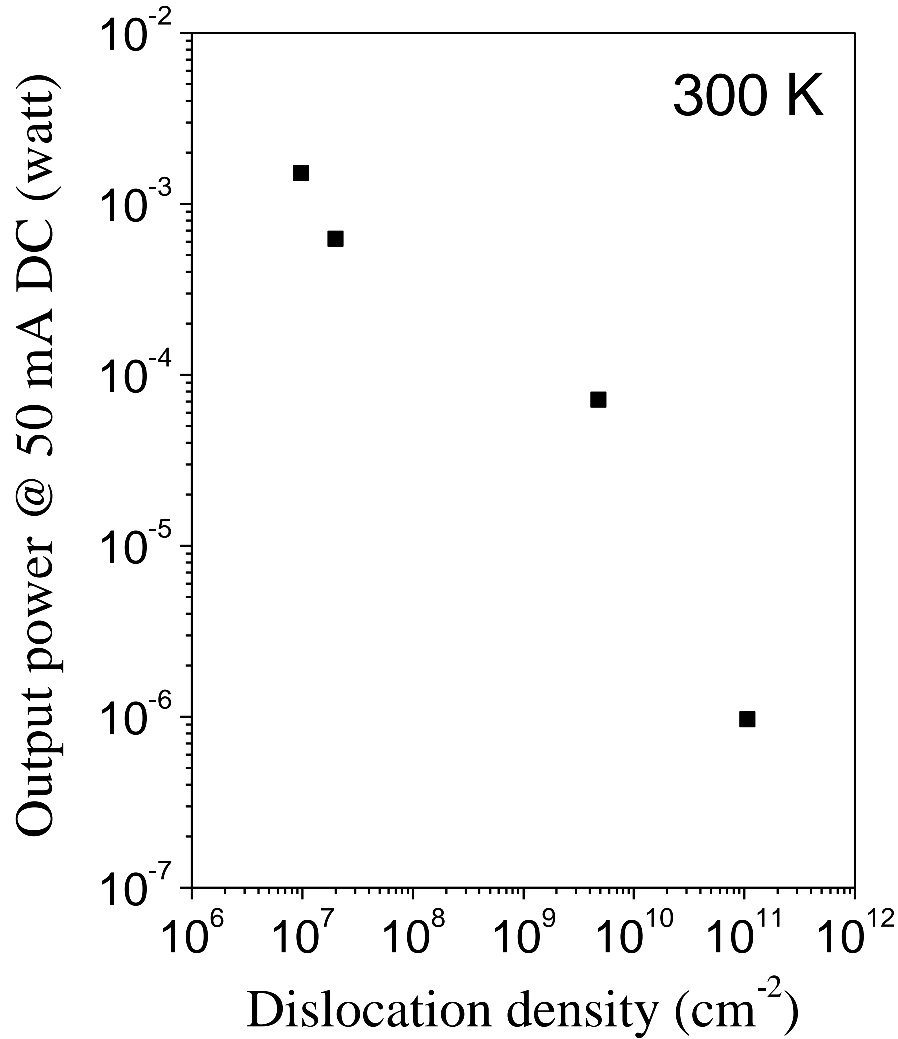

Fig. 1.4 Output power of UV LEDs at 50 mA drive current with GaN active layer on various AlGaN with different dislocation densities (Ref. 35. Copyright Wiley-VCH Verlag GmbH & Co. KGaA. With permission).

In photodetectors, dislocations provide an alternative carrier recombination channel, which increases the leakage current leading to the possible failure of the device when operated under applied high voltage. The amount of stress and, hence, the number of dislocations also depend on doping.

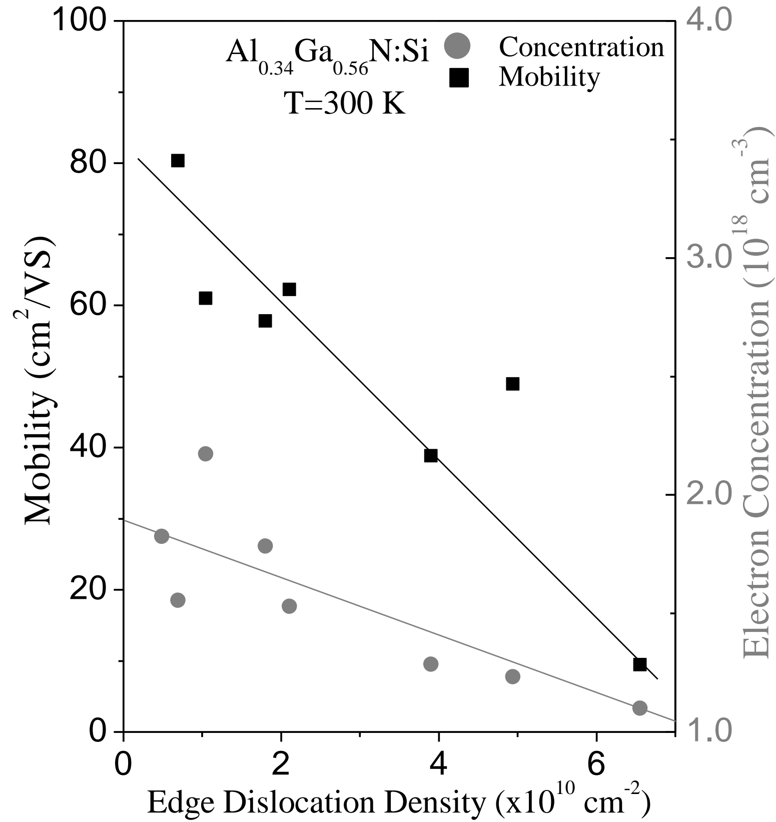

Fig. 1.5 Carrier concentration and mobility of a Si-doped n-type $Al_{0.34}Ga_{0.66}N$ as a function of dislocation density measured at room temperature. Solid lines are guides to eye. (Ref. 36, Copyright American Institute of Physics. With Permission)

An appropriate substrate has been sought for the growth of high quality nitride epilayers for electronic and optoelectronic applications. An ideal substrate is expected to have its in-plane lattice constant and thermal expansion coefficient as close to those values for the film as possible. For deep UV LEDs, in particular, high thermal conductivity and transparency in the deep UV wavelengths are also desired. Several methods, such as superlattice (SL) buffer, lateral overgrowth on patterned substrates etc., have been introduced to reduce dislocation density in materials grown on foreign substrates. However, homoepitaxial growth has the highest potential

to lower the dislocation densities in subsequent layers. AlN bulk substrates with reasonable size (2”) and threading dislocation density (TDD) <10^4 cm^{-2} has already been achieved [37]. A few UV light emitting devices have already been fabricated on bulk AlN substrates [12,38-40]. AlN bulk substrates appearing with dark or yellow color are highly undesired as they absorb deep UV emission from active layers. The mechanism behind such undesired coloration in bulk AlN is investigated in this thesis.

1.5 Formation and optical properties of native point defects in AlN and Al-rich AlGaN alloys

Cation vacancies and their complexes with unintentionally incorporated donor impurities, such as Al vacancy (V_{Al}) and Al vacancy-O complex (V_{Al}-O_N), have low formation energies in undoped and Si doped AlN or Al-rich AlGaN alloys. But in p-type doped materials, which have their Fermi level towards the valence band side from the mid-gap region, it is very difficult for the cation vacancies and their complexes to form, whereas nitrogen vacancies (V_N) are easily formed due to their low formation energy as shown in Fig 1.6 [41].

The formation of native point defect recombination centers in AlGaN alloys is undesired as they offer the electronic levels deep inside the bandgap. They provide an alternate carrier recombination channel, which reduces the radiative recombination rate in the near bandedge region and hence decreases the radiative efficiency of the device. Reduced quantum efficiency due to native point defects has been demonstrated in a recent report by measuring the excitonic radiative lifetime (τ_R) as function of aluminum vacancies (V_{Al}) via S parameter. Intrinsically very short τ_R for AlN (10 ps at 7 K) was increased to 530 ps with an increase in V_{Al} but it is not

sensitive to the TDD [42]. High concentration of these deep centers acting as single to the triple electron traps are partly responsible for low n-type conductivity observed in Si-doped AlN and

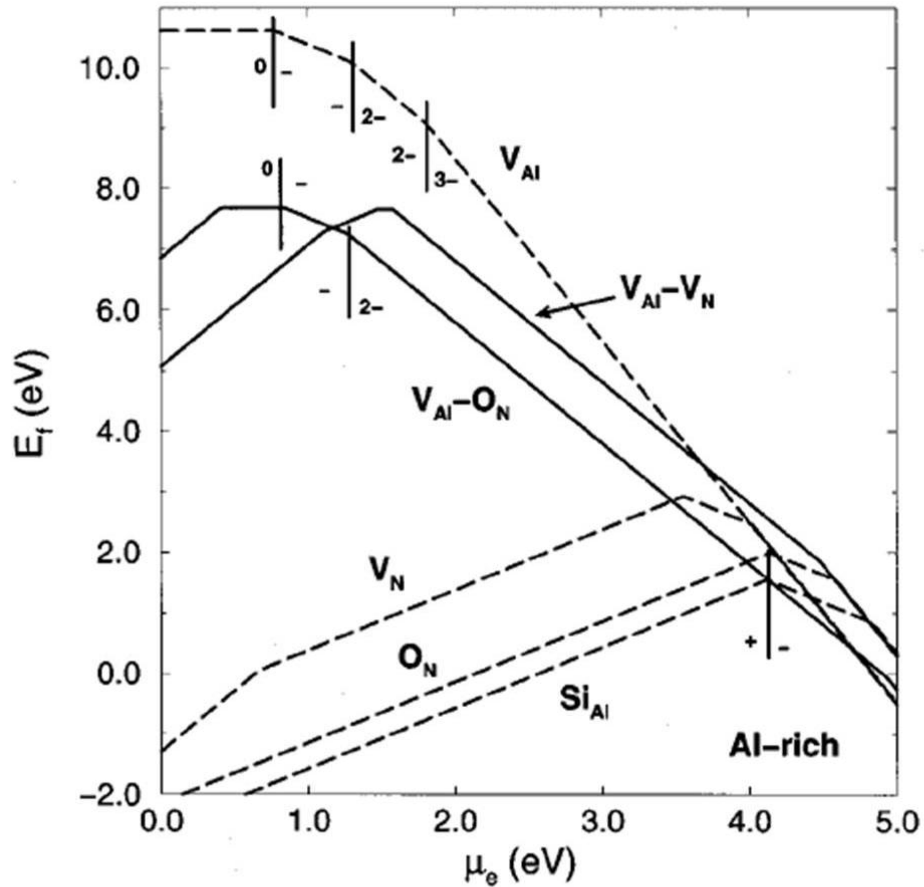

Fig. 1.6 Formation energies of various native point defects and their complexes in AlN plotted as functions of the fermi level position (With permission from Ref. 42. Copyright by the **American Physical Society**).

Al-rich AlGaN alloys [43]. Therefore, it is very important to identify and reduce the number of defects in the material in order to achieve good performance and extended lifetime of the device. Deep UV time-resolved PL spectroscopy has been established as the most effective way of monitoring these defects experimentally. It gives a clear qualitative assessment of the

concentration of these defects using the intensity of near bandedge PL emission relative to various defect-related emission lines in the lower energy region of the spectrum. Time-resolved measurements can be used to further identify the possible physical origin of those transition lines. Therefore, deep UV time-resolved PL spectroscopy has become an important tool in order to optimize the synthesis of high quality deep UV materials with low defect densities.

Significant progress has been made in past several years in terms of experimental studies of optical transitions related to the deep centers in AlGaN alloys. Our group has reported three

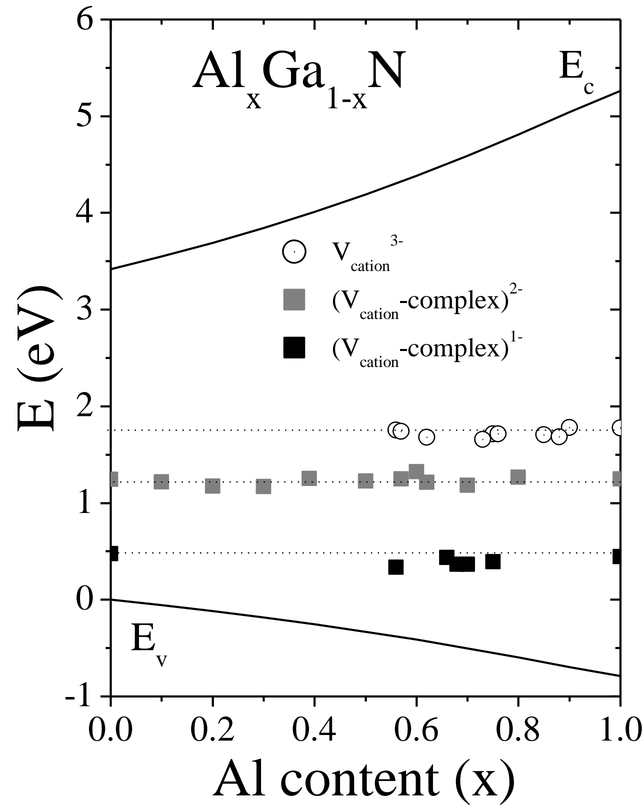

Fig. 1.7 Deep acceptor levels of (V_{III}-complex)$^{1-}$ (black squares), (V_{III}-complex)$^{2-}$ (gray quares), and (V_{III} –complex)$^{3-}$ (open circles) plotted together with E_c, E_v, as functions of Al content (x) (With Permission from Ref. 45. Copyright American Institute of Physics).

groups of acceptor-like native point defects in AlGaN alloys probed by deep UV time-resolved PL and Hall-effect measurements [44,45]. It includes isolated cation vacancies ($V_{III}^{3-/2-}$) and vacancy-impurity complexes [$(V_{III}\text{-}O_N)^{2-/1-}$ and $(V_{III}\text{-}2O_N)^{1-/0}$] in undoped and Si doped AlGaN alloys. Donor-to-acceptor pair (DAP) transitions involving shallow donors (O or Si) and these acceptors were observed in $Al_xGa_{1-x}N$ alloys with all x for $(V_{III}\text{-}O_N)^{2-/1-}$ and $(V_{III}\text{-}2O_N)^{1-/0}$ and only with x>0.58 for $V_{III}^{3-/2-}$. Deep acceptor levels associated with these deep centers are plotted in Fig. 1.7 together with conduction band (CB) and valence band (VB) edges (E_C and E_V, respectively) as functions of Al-content, taking top of the VB of GaN as reference zero level. Room temperature band gaps of GaN and AlN were taken as 3.42 eV and 6.05 eV, respectively. CB and VB offset parameters have been considered to be 0.70 and 0.30, respectively. This thesis discusses a group of five possible optical transitions involving these deep centers and the valence band in AlGaN alloys [46,47] taking the Al-N bond anisotropy into account.

1.6 p-type doping issue in AlN and Al-rich AlGaN alloys

Achieving conductive p- and n-type layers of AlN and Al-rich AlGaN with reasonable free holes and free electron concentrations (~10^{17} cm^{-3}) is required to achieve desired III-nitride based deep UV photonic devices. However, controlled doping is difficult whether it is p- or n-type, as the energy level of the dopant impurity deepens and the formation of defects acting as the compensating centers increases with increasing Al content. The n-type AlN layers with free electron concentration on the order of 10^{17} cm^{-3} and room temperature electrical conductivity of ~1 (Ω cm)$^{-1}$ can be obtained with Si doping [22]. For p-type, Mg is a universal dopant in all III-nitride materials, which gives reasonable free hole concentration in AlGaN alloys with lower Al

content. Achieving p-type (at room temerature) $Al_xGa_{1-x}N$ alloys for x>0.7 with Mg doping is found too difficult [48,49]. Mg doped AlN samples are highly resistive at room temperature and the acceptor ionization energy is quite large (~0.5-0.6 eV), which gives a very low free hole concentration of ~10^{11} cm^{-3} [50,51]. Resistive p-type layers employed in the device structure increase the total series resistance, which causes the operating voltage of the device to increase

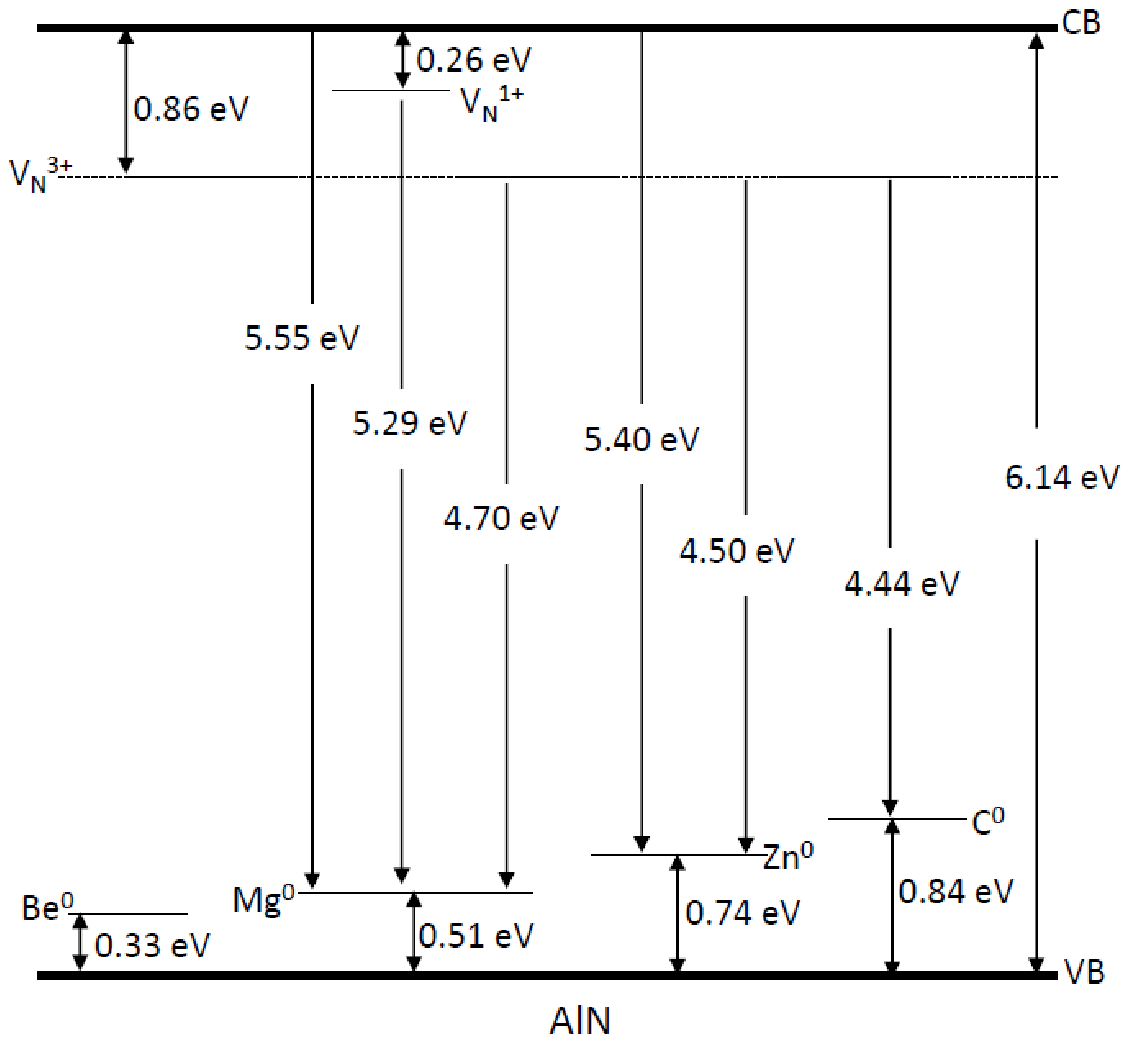

Fig. 1.8 Schematic diagram showing the donor levels of nitrogen vacancies (V_N^{3+} and V_N^{1+}) and acceptor levels of Be^0, Mg^0, Zn^0, and C^0in AlN.

as well. In addition to the inefficient hole injection, deep UV emitters use Mg doped AlGaN layers with low x as p-type cladding and contact layers, which absorb deep UV light emitted from the active region, thereby further reducing the external efficiency.

Zn, C, and Be have been suggested by calculations as possible alternative p-type dopants for III-nitrides. We studied the feasibility of using these elements in AlN by deep UV time-resolved PL spectroscopy and the results are summarized in Fig. 1.8. It includes the acceptor energy levels of C, Zn, Mg, and Be, and the donor levels of V_N^{3+} and V_N^{1+} in AlN. The corresponding transitions, which are observed, are shown with downward arrows. All as-grown and post growth annealed layers were highly resistive at room temperature (RT), however, these results clearly indicate that Be is shallower in AlN than Mg while Zn and C are deeper than Mg.

In most cases, a p-type dopant is an element lying just to the left of the cation host in the periodic table, which is believed to replace the cation and contribute an acceptor level above the valence band maximum. C acts as an acceptor in AlN only when it sits in the N site. Based on first-principle calculation, Van de Walle et al have recently proposed the idea of using F as a p-type dopant in wide bandgap semiconductors [52]. They suggest that interstitial F acts as a shallow accepter, which could be a major breakthrough if confirmed in experiments. P-type doping of AlN with Be doping has been investigated in this thesis.

1.7 III-nitrides on non-polar and semi-polar substrates

Optoelectronic devices employing quantum well structures exhibit enhanced performance in several ways, such as increased quantum efficiency, reduced threshold current density, reduced sensitivity to the temperature, etc. Conventionally, III-nitride epilayers and QW structures are grown on the c-plane of the substrate. C-plane orientations impose two major

limitations in the device. First, due to the polarization discontinuities at the hetero-interfaces, conventional c-plane nitrides QWs possess strong internal electric fields. This results in band bending so that electron and hole wave functions in the quantum well region are spatially separated, as shown in Fig. 1.9, leading to a reduced radiative recombination rate and hence reduced quantum efficiency [53]. Secondly, especially when the active layer contains Al-rich AlGaN alloys, emitted light is polarized along the c-axis direction and propagate parallel to the surface so that light extraction in surface emitting devices becomes increasingly difficult with decreasing emission wavelength. This results in a sharp deterioration of the overall efficiency of AlGaN based UV and deep UV emitters towards the shorter emission wavelengths.

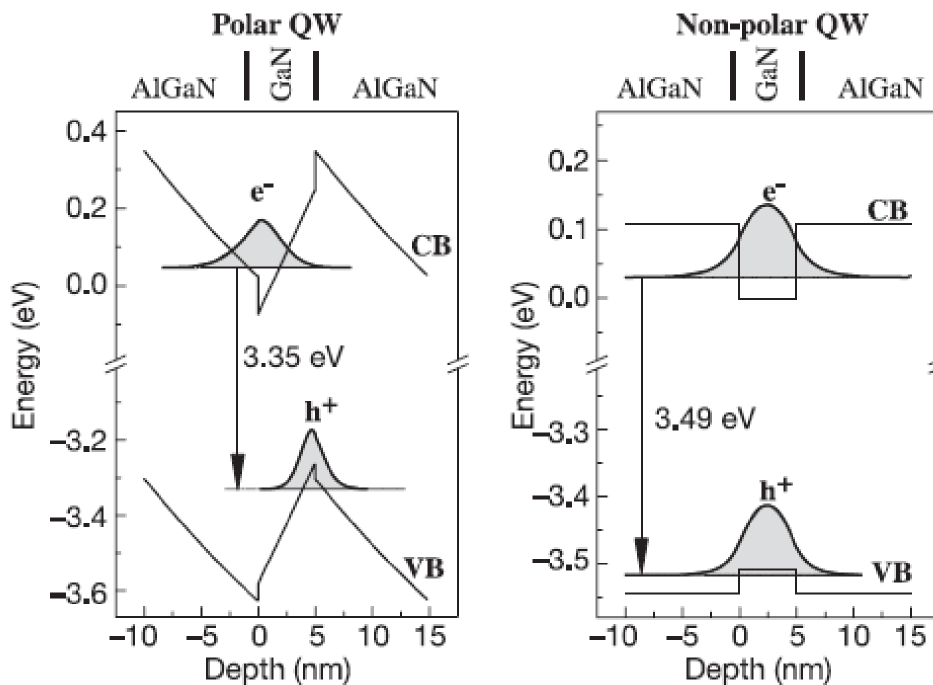

Fig. 1.9 Schematic diagram showing the band bending in polar c-plane AlGaN/GaN QW (left) and no band bending in similar QW in non-polar orientation (right) (Ref. 53. Copyright Wiley-VCH Verlag GmbH & Co. KgaA. With Permission).

Growing III-nitride QW based structures on semi-polar or non-polar (a- or m-plane) substrates has attracted a significant amount of research effort in the past several years. Despite the difficulties associated with non-polar and semi-polar growth, an output power of 23.7 mW for a m-plane InGaN/GaN MQW LED emitting at 407 nm has been demonstrated with an EQE of 38.9% at a 20 mA drive current, which is comparable to the existing state-of-the-art c-plane LEDs [54]. AlGaN based UV emitters have also been demonstrated in non-polar orientations; however, the emission intensity is much lower compared to matured c-plane grown devices [55] at this point.

1.8 Overview of the thesis

This thesis mainly discusses the optical characterization and optical studies of wide bandgap III-nitride semiconductors and nanostructures by using the deep UV time-resolved photoluminescence spectroscopy. It provides information on intrinsic as well as extrinsic effects induced by impurities and defects in the materials. The thesis is divided into 4 chapters. In chapter 1, a brief introduction and current issues on III-nitride semiconductors have been discussed. Experimental part, mainly the equipments and the methods are discussed in chapter 2. Results obtained from the experiments are discussed in chapter 3 and the thesis is wrapped up with the general conclusion in chapter 4.

Chapter 2 - Experimental facilities

In this chapter, the various experimental tools employed in this work are discussed briefly. Metal organic chemical vapor deposition (MOCVD) and deep ultra-violet (DUV) time-resolved photoluminescence spectroscopy systems have been discussed along with other characterization tools such as X-ray diffraction (XRD), Hall-effect measurement, atomic force microscopy (AFM), and secondary ion mass spectroscopy.

2.1 Deep UV time-resolved photoluminescence system for optical studies

The deep UV PL system utilized in this study consists of a ultra-fast light source (frequency quadrupled Ti-sapphire laser) and pico-second time-resolved detection systems as illustrated schematically in Fig. 2.1. It is integrated with a nearfield scanning optical microscope (NSOM) system through optical fibers, which provides a spatial resolution down to 50 nm. In PL, a sample is excited with a pulsed or modulated light source and the emitted light is analyzed to obtain the sample parameters.

2.1.1 Ultrafast laser system

An excitation laser with photon energy (hν) exceeding the band gap energy (E_g) of the material being studied is required to probe the material characteristics by PL. Since the continuous-wave (CW) laser can only provide time-averaged information, time-resolved PL systems are highly desired for fully exploring the dynamics of excited carriers along with time-averaged information. It requires a pulsed excitation laser source. The pulse characteristics of the

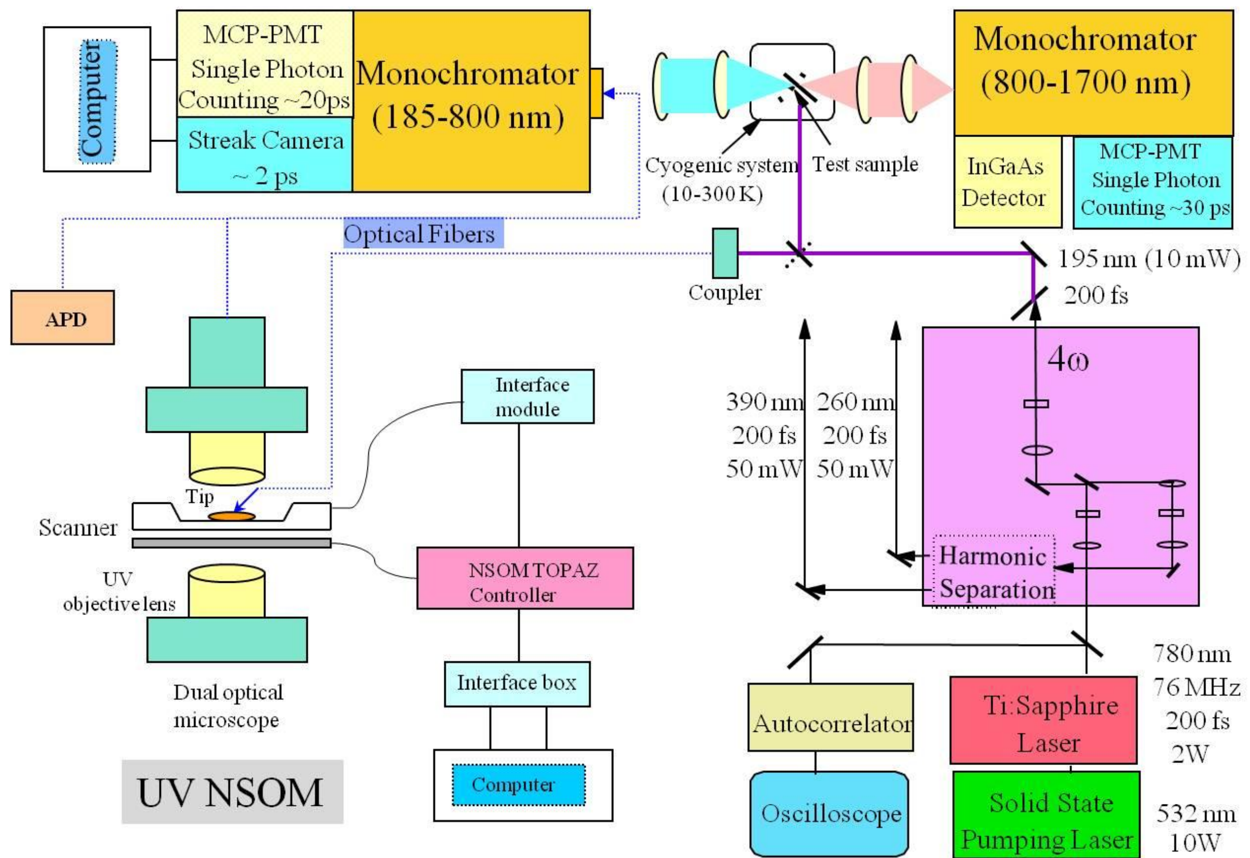

Fig. 2.1 Experimental setup of the time-resolved PL spectroscopy system with detection capability from deep UV to IR (185 nm-3 μm) intergrated with the NSOM system (Ref. 65).

excitation laser are carefully designed so as to achieve sufficiently high pulse power and narrow pulse width, as well as a suitable repetition rate. Using a pulsed laser, one can deliver very high instantaneous excitation power, which is not possible with a CW laser. The lasing output of the CW laser exhibits many axial modes with different phases and amplitudes, causing an interference effect varying with time. However, in mode-locked operation, there is no time dependence as the infinite train of pulses has the same wave shape as the distribution of mode amplitudes. The laser system used in this study was a solid-state laser pumped Ti-sapphire laser.

2.1.1.1 Pump laser

A Verdi 10 (V-10) laser from Coherent, Inc. was used as the pumping power source to the Ti-sapphire laser. The pump laser consists of two major components: the power supply and the laser head. The power supply unit provides DC power to two laser diode assemblies, each contains a FAP-I called fiber array package – integrated. Each FAP-I efficiently converts low-voltage high-current electrical power into tunable laser, which is centered on the strong absorption band of neodymium ions near 808 nm. It is the gain medium of pump laser. The fiber optic cables, enclosed in umbilical, transmit the light from the diode arrays in the power supply unit to pump the vanadate crystal in the laser head. The characteristic lasing wavelength of the neodymium doped yttrium orthovanadate ($Nd:YVO_4$) is nominally 1064 nm. It is frequency doubled using the nonlinear crystal lithium triborate (LBO), which provides the final pump beam at 532 nm with a high pumping power of 10 W. For the ideal conversion efficiency, LBO is held at approximately 148 ^{0}C. A photodiode in the laser head monitors the laser output relative to the power level requested from the front panel in the power supply and adjusts the pump electrical power to the vanadate in order to deliver a stable pump beam to the Ti-sapphire laser.

2.1.1.2 Ti-sapphire laser

A Coherent Mira-900F mode-locked ultrafast laser with a Ti doped sapphire crystal ($Ti:Al_2O_3$) as gain medium was used as an excitation light source in this study. Typically, the emission wavelength of Mira-900 is tunable from 700 to 1100 nm with a pulse width less than 150 femto-seconds (fs) and repetition rate of 76 MHz. While the pulse trains travel back and forth several times between output coupler and high reflector through the gain medium perfectly perpendicular to them, a small fraction of the pulse transmits from the output coupler each time

to form the output laser beam. Ultimately, a laser beam with photon energy exceeding 6.1 eV is required in this study to excite AlN across its bandgap. Since the peak power of Ti-sapphire laser is around 800 nm, the wavelength of Ti-sapphire laser is tuned to ~780 nm with an average output power ~2.1 W CW (1.9 W pulsed). Laser pulses are generated from passive mode-locking by self focusing generated from the optical Kerr effect in Ti:sapphire crystal in combination with a suitably narrow slit width. The atoms of Ti:sapphire crystal are distorted from the electric fields associated with extremely high light intensity. It alters the refractive index of the crystal generating the gradient index lens (called the Kerr lens) resulting from changes in the spatial profile of the beam so that the beam is further focused. Only mode-locked pulses with strong intensity will be able to form a Kerr lens and be further narrowed, whereas weak intensity laser operating CW can't form such lens and travels with larger diameter. The width of the slit is adjusted to block the CW operation at its edges but the narrower mode-locked beam will pass uninterrupted.

2.1.2 Super quadrupler

Light with the photon energy enough to excite the carriers across the ultra-high band gap of AlN and Al-rich AlGaN alloys (up to 6.1 eV) is achieved by generating the fourth harmonic of Ti:sapphire laser (peak emission set ~1.6 eV) using a semi-home-built equipment called the super quadrupler. The super quadrupler is even more important for probing the quality of deep UV materials, which are insulating in nature, making electrical characterization difficult at least during the development of a suitable doping mechanism. Furthermore, ultrashort light pulses in the 195 nm spectral region provide a unique opportunity for the spectroscopic study of ultrafast phenomena (carrier relaxation dynamics) in such a large energy gap materials. The final

excitation beam from the quadrupler has a power of about 1 mW at photon energy of ~6.35 eV, just above the AlN band gap. The super quadrupler employed in this study quadruples the fundamental frequency or photon energy of the laser in three stages using nonlinear crystals. The second harmonic (SH) generated by frequency doubling follows two-steps of sum frequency generation in order to achieve the third (TH) and the fourth harmonics (FH). It provides better conversion efficiency of FH relative to the direct doubling of SH pulses and also provides additional line for excitation.

The development of ultrashort laser pulses has made it possible to focus extraordinarily intense electromagnetic radiation onto a tiny spot, which induces a nonlinear response on suitable nonlinear material leading to the generation of higher harmonics. The focused beam has an average power of 2 W at 76 MHz and is delivered by a femtosecond version of the Mira-900 Ti:sapphire laser. Setting the Mira-900 at 780 nm, SH (390 nm) pulses are generated in lithium triborate (LiB_3O_5 or LBO) crystals. The fundamental and SH pulses from different optical paths were focused on a beta-barium borate (β-BaB_2O_4 or BBO) crystal to generate TH pulses (263 nm) using type I phase matching, maximizing the effective nonlinearity. FH (195 nm) were generated by mixing the fundamental wave and TH using type I phase matching in another BBO crystal giving about 1 mW of high repetition rate femtosecond pulses for the excitation of ultrawide band gap meterials. In order to achieve high conversion efficiency between TH and FH, respective delay lines and the crystals have to be optimally positioned to satisfy phase matching conditions.

The design of the quadrupler allows us to use the fundamental laser beam (780 nm) as well as all the higher harmonics (390, 263, and 195 nm) as needed depending on the band gap of

the material under investigation. The intensity of the selected laser pulse is controlled by using neutral density filters.

2.1.3 Detection system

Depending on the spectral region of interest, we have a few choices for detection systems. The components of the detection systems include UV/visible and IR monochromators, PMTs, InGaAs detector, time-correlated single photon counting system, and streak camera.

2.1.3.1 Monochromator

In deep UV to visible wavelengths, the collected PL signal is dispersed by an ARC AM-511 model monochromator from Acton Research Corporation. The collimating optics of the monochromator has a focal length of ~1.33 m and is Czerny-Turner type designed for use from 1849 to 8200 A^0, which provides a wavelength resolution of 0.01 nm with a 1200 g/mm grating in reflective mode and a 10 μm slit width. "Snap-in" type grating assembly allows easy replacement of the desired grating without requiring the realignment. The wavelength scanning drive can be controlled manually or using a stepping motor by rotating the precision drive screw. Of the two exit ports of this monochromator, one is connected to a PMT that provides amplified PL signal for the single photon counting system and the other is connected to a streak camera.

The other monochromator used in this study is a fully computer controlled SpectraPro 300i from Acton Research Corporation. It is used to disperse the collected PL signal in the IR region from 800 nm to 3.0 μm and has a focal length of 0.3 m. Two gratings are installed in its triple grating turret and the desired one can be selected using the computer control. Light enters from a single entry port but may exit from either of the two exit ports. The PMT receives a PL

signal from one of the exit ports, which allows us to perform time-resolved measurement up to 1.2 μm. An appropriate InGaAs detector is connected to the other exit port, which is sensitive from 0.8 to 3.0 μm. All the entry and exit ports are equipped with micrometer controlled slit width settings from 10 μm to 3 mm.

2.1.3.2 Time-correlated single photon counting

One of the time-resolved measurement systems used in this study is the time correlated single photon counting, which includes two detectors (PMT and photodiode), preamplifiers, delay, timing discriminators, time to amplitude converter (TAC), analog to digital converter (ADC), and multi channel analyzer (MCA), which is shown in the block diagram in Fig. 2.2.

A small fraction of the laser beam is delivered to the photodiode (Antel Optronics Inc., AR-S2, RS-26204) in order to generate a trigger signal, which is amplified by a preamplifier (Ortec VT120) and fed into the Constant Fraction Discriminator (CFD). The CFD converts this signal into a fast logic pulse, which defines the time when the excitation pulse occurs by initiating a charging ramp in the TAC. The major part of the laser is used to excite the sample. The PL signal ejects electrons from the photocathode at PMT (R3809U from Hamamatsu), which are accelerated with high voltage (~3 kV). While colliding on the walls of microchannel tubes during acceleration, electrons are multiplied, giving rise to a negative polarity pulse with an amplitude in the order of 20 mV and a width of ~400 ps. The pulse is further amplified by another preamplifier (Ortec 9306) and the signal is fed into the pico-timing discriminator (PTD), which defines the arrival time of these pulses with pico-second precision. In fact, PTD generates two identical logic pulses. One of the pulses is used to define the exact time when the PL signal arrived by stopping the charging of the capacitor in the TAC (time-resolved PL measurement).

The other pulse is sent to a ratemeter (Ortec 661) and then to a digital multimeter to display the numerical value corresponding to the PL intensity (CW PL measurement). A discriminator also distinguishes the photon pulses from the noise level in reference to its pre-defined threshold level as illustrated in Fig. 2.3 [56].

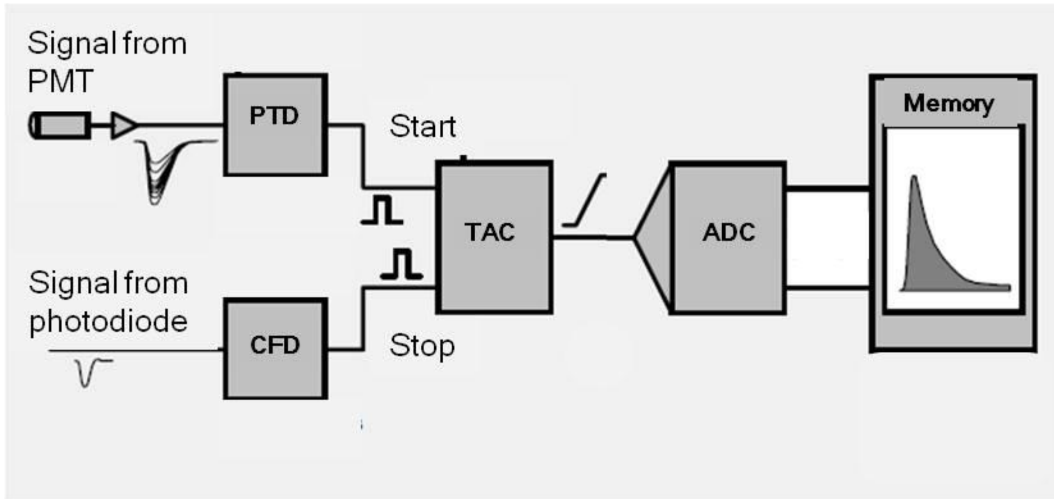

Fig. 2.2 Schematic representation of single photon counting system (With kind permission from Springer Science+Business media, Ref. 56. Copyright Springer-Verlag Berlin Heidelberg 2005).

The charge stored in the capacitor and hence the voltage amplitude in the TAC is proportional to the time interval between the signal from photodiode (excitation) and the signal from PMT (PL signal). Every single output pulse from TAC is given a numerical value in analog to digital convertor (ADC) corresponding to the voltage amplitude. The count is registered as a discrete event in a proper channel number in a multichannel analyzer (MCA). The process is repeated in subsequent laser pulse cycles and a histogram of counts versus the channel number (time) is generated. The histogram is displayed on a computer screen as temporal response of PL.

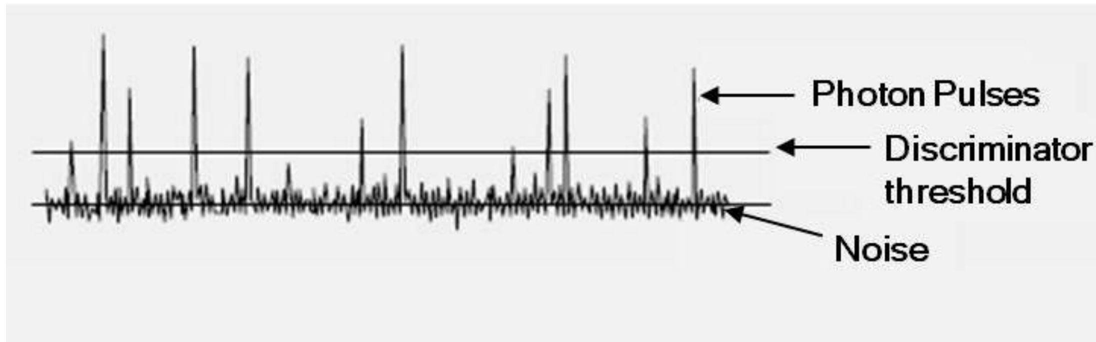

Fig. 2.3 Schematic representation showing the single photon pulses separated from noise background with adjustable discriminator threshold (With permission from Ref. 56).

In this work, a trigger is generated from low power of the fundamental laser pulse (780 nm) and the luminescence signal is excited with suitable higher harmonic pulses. The gain and rise time of the preamplifiers are matched to the PMT's signal. Pulse width after preamplifier is still quite narrow. However, because of the fluctuations in the electron multiplication process in PMT, amplitude varies over a wide range.

In contrast to general assumption, signal from the PMT is used as a start pulse and the signal from the photodiode, corresponding to the laser pulse releasing the photon, is delayed and used as a stop signal. It is possible for some of the laser pulse periods to have no photons counted. If the triggering reference signal from photodiode were used as a start signal, some of the start signals would have no corresponding stop signal, leading to excessive dead time in the TAC and MCA. By delaying the laser pulses and using signals from the PMT to indicate start times, every start signal will be accompanied by a stop signal. As shown in Fig. 2.4, the TAC measures the time from the first accepted start signal to the next stop signal and any other start signal received in that time interval is ignored. The TAC is started when the leading edge of the

signal from the PMT just exceeds the discriminator threshold and the reference signal is properly delayed.

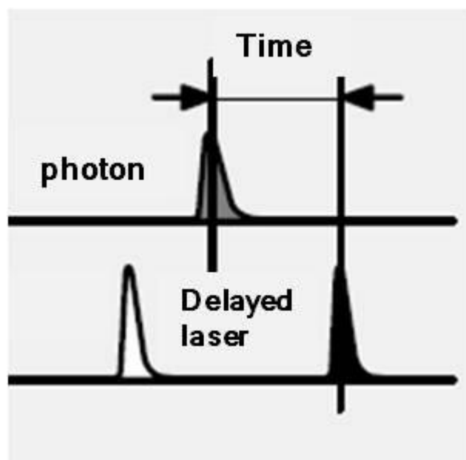

Fig. 2.4 Schematics of the photon pulse (TAC Start signal) and the reference laser pulse (TAC stop signal) in reversed start-stop mode (With permission from Ref. 56).

The measured temporal response is the convolution of the system response and the luminescence decay. System response may contain the pulse shape of the light source, temporal dispersion in the optical system, transit time spread in the detector, and timing jitter in the recording electronics. For samples with a very long decay lifetime, the system response doesn't affect significantly. However, for samples with fast decay lifetimes, the data has to be deconvoluted to measure the reliable recombination lifetime. System response can be measured in the same way by replacing the sample with a mirror and setting the monochromator to excitation laser wavelength. System response of our single photon counting system with the ultrashort laser pulses was measured to be ~20 ps as shown in Fig. 2.5.

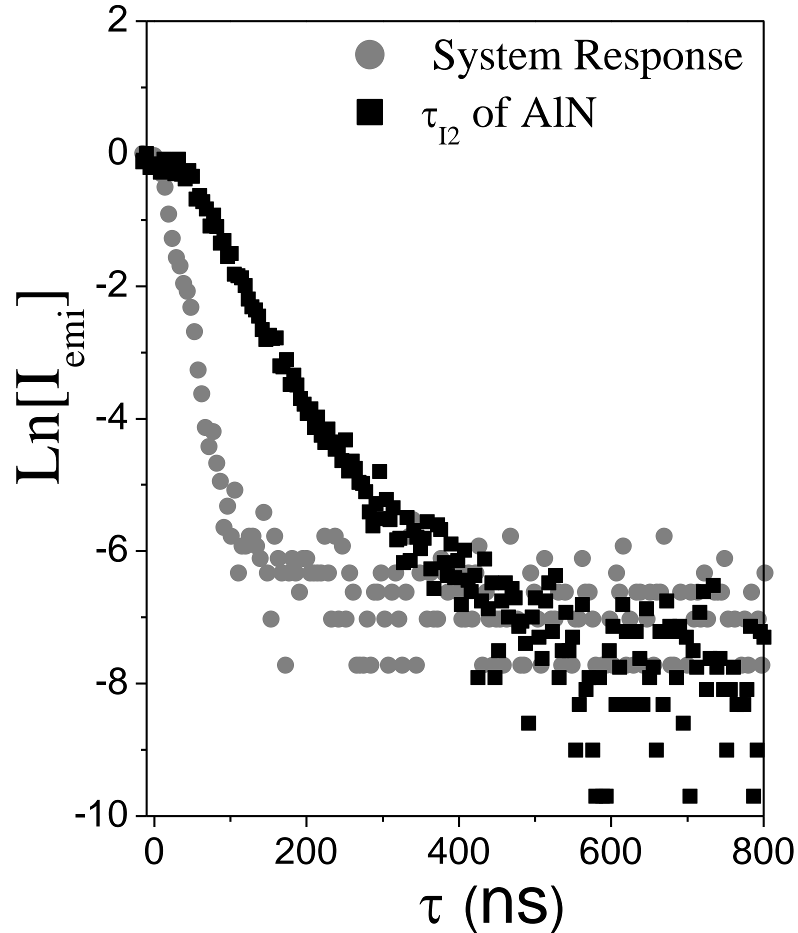

Fig. 2.5 System response (gray circles) and temporal profiles of donor-bound exciton transition (I_2) in AlN recorded with single photon counting system.

2.1.3.3 Streak camera

A streak camera was used to measure ultrafast phenomena like time resolved spectroscopy with the best possible time resolution. It is a two dimensional device with many detector channels working simultaneously. Analog video streak camera system C5680 from Hamamatsu, works in combination with ARC AM-511 monochromator. It measures the time variation of the incident light intensity with respect to the wavelength (time resolved

spectroscopy). The overall time resolution of the streak camera is 2 ps, which is better than that of the single photon counting system (20 ps). It has a built-in high sensitivity streak tube with a very high detection capability.

The streak camera converts the changes in temporal and spatial light intensity of the emitted photons into an image showing the brightness distribution on phosphor screen. Incident light is converted into electrons on the photocathode, the number of electrons being proportional

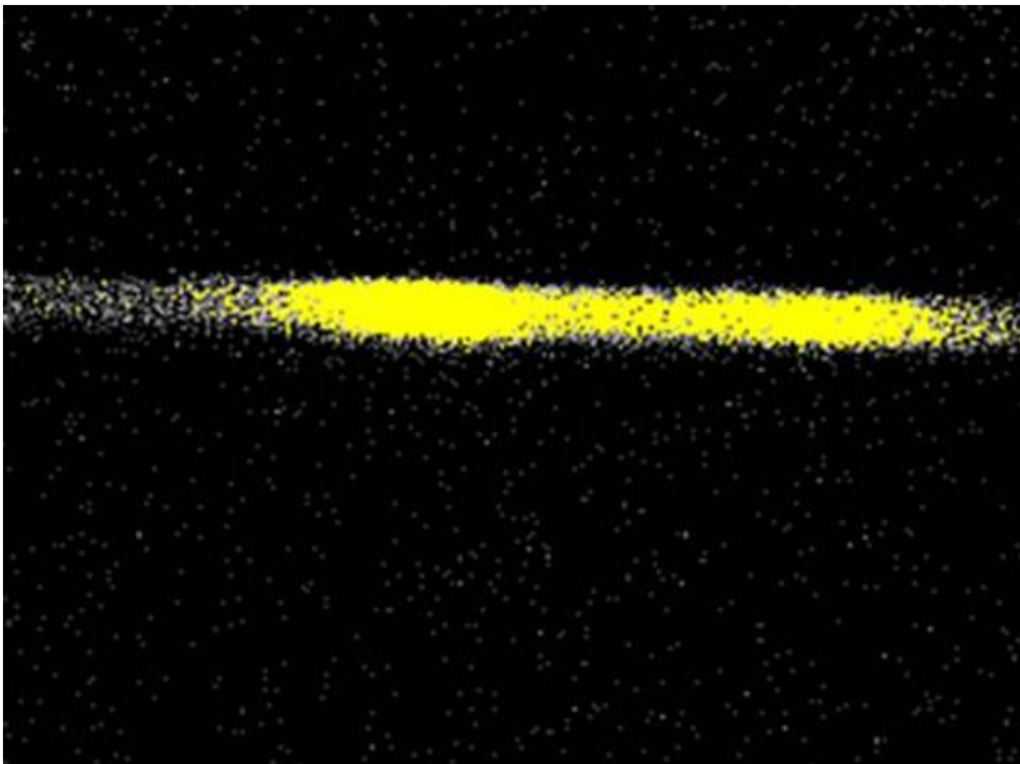

Fig. 2.6 Streak image of the bandedge transition in an AlN bulk crystal measured at 10 K.

to the light intensity. These electrons are accelerated by accelerating voltage and pass through the space between two sweep electrodes. These electrodes apply the sweep voltage in the vertical direction synchronized to incident light with magnitude varying with time so that the electrons

arriving later are deflected more from their horizontal direction relative to electrons arriving in the sweep field earlier. Deflected electrons enter the micro-channel plate (MCP) at different heights, are multiplied, and impact against a phosphor screen to form the phosphor image. Due to MCPs, the streak camera is capable of ultrahigh sensitivity with single photon detection capability that can be adjusted in a wide range (from x-ray to IR) just by selecting a suitable detector. A phosphor image corresponding to the earliest arrived optical pulse is placed on top and the subsequent images being arranged sequentially from top to bottom in the order of their arrival. The position of the phosphor image on a horizontal scale corresponds to the wavelength of the photon being detected. We can thus find the optical intensity from the brightness of the image and the time and wavelength from the location (pixel address) in the phosphor image. Fig. 2.6 shows an example of streak image recorded for the bandedge transition of AlN homoeilayer measured at low temperature.

2.1.4 Cryogenic system

Temperature is an important parameter in PL spectroscopy that provides an opportunity to measure characteristic activation energy of the system through thermal quenching (PL intensity, electrical resistivity) or thermal enhancement (carrier concentration) process, which is useful in the estimation of impurity level in semiconductor. Understanding the basic properties of semiconductors also requires measurements at cryogenic temperatures, which limit lattice vibrations and isolate the effects of impurities/defects in the crystal. Specific information about donor and/or acceptor centers can be obtained when carriers are frozen out in these states. At low temperatures, presence of defects or impurities is revealed, for example, through the inhibition of carrier mobility, which is clearly distinguishable from the values without or with less defects. At

higher temperatures (~300 K), in many cases, impurity scattering is not sensitive to the nature of donor/acceptor involved and mobility is dominated by lattice scattering. Furthermore, spectral broadening due to the involvement of phonon is significantly reduced at 10 K.

Cryogenics is the study of the generation of very low temperature (below -150 °C or 123 K) and its effect on behavior of materials. Cryogenic cooling is achieved using liquid nitrogen (77 K), liquid helium (4.2 K), or a cryocompressor (which uses high pressure helium lines). Liquid nitrogen is the most commonly used and is legally purchasable around the world, whereas liquid helium allows for reaching the lower temperatures. Various 4 K cryocoolers and higher capacity 10 K cryocoolers are widely available. The more advanced pulse tube technology are developed for vibration sensitive applications, such as micro-photoluminescence, micro-Raman spectroscopy etc. The most recent development in cryogenics is the use of magnets as regenerators as well as refrigerators. The magnetic refrigeration is a cooling technology based on the magnetocaloric effect. This technique can be used to obtain extremely low temperatures (well below 1 K), as well as the ranges used in common refrigerators, depending on the system design.

In this work, the temperature of test sample is varied anywhere between 10 and 900 K using SHI-APD cryogenic system. The cryogenic system consists of a helium compressor, the Expander, and two separate lines for the helium gas supply and return. The HC-4 MK2 compressor is a single-staged, water cooled, rotary compressor. It delivers high pressure, oil-free (99.995% pure) helium gas to DE-240SL Expander (cryogenic refrigerators). The compressor continuously draws low pressure helium from the system return line. The helium gas is compressed, cooled, and cleaned. High pressure oil-free helium gas is then delivered to the expander through the gas supply line. The gas supply and return lines use self-sealing bulkhead couplings. The cooling water supply and return lines use compression type bulkhead fittings for

3/8” tubing. A pressure gauge indicates gas supply pressure (280-300 psig at 68^{0}F). When the compressor is not running, the gauge shows the equalization pressure (240-245 psig). Automatic temperature control senses the compressor temperature, the overload switch opens the control circuit at a predetermined temperature, and resets automatically after cooling. A cable connected to a 28-socket receptacle mounted on the rear panel of the compressor supplies electrical power to the DE-204SL Expander. The Expander is a two stage cryogenic refrigerator that operates on the Gifford-McMahon refrigeration cycle using helium gas from a helium compressor to produce the cold temperatures. A sample holder is mounted to the second stage heat station and a radiant heat shield mounts to the first stage. Instrumentation feed throughs, vacuum pump out, and vacuum shroud (with transparent window material) are fastened to the skirt.

This system utilizes Lakeshore 331S temperature controller, which features two inputs with separate current source for sensing and one heater output. Sensor inputs are compatible with either diode/RTDs or thermocouples. It is typically factory configured for one diode/RTD input and one thermocouple input or both thermocouple inputs. The heater is a well-regulated variable DC current source optically isolated from other circuits. It provides up to 50 W of continuous power to a resistive heater load, and includes two lower ranges. Heater output is protected with short-circuit.

2.2 Material synthesis by MOCVD

Materials with good crystalline and optical quality for the modern electronic and optoelectronic applications can be synthesized by different methods including metal organic chemical vapor deposition (MOCVD), molecular bean epitaxy (MBE), physical vapor deposition (PVD) etc. MOCVD is an efficient method for the growth of thin film and layered structures of

high quality crystals. The samples of III-nitride material in this study were deposited by MOCVD with a horizontal quartz reactor. Basically, the MOCVD system consists of reactor, vacuum/exhaust system, and gas handling system built with metal-organic (MO) source chillers and the gas lines. Trimethyl aluminum (TMAl), Trimethyl gallium (TMGa), and blue ammonia (NH_3) were used as Al, Ga, and N precursors, respectively. Silane (SiH_4), bis-cyclopentadienylmagnesium (Cp_2Mg), and dimethyl zinc were used for Si, Mg , and Zn doping, respectively. Hydrogen (H_2) or nitrogen (N_2) was used as carrier gas in order to transport the precursors into the growth chamber. Flow rates of all the gasses were computer controlled via mass flow controllers. Film deposition occurs in the reactor chamber on a substrate, which sits on boron nitride (BN) coated graphite susceptor. The susceptor can be heated up to 1350 ^{0}C by a 10 kW RF generator (TIG-10/100). The growth temperature is controlled by a Eurotherm temperature controller (Model-904) and monitored by a R-type thermocouple. Interferometer is used for in-situ growth monitoring.

There are many growth parameters need to be otimized for achieving the desired material quality including temperature, pressure, V/III ratio etc. and the optimized values of these parameters vary for different materials.

2.3 Characterization tools

The quality of the synthesized material is monitored routinely using the following tools, which provide important feedback to guide the further material growth in appropriate directions.

2.3.1 Optical microscope

Optical microscope (OM) is an important tool to visually inspect the surface of the synthesized material, such as cracks, scratches, and cluster of particles in certain regions. It is quick and easy way to monitor as it doesn't require any sample preparation. A Nikon eclipse ME 600 microscope uses system of lenses to produce magnification so that features up to a few microns can be resolved.

2.3.2 Atomic force microscope (AFM)

Atomic force microscope (AFM) is one of various types of scanning probe microscopes (SPM) currently being employed for high resolution imaging. All SPMs are based on probing local properties, such as distance (force), optical absorption, magnetism, electric field etc. The resolution of SPMs is not diffraction limited. It is determined from the size of tip of the probe so that very high resolution is obtained by maintaining the small sample-probe separation and small tip size. AFM provides the topographical images by probing interatomic force between probe tip and sample surface. Therefore, it is equally applicable to metals, semiconductors, and insulators irrespective of its electrical conductivity. AFM Q-Scope 250 model from Quesant Company is used to monitor the surface morphology of the III-nitride photonic structures employed in this study. Sample is kept fixed and tip moves on sample surface. A highly flexible cantilever holds the tip. As tip scans through the sample surface, small defection of the cantilever deflects the laser beam more, which is detected by position sensitive photodetector. Based on the relative position of deflected beam on detector, feedback signal is calculated and sent to the piezoscanners to expand or retract so that constant distance (or force) is maintained between the tip and the sample. It gives vertical and lateral resolutions of about 1 and 10 A^0, respectively. In addition, AFM is used to assess the structural properties of the material by measuring the etch pit

density. It is used frequently to monitor the outcome of various steps during the device fabrication, such as feature dimensions, step formation in wageguide etc. Following figures show AFM images of AlN epilayers before and after growth optimization, which show that the surface of our optimized AlN is atomically flat.

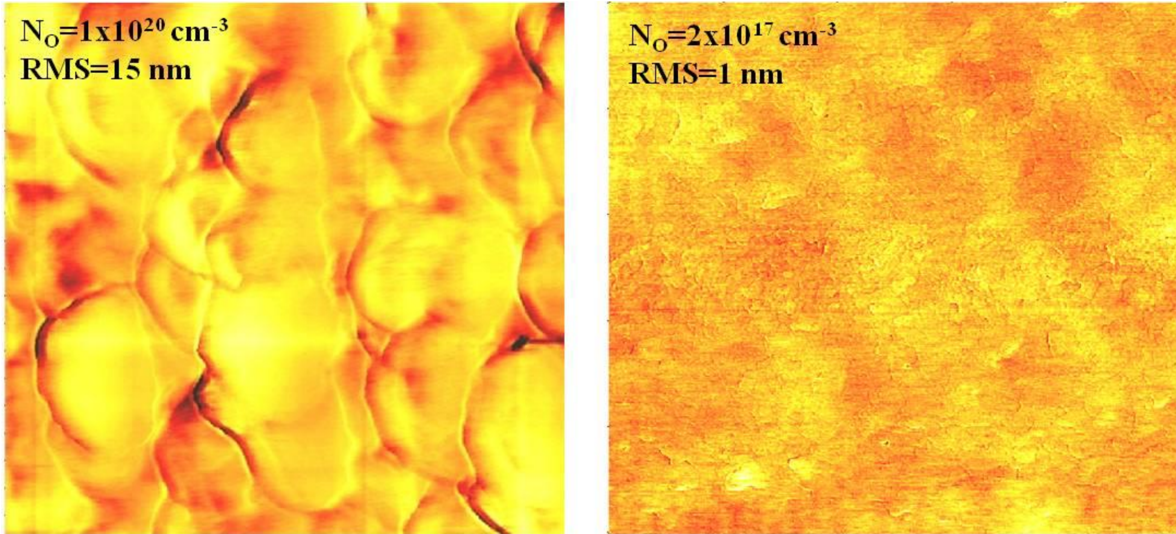

Fig. 2.7 AFM images of AlN epilayers with different concentrations of oxygen impurity (N_O) for a 2 μm x 2 μm scan area.

2.3.3 X-ray diffraction (XRD)

X-ray diffraction (XRD) is routinely used in order to estimate the alloy composition, asses the crystalline quality of material, and estimate strain in epilayers. The crystallinity is monitored through the XRD spectrum, such as the count rate of the diffracted X-rays, full width at half maximum (FWHM) of the rocking curve, and estimated TD densities. Diffracted X-rays from different atoms of the crystal interfere with each other resulting in interference maxima (diffraction peaks) with the same symmetry as in the distribution of atoms. When the

monochromatic X-rays of wavelength λ are incident on a crystal with the lattice planes of miller indices *hkl* and separated by a distance d_{hkl}, the condition for diffraction maxima can be described by Bragg's law

$$2d_{hkl}\sin\theta = n\lambda, \tag{2.1}$$

where θ is the scattering angle and n represents the order of diffraction. Inter-planer distance, d_{hkl}, can be calculated from the known λ and measured θ values by using the above equation. The lattice constants a and c of the hexagonal crystal are then estimated from the following equation.

$$\frac{1}{d_{hkl}^2} = \frac{4}{3}\frac{(h^2+hk+k^2)}{a^2} + \frac{l^2}{c^2}, \tag{2.2}$$

Measured lattice constant, a, can be employed to estimate the Al content (x) in the alloy by Vegard's law

$$a_{Al_xGa_{1-x}N} = xa_{AlN} + (1-x)a_{GaN}, \tag{2.3}$$

The in-plane stress ($\sigma_\parallel$) can be calculated by measuring the lattice constant of a strained epilayer (*a*), that of a strain free layer or the bulk material (a_0), and using the following relation

$$\sigma_\parallel = \frac{a-a_0}{a_0}\left(C_{11} + C_{12} - 2\frac{C_{13}^2}{C_{33}}\right), \tag{2.4}$$

where C_{ij} are the elastic constants of the material. The threading dislocation densities in the samples are estimated by knowing the tilt and twist angles, which are determined by measuring the FWHM for a family of lattice planes inclined at various angles relative to (002) lattice plane.

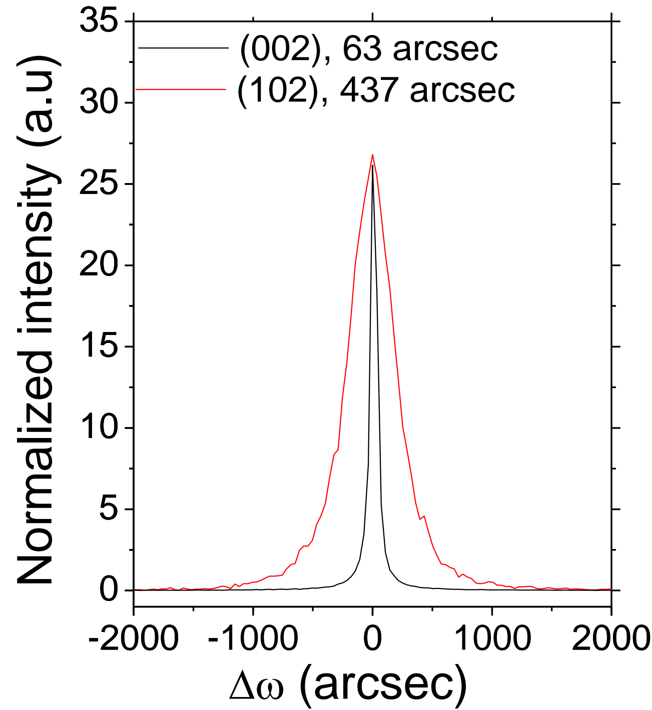

Fig. 2.8 XRD rocking curves of symmetric (002) and asymmetric (102) planes of AlN epilayer.

The XRD system being used in our lab is Rigaku – RINT2000V/PC series. The X-rays are produced from a sealed-off Cu X-ray tube with the characteristics wavelengths of 0.154056 nm and 0.154439 nm corresponding to Cu $K_{\alpha1}$ and Cu $K_{\alpha2}$, respectively. The peak arising from Cu $K_{\alpha2}$ is removed by using the software. Typical patterns of XRD rocking curves for symmetric (002) and asymmetric (102) reflection planes of our high quality AlN epilayers is shown in Fig. 2.8. The full width at half maximum (FWHM) of (002) and (102) peaks were observed to be 63 and 437 arcsec, respectively.

2.3.4 Photoluminescence (PL)

In addition to its application in very detailed optical studies, photoluminescence is also used to characterize the semiconductors, semiconductor hetero-structures, and fabricated devices

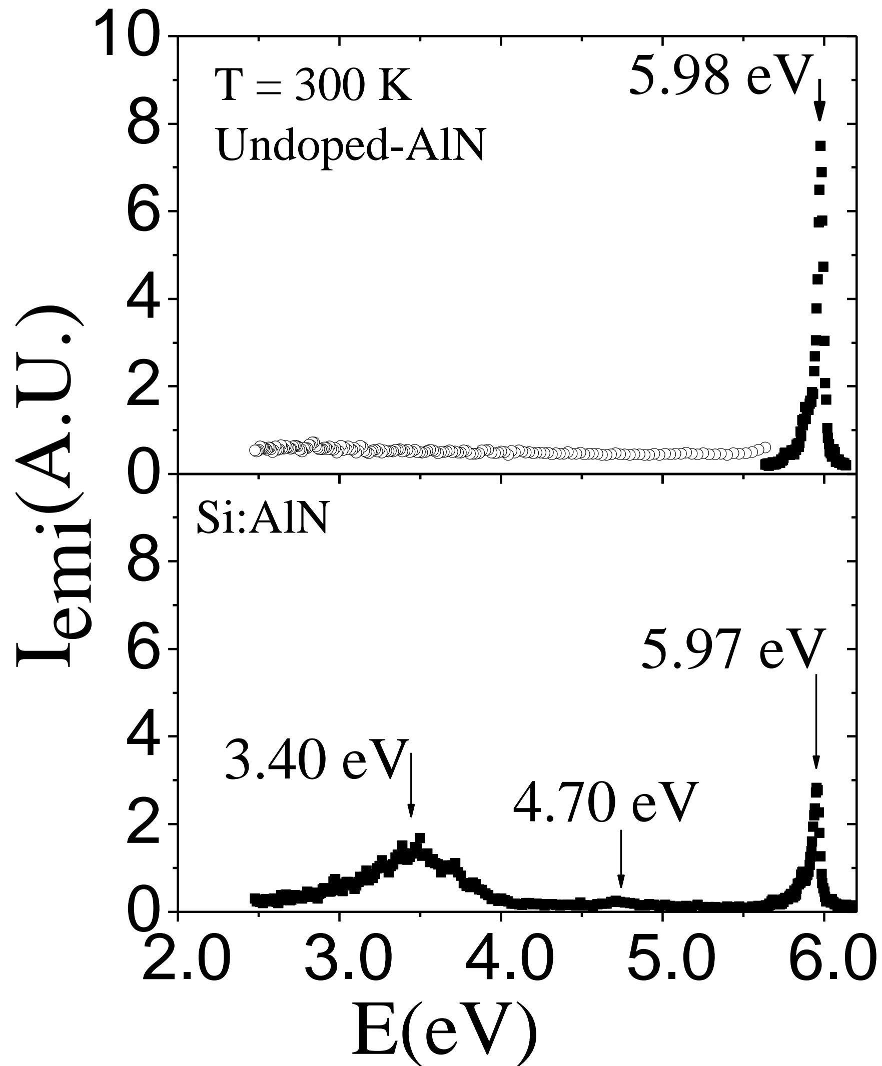

Fig. 2.9 Room temperature (300 K) PL spectra of undoped- (top) and Si-doped (bottom) AlN epilayers.

on daily basis. PL spectra measured at room temperature (300 K), and sometimes at low temperature (10 K), are the diagnostics of semiconductors in most cases, which provide the feedback very quickly and non-destructively. PL becomes very important, especially for wide bandgap materials such as AlN and Al-rich AlGaN alloys, because the electrical characterization is difficult to be employed in many cases due to their insulating nature and structural studies do not reveal the information on native point defects in the materials. Monitoring the relative intensities of various transitions in near band-edge region and that involving deep level donors or acceptors is an excellent way of assessing the optical quality of the material, which is correlated with the crystalline quality of the materials. Over the last few years, we have established PL as an efficient tool providing an opportunity to study the structural properties of materials, such as strain in epilayers, concentration of native point defects, and that of dislocations.

2.3.5 Secondary ion mass spectroscopy (SIMS)

Incorporation of impurities, such as C, O, and Si, from the environment appears to be an unavoidable problem in MOCVD growth in many cases. In order to determine the impurities in the epilayers, which includes the intentionally doped elements and unintentionally incorporated impurities with concentration $<1\%$ of the host atoms, secondary ion mass spectroscopy (SIMS) is the most sensitive analysis technique. In SIMS measurement, sample is bombarded with energetic primary ions, which eject the beam of secondary ions. The secondary ions are detected with the mass spectrometers and analyzed for their chemical identity. The profile of oxygen (O) and carbon (C), impurity concentrations as functions of depth, in one of our undoped AlN epilayer from SIMS measurement is shown in Fig. 2.10.

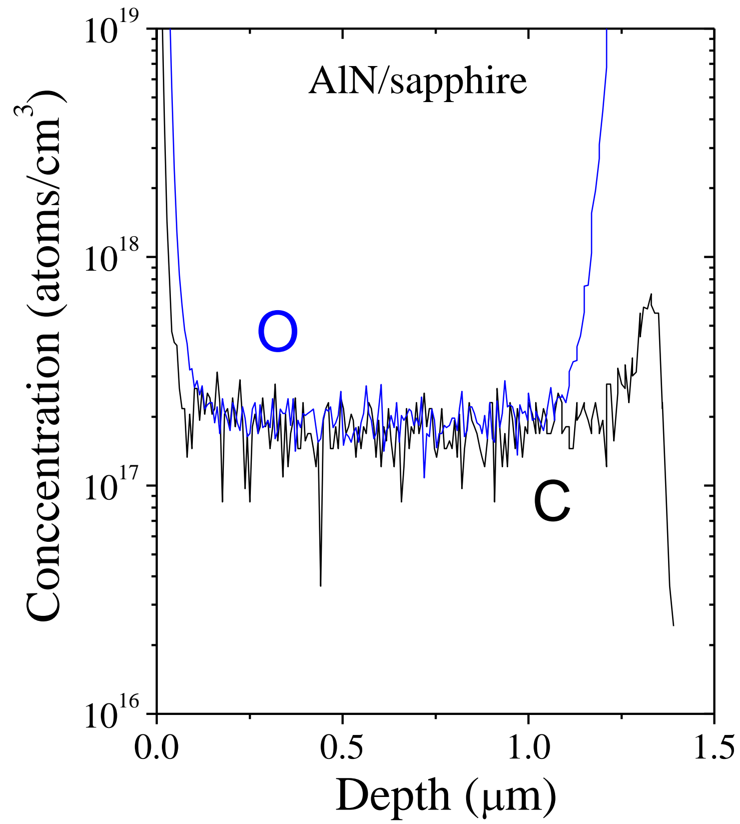

Fig. 2.10 SIMS results showing the depth profiles of O (blue line) and C (black lines) in one of the AlN epilayers.

Chapter 3 - Experimental results and discussions

3.1 Valence band structure of AlN probed by photoluminescence

AlN has the widest direct band gap (~6.1 eV) among the nitride semiconductors and offers a continuous band-gap variation through the alloying and heterostructure design with GaN and InN. It is an ideal material for the development of UV-light sources (detectors) operating in the wavelength range down to 200 nm. The electrical and optical properties of semiconductors are mainly determined by the electronic band structure near the Γ point. Information regarding the band structure of AlN is fundamentally important for the understanding of the basic properties of AlN and its device applications. Due to an increasing interest in AlN in recent years, several theoretical [3,57,58] and experimental [59-61] studies on the fundamental optical properties of AlN have been reported.

The valence band of wurtzite (WZ) III-nitrides with Γ_{15} symmetry splits into three levels (*A*, *B*, and *C* valence bands in the order of increasing emission energies). Hexagonal symmetry of the WZ structure induces crystal-field splitting into two-fold degenerate Γ_6 state and nondegenerate Γ_1 state [3,62]. Spin-orbit interaction further splits Γ_6 state into Γ_9 and Γ_7 states. Magnitude and nature of crystal-field splitting parameter (Δ_{CR}) in WZ AlN depend on deviations of its lattice constants' ratio c/a and internal u parameter from their values for an ideal WZ structure [57]. AlN has a large negative Δ_{CR} [62,63], so that the energy level of Γ_1 is higher than that of Γ_6. By examining GaN and all other semiconductors with WZ structure, we notice that Δ_{CR} is generally small and positive so that the energy level of Γ_6 is always higher than that of Γ_1 [64]. This unusual ordering of the valance bands gives rise to unique optical properties of AlN. The recombination of excitons associated with the *A*, *B*, or *C* valence bands has different

probabilities for different polarizations of absorbed or emitted light [3]. The emission spectrum in AlN has a dominant Π-polarized (**E**||**c**) emission [3,64] in contrast to dominant σ-polarized (**E**⊥**c**) emissions in GaN [64]. These optical polarization properties may be exploited for polarization filtering, polarized emission in AlN based light emitting diodes, polarization-sensitive photodetectors, and AlN based TM mode laser in the future.

The *A* exciton transition in AlN was experimentally observed by photoluminescence (PL) and cathodoluminescence (CL) measurements [59,64]. There were several reports from optical reflectance measurements on the observation of *A*, *B*, and *C* excitonic transitions [60-62]. However, the *B* and *C* excitonic transitions have never been observed directly by PL measurement. Recently, by increasing the thickness of the epilayers, we have achieved AlN epilayers with a reduced dislocation density. The fabricated metal-semiconductor-metal photodetectors based on these AlN epilayers exhibited a peak responsivity at 200 nm with a sharp cutoff at a wavelength of 207 nm and extremely low dark currents (~50 fA at 300 V) [65,66]. In this work, we report on the studies of the valence band structure of AlN based on the observation of three well resolved excitonic emission peaks in high quality AlN epilayers directly probed by polarization resolved PL.

AlN epilayers with a thickness of 4 μm were grown on *c*-plane sapphire substrates by MOCVD [65]. Deep UV PL measurement was employed to probe the excitonic transitions and the polarization of emitted light. The excitation light source was a frequency quadrupled Ti-sapphire laser (with more than 90% vertical polarization), 76 MHz repetition rate, 100 fs pulse width, and photon energy set around 6.29 eV [67]. The collected emission was dispersed by a 1.3 m monochromator. The sample was held in a stage with its *c* axis (**c**) pointing in the direction perpendicular to the sample surface and the excitation laser was incident at very small

angle with respect to the sample surface, as illustrated in the inset of Fig. 3.1(a). A polarizer was used in front of the slit of the monochromator to resolve **E**∥**c** (Π) or **E**⊥**c** (σ or α) components.

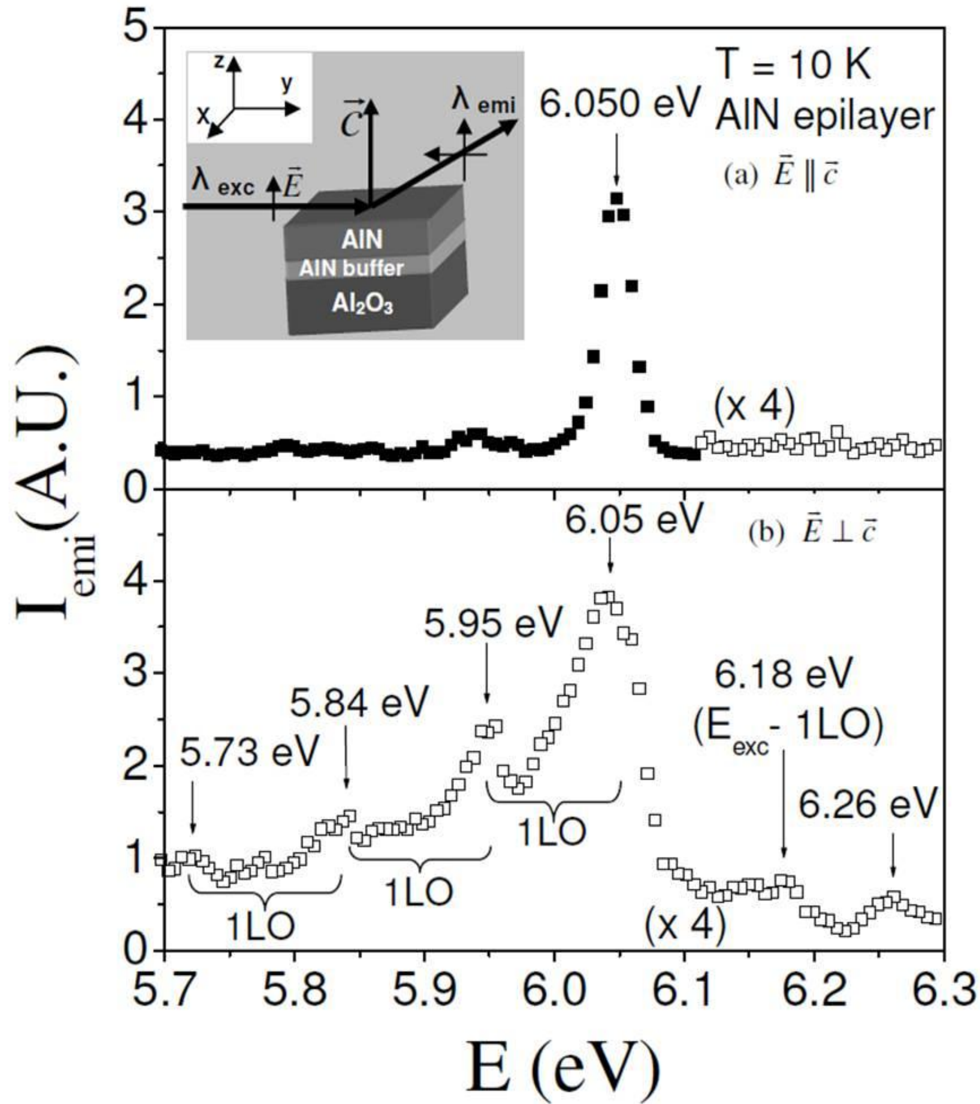

Fig. 3.1 Low temperature (10 K) PL spectra of an AlN epilayer measured under different polarization configurations with (a) **E**∥**c** and (b) **E**⊥**c**. Schematic diagram of the measurement setup is shown in the inset of (a).

Fig. 3.1 compares the low temperature PL spectra of an AlN epilayer collected for the emitted light with electric field component (**E**) (a) parallel (**E**||**c**) and (b) perpendicular (**E**⊥**c**) to the *c* axis. The intensity of the emission peak at 6.050 eV for the **E**||**c** polarization is much stronger than that for the **E**⊥**c** polarization. The emission lines at 5.95, 5.84, and 5.73 eV in Fig. 3.1(b) marked as 1 LO, 2 LO, and 3 LO are one, two, and three phonon replicas of the dominant 6.05 eV emission line in AlN with a LO phonon energy of about 110 meV. The peak at 6.18 eV is the Raman line due to the excitation laser set at 6.29 eV. The dominant emission line at 6.05 eV has a linewidth of about 29 meV. Previous theoretical calculation [59] showed that the *A* valence band related band-edge transition in AlN is allowed only for the **E**||**c** polarization and almost forbidden for the **E**⊥**c** polarization. Therefore, spectral peak position, line width, and observed relative intensities of two polarization resolved measurements suggest that the 6.05 eV peak is due to the recombination of *A*-free excitons (*A*-FX). Using the binding energy of *A*-FX in AlN of 80 meV, the band gap of AlN is (6.05+0.08 eV) = 6.13 eV at 10 K, which is consistent with the previously reported values [18,48,68]. A slight variation in the FX emission peak position from previous reports is due to different magnitudes of stress in different samples caused by variations in growth conditions, layer thickness, etc [69].

For the **E**⊥**c** orientation shown in Fig. 3.1(b), in addition to the 6.05 eV peak, there is another emission line at a higher energy position near 6.26 eV, which is absent in the **E**||**c** measurement configuration. In Fig. 3.2, we replot the same emission spectrum of Fig. 3.1(b) in a narrower spectral range from 6.20 to 6.35 eV with higher resolution. Two peaks at 6.249 and 6.262 eV are clearly resolved only for **E**⊥**c** polarization. These two peaks are separated by 13 meV. Previous theoretical calculations [3,57] have predicted that the energy separation between the *B* and *C* valence bands is 13 meV and that between the *A* and *B* valence

bands is ~211 meV. The observed peak at 6.249 eV in Fig. 3.1(b) is about 199 meV higher than the *A*-exciton peak at 6.050 eV. Therefore, based on the calculations, observed spectral peak positions and relative emission intensities in two different polarization orientations, we assign the emission peaks at 6.249 and 6.262 eV to the *B* and *C* exciton recombination, respectively. These two emission bands have not been previously observed by PL measurements. We believe that improved crystalline quality of AlN epilayers makes their observations possible.

A previous optical reflectance measurement revealed a spectral peak position at about 6.029 eV for the *A*-FX transition in AlN bulk crystals [61], which matches perfectly with that in AlN homo-epilayers obtained by PL measurements [69] and represents the *A*-FX transition peak in stress-free AlN. It was not possible to fully resolve the peak positions of *B*- and *C*-exciton transitions by the optical reflectance measurement but careful fitting suggested positions at 6.243 and 6.268 eV, respectively [61]. The *A*- and *B*-exciton emission peaks observed here (in a 4 μm thick AlN/Al_2O_3 epilayer) are blueshifted by 21 and 6 meV, respectively, with respect to the stress-free AlN due to a compressive strain, while a blueshift for the *C*-exciton transition is absent based on this optical reflectance measurement [61]. A separate optical reflectance/transmission measurement on AlN with various crystal orientations revealed that the *A*, *B*, and *C* excitons have transition energies of 6.025, 6.243, and 6.257 eV in stress-free AlN [60], which implies that the *A*, *B*, and *C* exciton emission lines observed here (in a 4 μm thick AlN/Al_2O_3 epilayer) are blueshifted by 25, 6, and 5 meV, respectively, with respect to the stress-free AlN due to a compressive strain. The results seem to suggest that the effects of strain on *B* and *C* valence bands are less pronounced than that on the *A* valence band. However, the effects of strain on *B*- and *C*-valence bands are still ambiguous at this point. We are unable to deduce the binding energies of the *B* and *C* excitons in AlN based on the present experimental

data. However, excitons associated with the *A*, *B*, and *C* valence bands have almost the same binding energies in GaN [70]. Therefore, we assume that the *B* and *C* excitons in AlN have the same binding energy as that of the *A* exciton. This gives the bandgap of AlN to be (6.249+0.080)=6.329 eV and (6.262+0.080)=6.342eV for the *B* and *C* valence bands, respectively.

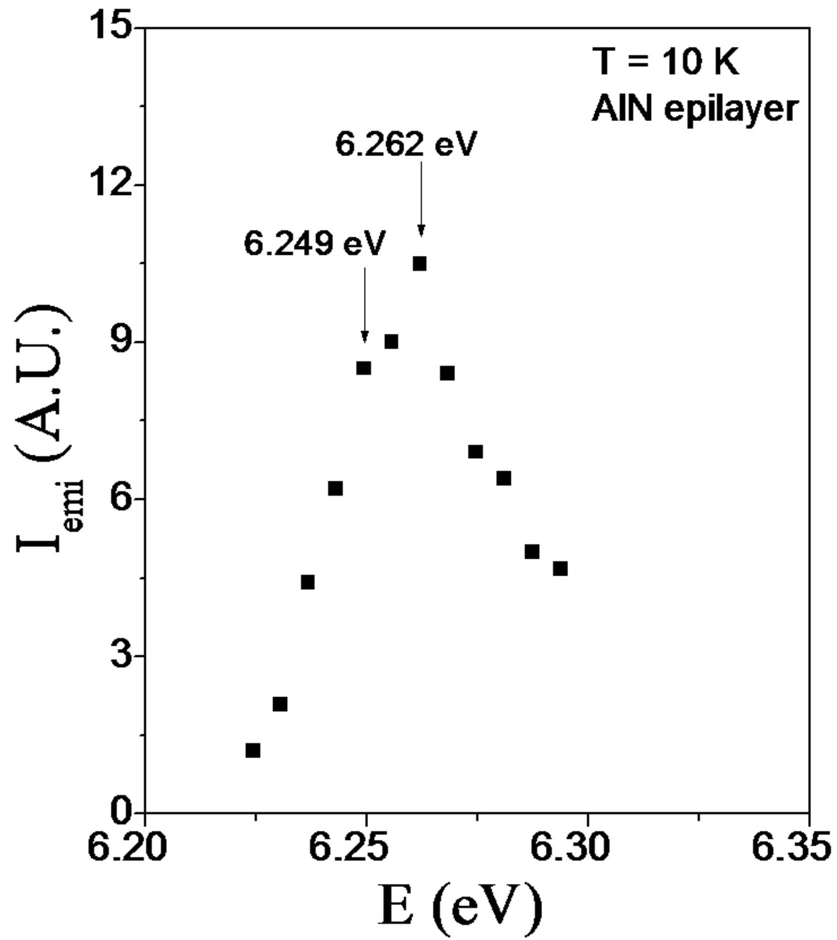

Fig. 3.2 Low temperature PL spectra of an AlN eppilayer for **E⊥c** polarization in narrow spectral range.

Based on the results shown in Fig. 3.1, we have constructed in Fig. 3.3 the energy band structure of AlN near the Γ point. The corresponding optical transitions are illustrated by downward arrows. Polarization properties of emitted light are different depending on which of the valence bands are involved in the recombination. Recombination of the *B* and *C* excitons are allowed in the **E⊥c** polarization configuration and forbidden in the **E∥c** polarization configuration, which is in contrast to the *A* exciton recombination that is allowed mainly in the **E∥c** polarization configuration and almost prohibited in the **E⊥c** polarization configuration. According to Hopfield's quasicubic model for WZ crystals [71], excitonic emission energies and valence band splitting parameters are related by

$$E_{A/C} = E_B + \frac{\Delta_{SO}+\Delta_{CR}}{2} \mp \sqrt{(\frac{\Delta_{SO}+\Delta_{CR}}{2})^2 - \frac{2}{3}\Delta_{SO}\Delta_{CR}}, \quad (3.1)$$

where $E_{A/C}$ (E_B) are the emission energies from the band-to-band transitions related to *A*/*C* (*B*) valence bands, respectively. Using our experimentally observed values of E_A=6.050 eV, E_B=6.249 eV, and E_C=6.262 eV, we deduce Δ_{CR}=−206meV and Δ_{SO}=20 meV for AlN epilayer grown on sapphire substrate.

Values of ΔE_{AB}, ΔE_{BC}, Δ_{CR}, and Δ_{SO} from previous theoretical calculations and experimental observations are summarized in Table 1 along with respective methods of experiments. Bearing in mind that different amounts of strains involved for AlN epilayers grown on different substrates with varying thicknesses, our data agree well with majority of the reported experimental and calculated values. The intensities of these two emission lines are relatively weak, which seems reasonable. Typically, transitions involving higher bands such as the *B* and *C* valence bands are very difficult to observe due to a much lower population of free holes, in

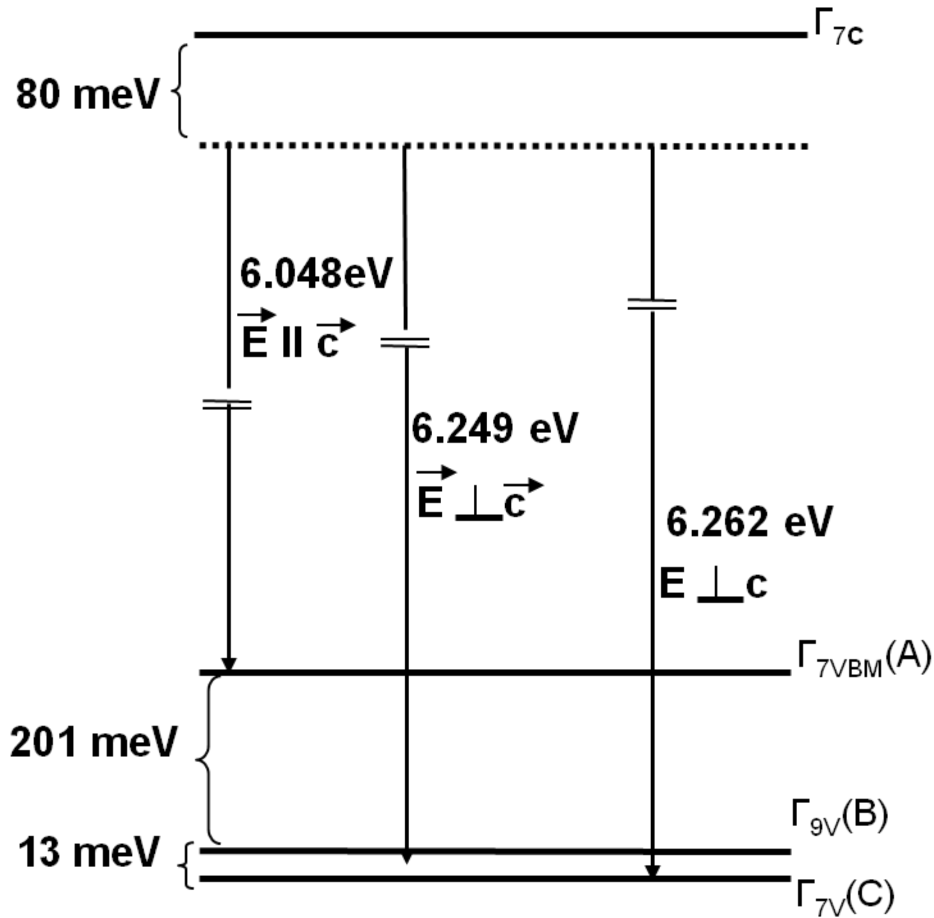

Fig. 3.3 Energy level diagram of AlN near the Γ-point constructed from the low temperature PL measurement results.

consistence with the statistical distribution [72]. The free hole concentration is much higher in the *A* valence band. However, in the case here, the transitions from the *B* and *C* valence bands are enhanced due to the unique polarization properties of these bands in AlN. Nevertheless, other

complementary measurements such as high resolution optical absorption measurements may be needed in order to further confirm the energy positions of *B* and *C* exciton transitions.

Table 3.1 Theoretically calculated and experimentally observed spin-orbit splitting parameter (Δ_{SO}), crystal-field splitting parameter (Δ_{CR}), energy spacing between the A and B valence bands (E_{AB}), and the B and C valence bands (E_{BC}) in WZ AlN.

Δ_{SO} (meV)	Δ_{CR} (meV)	ΔE_{AB} (meV)	ΔE_{BC}(meV)	Notes
	--219	213	13	Calc. (Ref. 1)
19	-217	211	13	Calc. (Ref. 4)
19	-224	218	19	Calc. (Ref. 5)
	-237	E_A = 5.981 (5.985) e V 6.22 eV -B,C Unresolved		OR (CL and PL) AlN : Si / SiC (Ref. 6)
	-230	E_A = 6.024 e V 6.25 eV – B,C Unresolved		OR (m-face bulk AlN) (Ref. 7)
36	-225	234	25	OR (AlN bulk) (Ref. 8)
22	-210	201	13	This work (AlN / Al_2O_3)

Calc. : Calculation, OR : Optical Reflectivity measurement, CL : Cathodoluminescence
E_A, E_B, E_C : Emission energies corresponding to A, B and C valence bands

In summary, we have investigated the valence band structure of AlN near the Γ point by polarization resolved deep UV PL measurements. Three different emission lines have been observed. As expected, the *A* valence band related excitonic emission at 6.050 eV with **E||c** polarization dominates the spectrum. The observed *B* and *C* valence bands related excitonic emissions at higher energy positions of 6.249 and 6.262 eV are polarized in the **E⊥c** direction. From these results, the crystal-field and spin-orbit splitting parameters are

deduced, which agree well with previous reported results. We believe that the present results provide a more coherent picture for the valence band structure of the WZ AlN.

3.2 Photoluminescence properties of AlN homoepilayers

AlN has a complete solid solubility with GaN (Ref. 73) and emerged as an important semiconductor material for applications in light emitters down to 200 nm (Ref. 51) and detectors in the deep ultraviolet (DUV) and extreme UV spectral region [11,74]. Quantum wells (QWs) have been the device structure of choice for efficient III-nitride semiconductor based light emitters [75,76]. Conventional nitride *c*-plane multiple QW structures generate fixed sheet charges at the interfaces due to the spontaneous and piezoelectric polarization [15,77-79], which induce internal electric fields, lead to carrier separation, and reduce the radiative recombination rate. Consequently, optoelectronic devices such as light emitting diodes and laser diodes based on heteroepitaxial *c*-plane oriented III-nitride materials possess reduced internal quantum efficiencies.

There has been tremendous effort in the investigation of nonpolar *a*-plane and *m*-plane III-nitride epilayers [80] and optoelectronic devices with QW structures [78,79] to reduce the effects of internal electric fields. To achieve QW and other heterostructure based devices with improved performance, optical properties of epilayers grown on different orientations of available substrates have to be better understood. Furthermore, most previous studies on the fundamental band structures of AlN have been carried out for heteroepilayers grown on sapphires. These epilayers are plagued by lattice mismatch induced strain and high threading dislocation density, which significantly inhibited our ability for precisely determining the fundamental band structure parameters of AlN. In this work, we report a systematic comparative study of optical properties of both homoepitaxial and heteroepitaxial layers of AlN grown on polar *c*-plane as well as non-polar *a*-plane and *m*-plane orientations probed by DUV photoluminescence (PL).

AlN bulk single crystal substrates were produced by sublimation crystal growth using polycrystalline AlN wafer as seeds and have a thickness of about 1 mm and an average grain size of about 2×3 mm^2 [81]. The surface of AlN bulk crystal substrates was prepared by chemical mechanical polishing (done by NovaSiC) that provided a surface roughness of about 1–4 nm. The dislocation density in AlN bulk single substrates was below 1×10^6 cm^{-2} as determined by synchrotron white beam x-ray topography [82]. The 1 μm thick undoped AlN epilayers were grown on *c*-plane, *a*-plane, and *m*-plane bulk AlN and *c*-plane and *r*-plane sapphire substrates by MOCVD. A low temperature AlN nucleation layer was deposited at 500 °C prior to the deposition of AlN heteroepitaxial layers on sapphire, while the nucleation layer was eliminated for the growth of homoepilayers. The AlN epilayers were grown at 1300 °C and a V/III ratio of 50 was employed for all samples. Trimethylaluminum and ammonia were used as Al and N sources, respectively. The PL spectra were measured with a DUV laser spectroscopy system that consists of frequency quadrupled 100 fs Ti-sapphire laser with 76 MHz repetition rate and photon energy set around 6.30 eV. Since the optical absorption coefficient in AlN for the above band gap excitation is typically $>10^5$/cm [83], such an excitation scheme provides a typical optical absorption depth of <0.1 μm, which is much smaller than the epilayer thickness (1 μm). Hence the measured PL emission was purely from the epilayer.

Fig. 3.4 compares the low temperature (10 K) PL spectra of AlN homoepilayers with three different orientations (*a*-plane, *c*-plane and *m*-plane) (a) in a broad spectral range from 2.0 to 6.2 eV and (b) in a narrower spectral range from 5.8 to 6.2 eV. We observed weak and deep impurity related emission bands centered around 2.9 eV and 4.4 eV from the *m*-plane sample related to O impurities [84] and at 4.70 eV in *a*-plane sample related to Al vacancy complex with one negative charge state [45], (V_{Al}-complex)$^{1-}$. However, the intensities of these

impurity transitions are less than 1% of the corresponding band-edge emissions, which confirms the high optical quality of our AlN homoepilayers.

Fig. 3.4(b) shows the dominant peak at 6.008 (6.007) eV in *c*-plane (*a*-plane) homoepilayer due to the donor bound exciton transition (I_2), while the 6.025 eV peak due to the free exciton transition (FX). I_2 is about 17 meV below FX, which is the binding energy of the donor bound excitons in AlN and agrees well with the previously reported value. Fig. 3.5 shows the Arrhenius plot of the PL intensity of the high energy peak (6.025 eV at 10 K) measured in *a*-

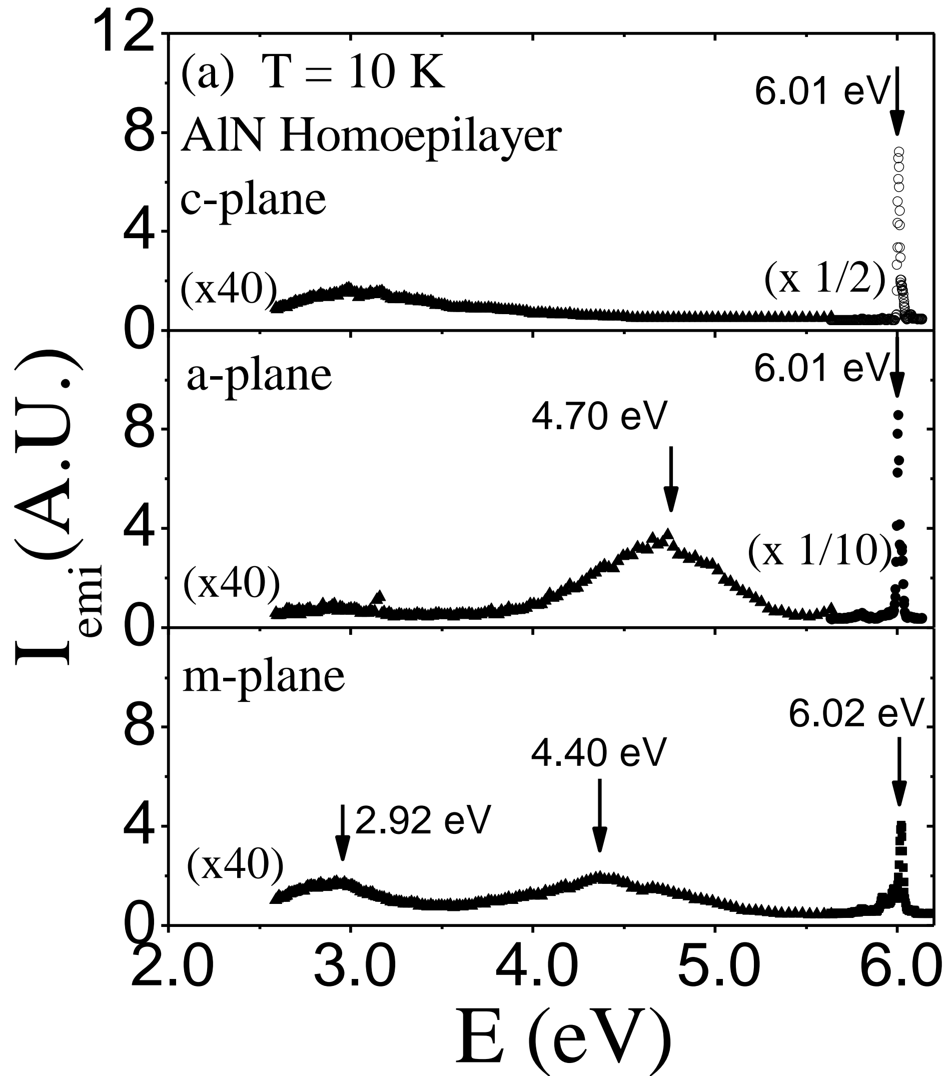

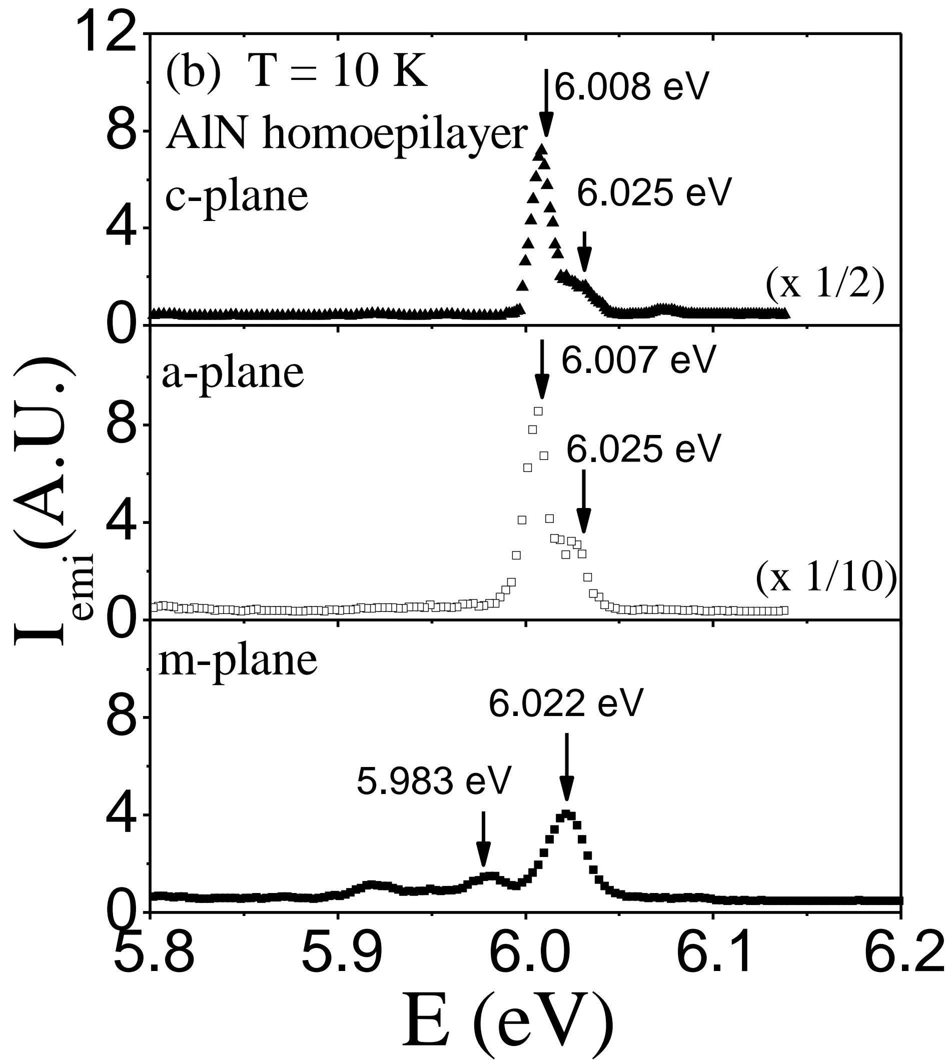

Fig. 3.4 Low temperature (10 K) PL spectra of c-plane, a-plane, and m-plane AlN homoepilayers measured in (a) wide spectral range from 2 to 6.2 eV and (b) narrow spectral range from 5.8 to 6.2 eV.

plane AlN homoepilayer. The inset of Fig. 3.5 shows the temperature dependent PL spectra. The solid line is the least squares fit of data with the equation

$$I(T) = \frac{I_0}{1+Ce^{-E_0/K_BT}}, \quad (3.2)$$

The fitted value of E_0 is 74 meV, which is close to the previously reported value of 78 meV for the binding energy of FX in AlN/Al_2O_3 and further corroborates our assignment of a FX transition for the 6.025 eV peak. In *m*-plane homoepilayers, there is only one dominant FX transition at 6.022 eV and no observable I_2 transition. The 5.983 eV peak in this sample is 4LO of excitation laser. We thus conclude that all AlN homoepilayers (*c*-plane, *a*-plane, and *m*-plane) have almost identical FX peak positions (varying only slightly between 6.022 and 6.025 eV) at 10 K. No I_2 emission is visible in *m*-plane AlN. This implies a smaller amount of unintentional donor impurity incorporation during epigrowth into *m*-plane films than *a*-plane and *c*-plane films. This observation is consistent with a previous study, which revealed that the oxygen incorporation on *m*-plane is 1% of that on *c*-plane of the sublimation grown AlN bulk crystals [85].

The PL properties of AlN homoepilayers and heteroepilayers grown in different orientations are summarized in Table 3.2 for comparison. The near band-edge emission spectra measured in all *a*-plane, *c*-plane, and *m*-plane AlN homoepilayers at 300 K exhibit only one peak at an energy position of 5.961 eV due to the FX transition, which lines up exactly with the FX peak position in AlN bulk crystals. All homoepilayers, therefore, are nearly stress free and the band gap of strain free AlN is thus (6.025+0.074) eV = 6.099 eV at 10 K and (5.961+0.074) eV = 6.035 eV at 300 K. This conclusion is further corroborated by the x-ray (XRD) measurements of the lattice parameters. For example, the spectral peak positions of $\theta/2\theta$ scans of both the symmetric (002) and asymmetric (102) reflection peaks of a *c*-plane AlN homoepilayer and AlN

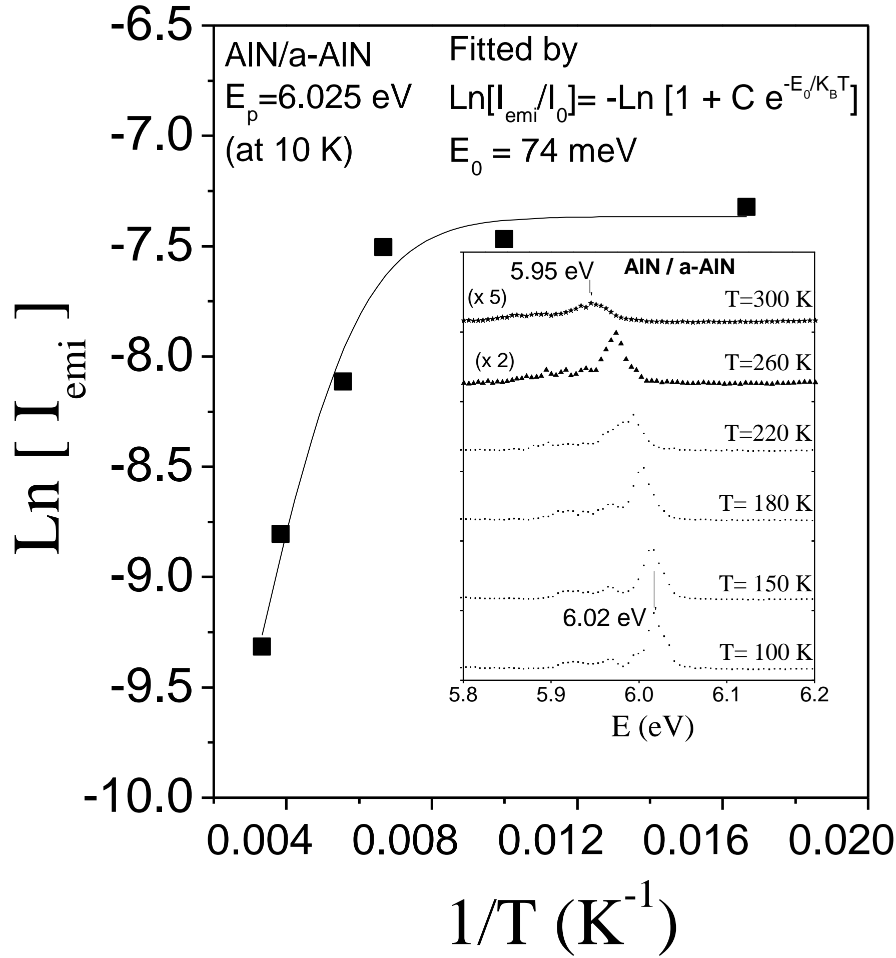

Fig. 3.5 The Arrhenious plot of the PL intensity [Ln (I_{emi}) vs 1/T] of FX transition (6.025 eV at 10 K) for a-plane AlN homoepilayer. The solid line is the least square fit of the data with Eq. (1). The inset shows the temperature dependence of the band-edge emission between 100 and 300 K.

bulk substrate exactly line up revealing an in-plane lattice constant of a = 3.112 Å, which also indicates that the AlN homeepilayer is perfectly lattice matched to the AlN bulk substrate and is almost strain free [69].

The band-edge emission peak intensity ratio for *a*-plane, *c*-plane, and *m*-plane AlN homoepilayers is approximately 32:5:1. Due to the unique band structure of AlN near the Γ point, the PL intensity in *a*-plane AlN is enhanced by the fact that AlN exhibits a maximum emission in the directions perpendicular to the *c* direction (or in the **E**//**c** measurement geometry) [64]. In our measurement, the *c* direction of *a*-plane AlN lies in the substrate plane so that the maximum emitted light propagation direction is normal to the surface. Thus, optoelectronic devices with *a*-plane homoepilayers in their active region can exploit optimum quantum efficiency.

Fig. 3.6 shows the 10 K PL spectra of a *c*-plane AlN epilayer grown on *c*-sapphire and *a*-plane AlN epilayers grown on *r*-plane sapphire and also on *a*-plane bulk AlN (a) covering a broad spectral range from 2.0 to 6.2 eV and (b) in a small spectral range from 5.8 to 6.2 eV. The near band-edge emission spectra of an AlN epilayer grown on *c*-plane (*r*-plane) sapphire has two peaks at 6.063 (6.030) and 6.045(6.013) eV, corresponding to the recombination of FX and I_2 [45]. Clearly the FX emission peak in *a*-plane AlN heteroepilayer is about 33 meV lower than that in *c*-AlN heteroepilayer. This implies that the strain induced by lattice mismatch between AlN and sapphire substrate is almost relaxed by simply switching the growth to *r*-plane. However, compared with homoepilayers, the unique band structure induced enhancement in the band-edge emission intensity is absent in *a*-plane AlN heteroepilayers due to the presence of high dislocation density because the growth technology for *a*-plane AlN epilayers is still far from maturity. This interpretation is consistent with three other observations: (1) the FX emission linewidth is narrower in *c*-plane AlN heteroepilayers than that in *a*-plane hetero-epilayers; (2) the presence of a much higher concentration of Al vacancies in *a*-plane AlN heteroepilayers; (3) the full width at half maximum of XRD rocking curve of the asymmetric (102) reflection peak of *c*-

plane AlN heteroepilayers (400 arcsec) is much narrower than that of the (110) reflection peak of *a*-plane AlN heteroepilayers (940 arcsec).

Table 3.2 Comparision of PL emission properties of a-, c-, and m-plane AlN homo-epilayers, c-AlN/c-Al_2O_3, and a-AlN/r-Al_2O_3 hetero-epilayers including PL peak position (E_p), PL peak intensity (I_p), full width at half maximum (FWHM), and binding energy (BE) at 10 K and 300 K.

		Transition type	T=10 K				300 K
			E_p (eV)	I_p (a.u.)	FWHM (meV)	E_0 (meV)	E_p (eV)
		FX	6.025	24	16.0	74	5.961
Homoepilayers	*c* plane	I_2	6.008	136	13.1	17	
	a plane	FX	6.025	320	13.0	74	5.961
		I_2	6.007	820	11.6	18	
	m plane	FX	6.022	35	21.0	···	5.961
		FX	6.063	89	22	78	5.984
		I_2	6.045	63	19.2	18	
Heteroepilayers		FX	6.030	38	33	···	5.956
(Sapphire)		I_2	6.013	23	20	17	
AlN bulk	*c* plane	FX	···	···	···	···	5.961

We can also make a comparison between emission spectra of *a*-plane homoepilayers and heteroepilayers. As seen in Fig. 3.6, the near band-edge spectrum of *a*-plane AlN homoepilayer exhibits an emission peak at 6.025 eV due to the FX recombination, which is only about 5 meV below that in *a*-plane AlN heteroepilayer, which reiterates the fact that the strain induced by the use of a foreign substrate is very small in *a*-plane AlN. The *a*-plane homoepilayer has an emission intensity that is at least one order of magnitude higher and a much narrower emission linewidth compared to those of *a*-plane heteroepilayers, although no optimization processes for homoepilayer growth was carried out due to the limited supply of AlN bulk

substrates. The results reaffirm the higher crystalline and optical qualities of homoepilayers over heteroepilayers.

In summary, we have investigated the optical properties of AlN homoepilayers and heteroepilayers. Our results indicate that homoepilayers are nearly stress free and possess an identical band gap of about 6.099 (6.035) eV at 10 (300) K. The stress on *a*-plane AlN heteroepilayers grown on *r*-plane sapphires is very small. Due to the unique band structure of

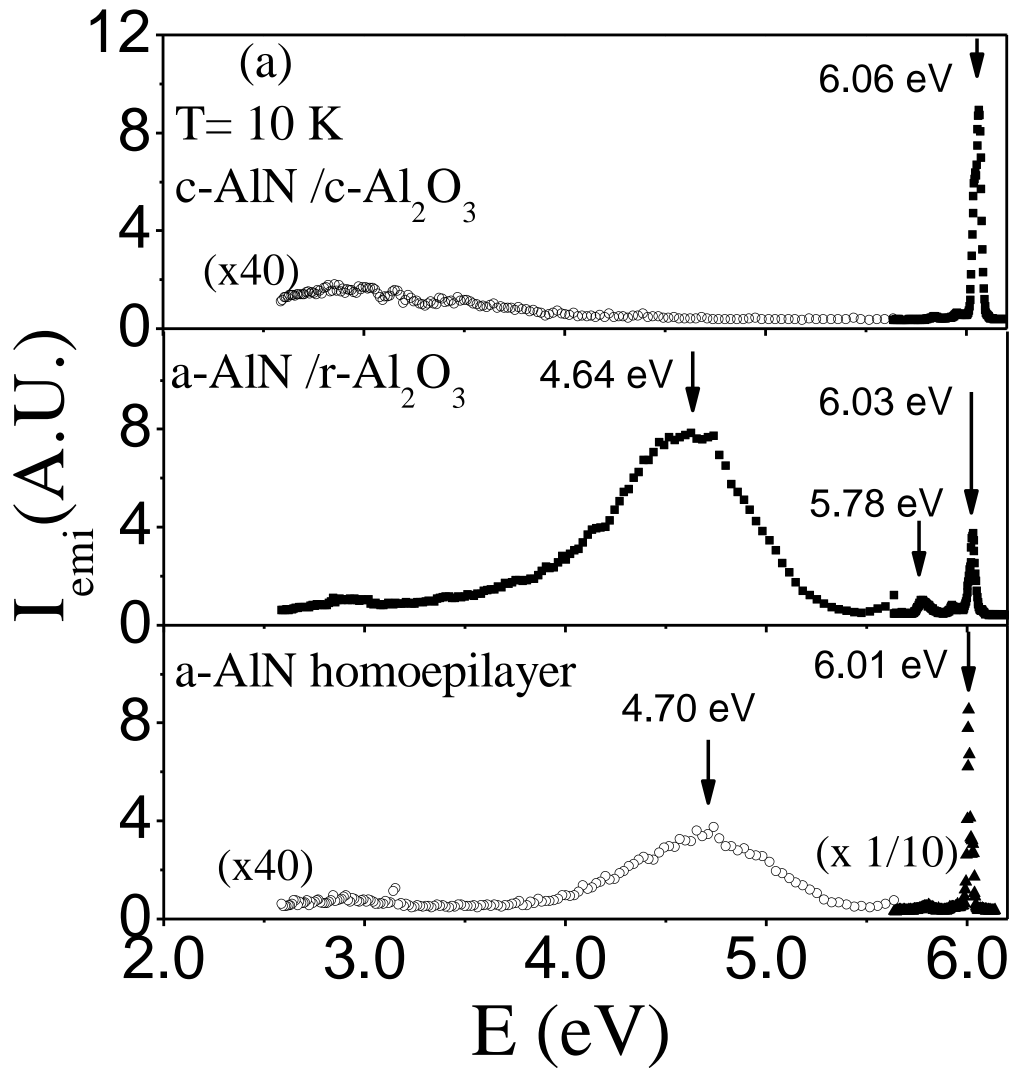

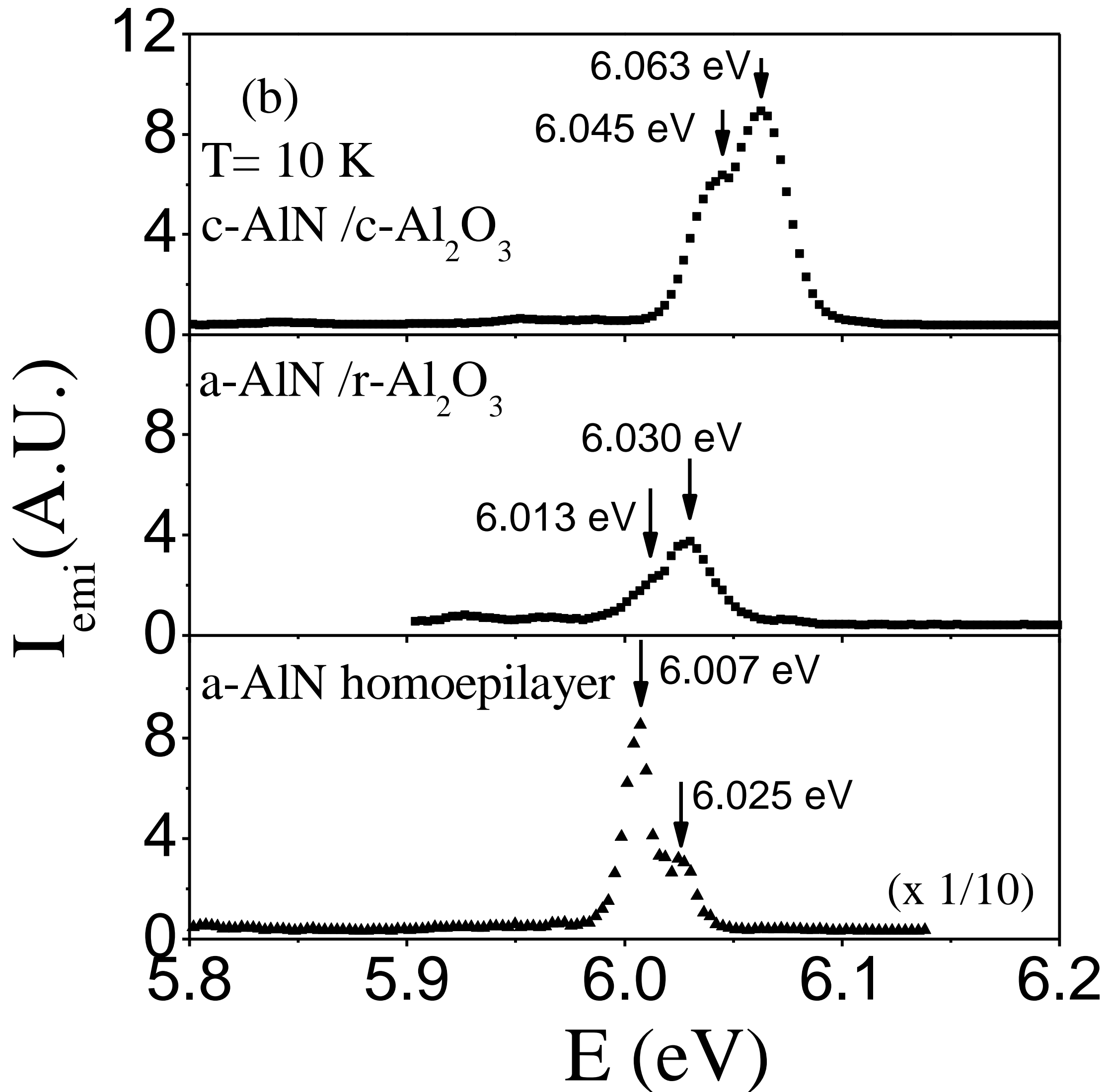

Fig. 3.6 Low temperature (10 K) PL spectra of c-AlN/c-Al_2O_3, a-AlN/r-Al_2O_3 and a-plane AlN homo-epilayer measured in a (a) wide spectral range from 2 to 6.2 eV and (b) narrow spectral range from 5.8 to 6.2 eV.

AlN, we believe that *a*-plane AlN homoepilayers have the potential to provide orders of magnitude improvement in the performance of new generation DUV photonic devices, especially surface emitting devices.

3.3 Beryllium acceptor in AlN

Light sources such as light emitting diodes and laser diodes, and detectors operating in ultraviolet (UV) and deep UV (DUV) spectral region are of technological importance for ultrahigh-density optical data storage/readout and high resolution photolithography in micro- and nanofabrication technologies by extending the optical diffraction limit. Environmental science would also benefit from such sources and sensors in detecting minute hazardous particles, sterilization, and air/water purification. With a wide and direct band gap of ~6.1 eV and complete solubility with GaN (band gap ~3.4 eV) in the entire alloy composition range, AlN has emerged as an important semiconducting material for the fabrication of chip scale integratable DUV light sources and detectors.

In the past, AlN was considered to be an excellent insulator. But in recent years, with the advances in thin film growth techniques, the optical quality of undoped AlN epilayers has been demonstrated to be comparable to that of GaN [18,65,86]. Optoelectronic DUV devices require conductive *p*- and *n*-type AlN and Al-rich AlGaN alloys. AlN epilayers with *n*-type conductivity with a reasonable free electron concentration (9.5×10^{16} to 7.4×10^{17} cm^{-3}) have been obtained by Si doping by several groups [87-89], but the situation is quite challenging for *p*-type doping. Mg is the most commonly used *p*-type dopant in nitrides. Our group has previously achieved *p*-type conduction at room temperature in Mg-doped $Al_xGa_{1-x}N$ for x up to 0.27 [90]. The resistivity of Mg-doped AlGaN increases with Al content and becomes extremely high in Mg-doped AlN (~1 Ω cm in GaN to >10^7 Ω cm in AlN at 300 K) due to increased energy level of Mg (~160 meV in GaN versus 510 meV in AlN) [47,90,91] along with lower formation energy of donor-like native defects that act as hole compensating centers [49]. We have also investigated Zn doping in AlN and experimentally confirmed that Zn is a deeper acceptor than Mg [68]. *P*-

type conduction in Mg-doped $Al_{0.70}Ga_{0.30}N$ and pure AlN was observable only at elevated temperatures (>700 K) [50,92]. Even though there are a few reports on active devices based on pure AlN [51,66,93], the attainment of AlN with a controllable and reproducible room temperature *p*-type conductivity is still far from reality and it is a subject of intense research interest in the nitride community.

With Mg doping limited by saturation, assuming a maximum attainable doping concentration of ~10^{20} cm^{-3}, a maximum achievable free hole concentration (p) at room temperature in AlN would only be ~10^{12} cm^{-3} [$p = N_A e^{-E_0/K_B T}$, where N_A is the doping concentration and E_0 (~0.51 eV) is the Mg energy level], which may be further reduced by compensation. A previous calculation using effective mass theory has predicted that Be occupying Al site (Be_{Al}) in AlN acts as an acceptor with an activation energy of 0.26–0.47 eV [94]. A more recent calculation also suggested a lower activation energy of Be_{Al} (~0.34 eV) than Mg_{Al} [95]. The smaller activation energy of Be in AlN has the potential to partly address the *p*-type doping issue by increasing the room temperature free hole concentration. To date, no experimental determination of the binding energy (BE) of Be acceptor in AlN has been reported. In this work, we report on the metal-organic chemical vapor deposition (MOCVD) growth of Be-doped AlN and probing Be acceptor BE in AlN by time-resolved photoluminescence (PL).

The 0.5 μm thick Be-doped AlN epilayers were grown by low pressure MOCVD on (0001) *c*-plane oriented AlN/sapphire templates. The growth temperature and pressure were 1150 °C and 60 torr, respectively. A DUV time-resolved PL system was employed to investigate the energetic position and recombination lifetime of the acceptor-bound exciton transition (I_1) in Be-doped AlN. The PL system consists of a frequency quadrupled 100 fs Ti:

sapphire laser with a 76 MHz repetition rate and excitation photon energy set around 6.30 eV. The PL signal was dispersed by a 1.3 m monochromator and detected by a streak camera [67].

In Fig. 3.7, we plot the continuous-wave PL spectra of Be-doped AlN epilayers measured at 10 K in (a) a broad spectral range from 2 to 6.2 eV and (b) a narrower spectral range from 5.8 to 6.2 eV. PL spectra of undoped and Mg-doped AlN are plotted together for comparison. Two band-edge peaks are well resolved in undoped AlN with virtually no impurity

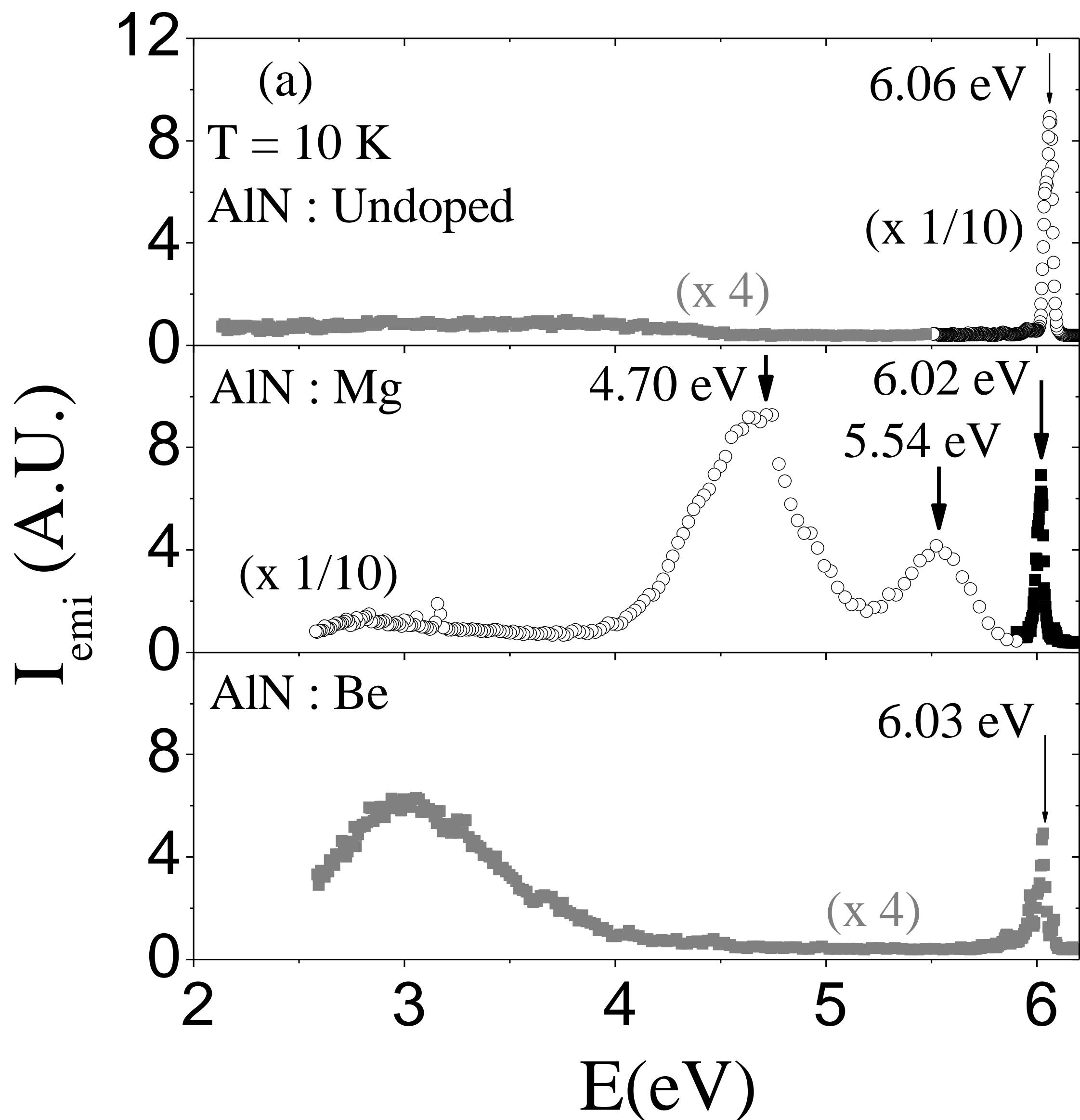

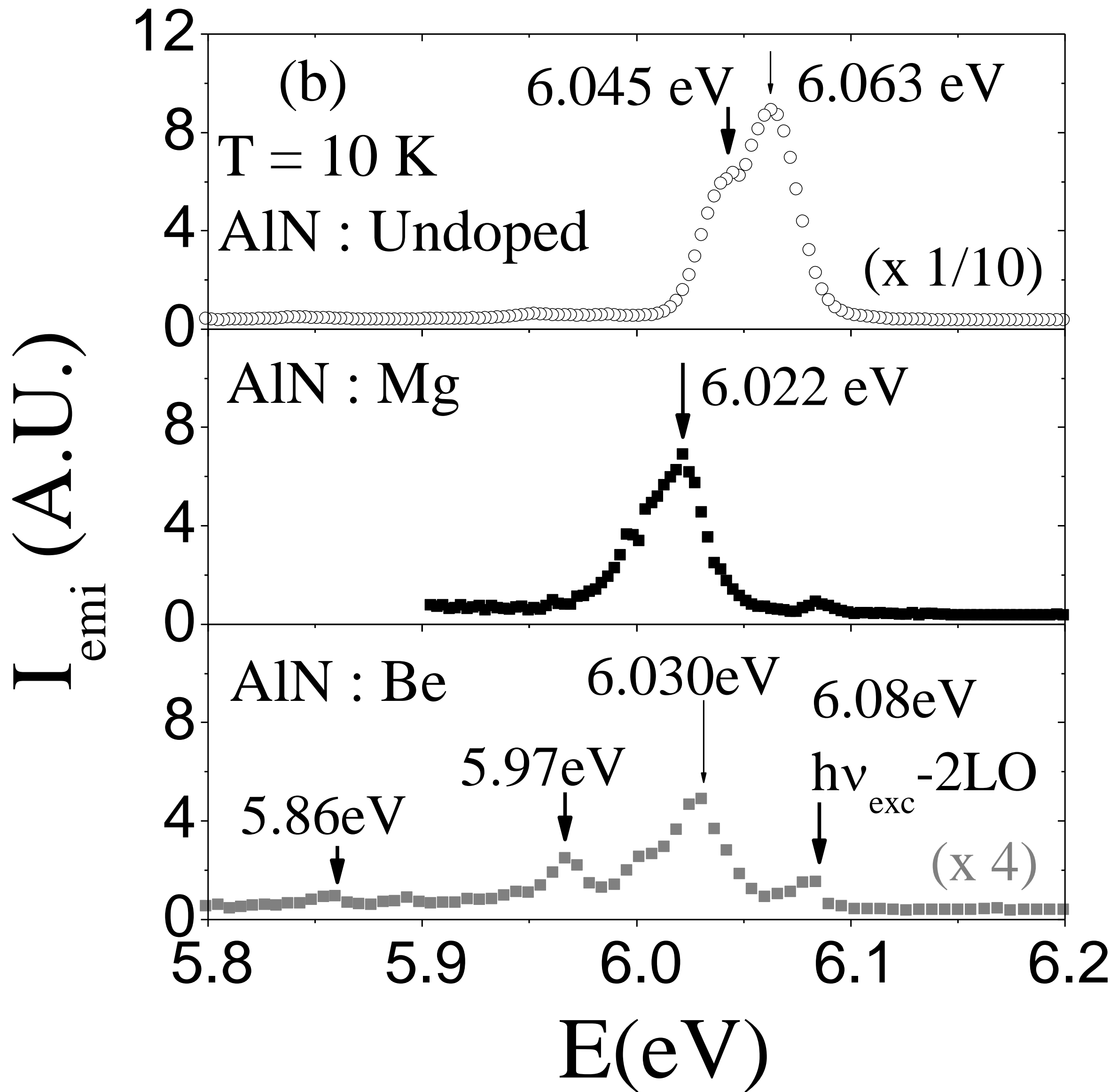

Fig. 3.7 Low temperature (10 K) PL spectra of undoped, Mg doped and Be doped AlN epilayers measured in (a) a wider spectral range from 2 to 6.2 eV and (b) narrower spectral range from 5.8 to 6.2 eV.

related emission lines. In undoped AlN, we attribute the dominant emission peak at 6.063 eV to the recombination of free exciton (FX) and the emission line at 6.045 eV (18 meV below the FX

peak) to the donor-bound exciton transition (the I_2 line). Energy difference (18 meV) between the two peaks provides the BE of the donor-bound exciton in AlN, which agrees well with a previous reported value [3].

In the near-band-edge PL spectra of Mg-doped AlN epilayers, FX transition disappears and a new emission line with a peak position at 6.022 eV is observed, which is attributed to the recombination of excitons bound to neutral Mg acceptors (A_0,X) or the I_1 line in Mg-doped AlN [96]. Weak emission lines at 6.08, 5.97, and 5.86 eV in Be-doped AlN are 2LO, 3LO, and 4 LO phonon replica of excitation laser (6.30 eV) with LO phonon energy of 110 meV in AlN. The emission peak at 6.030 eV in Be-doped AlN appears at a higher energy position (by 8 meV) than the I_1 transition in Mg-doped AlN. The temperature dependence of the 6.030 eV emission line follows that of the energy band gap. The spectral linewidth and shape are very similar to those of the I_1 transition in Mg-doped AlN. Therefore, we assign the emission line at a 6.030 eV peak in Be-doped AlN to the recombination of excitons bound to neutral Be impurities.

The energy difference between the FX peak position in undoped AlN and the I_1 line in Be-doped AlN gives the BE of the excitons bound to Be impurities to be 33 meV (=6.063–6.030 eV). According to Haynes' rule, the BE of the exciton-neutral impurity complex is about 10% of the impurity BE, neglecting the central cell correction [97]. The I_1 spectral peak position measurement thus implies that Be acceptor BE is about 0.33 eV, which agrees quite well with the calculated value of ~0.34 eV for the substitutional Be at the Al site [95]. In the case of Mg-doped AlN, the BE of the acceptor-bound exciton is about 41 meV (= 6.063–6.022 eV), which is very close to the previously reported values of 40 meV (Ref. 95) and 8 meV larger than that of the Be acceptor-bound exciton in AlN. Based on Haynes' rule, our results suggest that the Be acceptor level is about 80–150 meV shallower than that of the Mg in AlN.

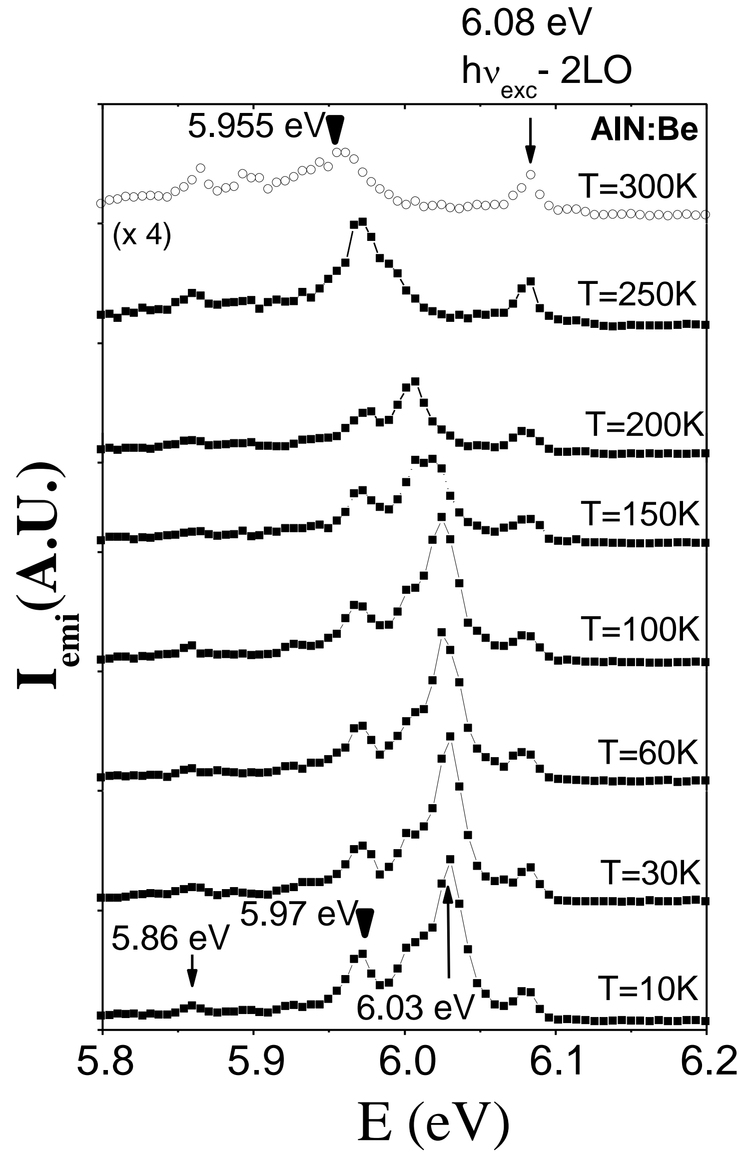

Fig. 3.8 Temperature dependence of the I_1 transition in Be doped AlN epilayers measured from 10 to 300 K.

The temperature dependence of the PL intensity of the I_1 transition on Be-doped AlN has been measured, which is shown in Fig. 3.8. The general trends of decrease in PL intensity and redshift of the emission peak position with temperature are evident. The decrease in

the I_1 intensity is due to the dissociation of acceptor-bound exciton into the neutral acceptor (A^0) and free-exciton (X) following $A^0X \rightarrow A^0 + X$. Fig. 3.9 shows the Arrhenius plot of the I_1 emission intensity and the solid line is the least squares fit of the data with the equation

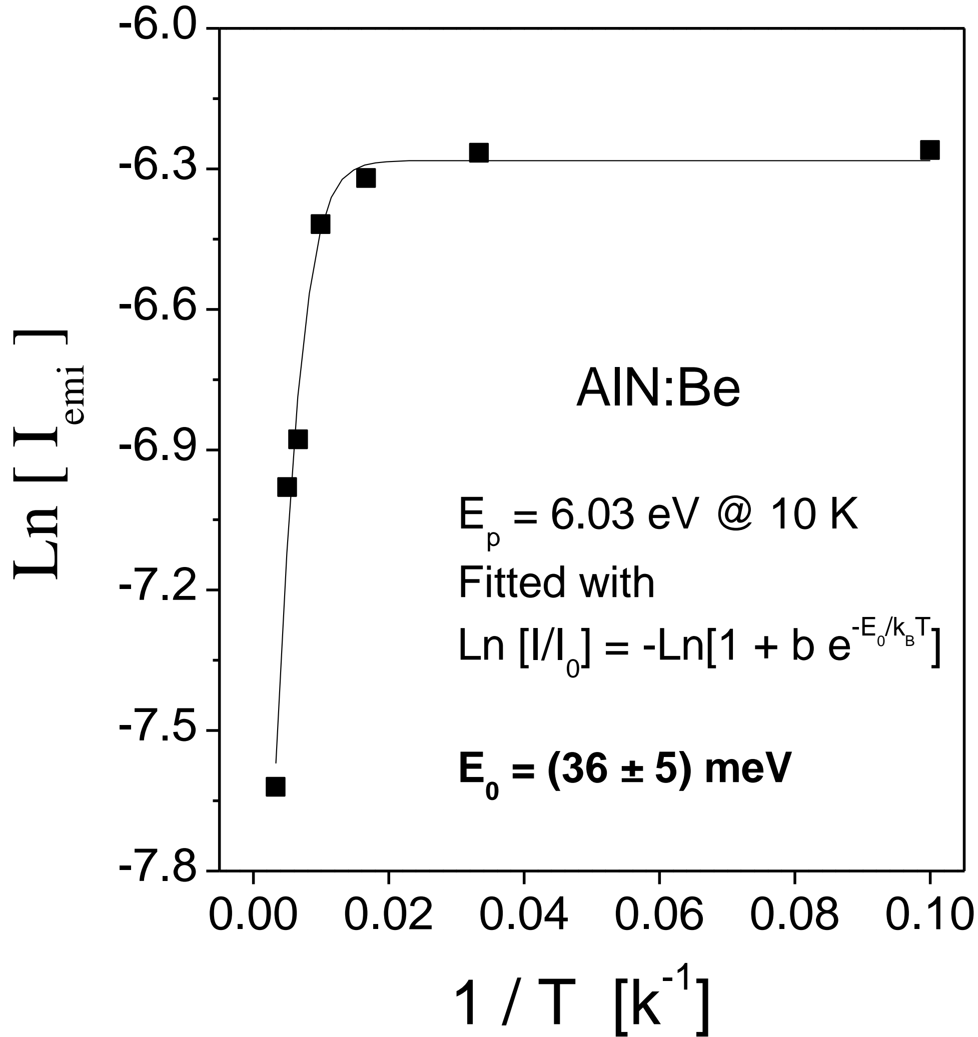

Fig. 3.9 The Arrhenius plot of the PL intensity [Ln (I_{emi}) vs 1/T] of the I_1 transition (6.03 eV at 10 K) for Be doped AlN epilayers. The solid line represents the least square fit of the data with Eq. (1).

3.2. The fitted value of E_0, the activation energy of the I_1 emission intensity, is around 36 meV, which measures the BE of the acceptor-bound exciton in Be-doped AlN and is in good agreement with a value of 33 meV obtained from the spectral peak measurement of Fig. 3.7.

Fig. 3.10 shows the temporal response of the I_1 transitions in Be- and Mg-doped AlN epilayers. The measured decay lifetimes of the I_1 transitions in Be- and Mg-doped AlN are 93 and 119 ps, respectively. The relation between the oscillator strength of the impurity-bound exciton (F) and the free exciton (F_{ex}) is expressed as [98,99]

$$F = (E_0/E_{bx})^{3/2} F_{ex}, \tag{3.4}$$

where E_{bx} is the BE of the impurity-bound exciton and E_0 is the BE of the free exciton. The ratio between the decay lifetimes of the I_1 transition in Be- and Mg-doped AlN can thus be obtained as

$$\frac{\tau_{I_1}(Be)}{\tau_{I_1}(Mg)} = \frac{F_{I_1}(Mg)}{F_{I_1}(Be)} = \left[\frac{E_{bx}(Be)}{E_{bx}(Mg)}\right]^{3/2}, \tag{3.5}$$

$[E_{bx}(\mathrm{Be})/E_{bx}(\mathrm{Mg})]^{3/2}$ lies within 0.72–0.85 and is in agreement with the ratio of (93 ps/119 ps) = 0.78 of the measured decay lifetimes. Time-resolved PL results are thus further corroborating our conclusion that the Be acceptor energy level in AlN is shallower than that of Mg.

In summary, Be-doped AlN epilayers were grown by MOCVD and their optical properties were investigated by time-resolved DUV PL. Be impurity related acceptor-bound exciton transition is observed at 6.03 eV with a BE of about 33 meV, which indicates that the Be level in AlN is about 80–150 meV shallower than Mg. Our additional experimental data from temperature dependent PL and decay lifetime measurements of the I_1 transition provided a

coherent picture to support the fact that the Be energy level is shallower than that of Mg in AlN. As our Be-doped AlN layers are highly resistive at this point, direct transition from free electron

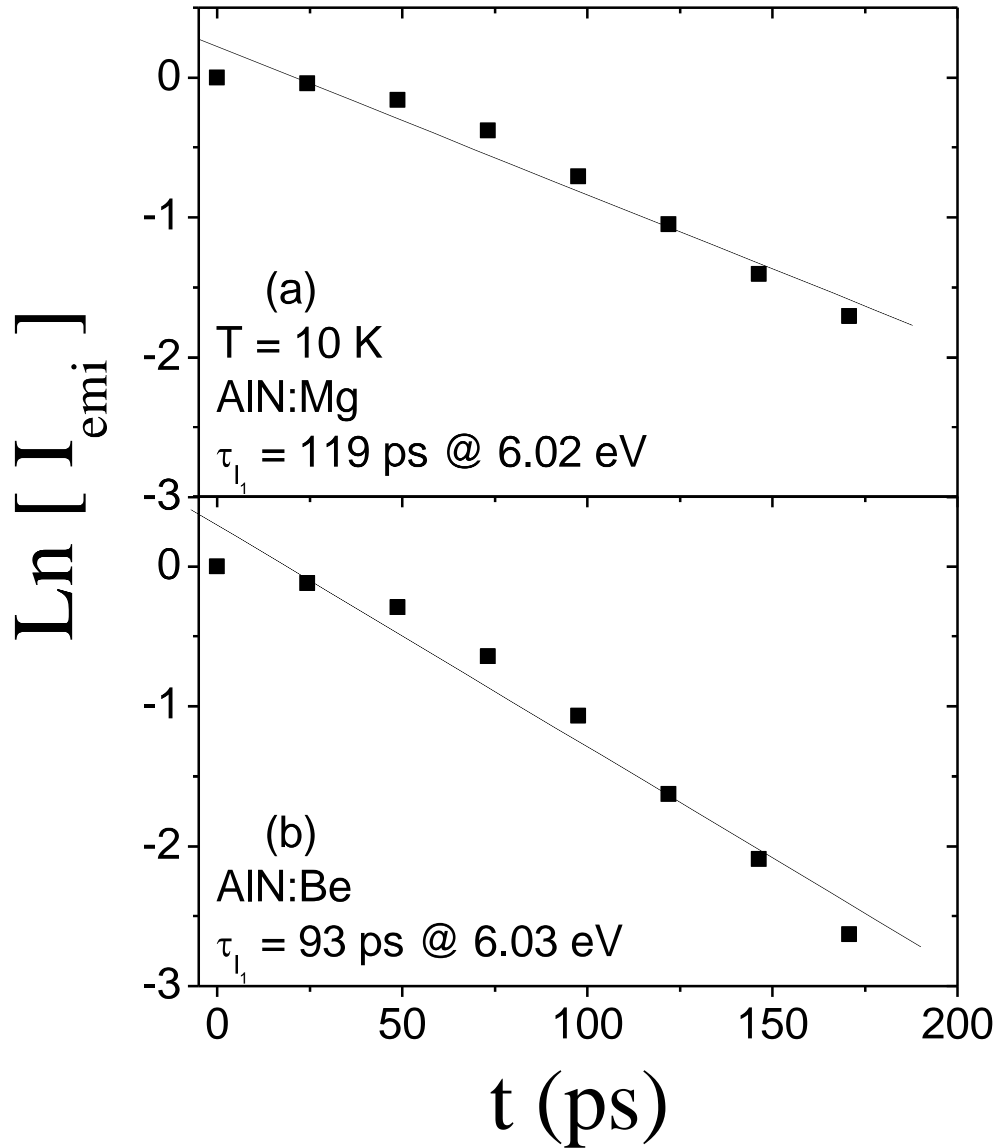

Fig. 3.10 Temporal responses of the I_1 transition in (a) Mg and (b) Be doped AlN epilayer measured at 10 K. Measured decay lifetimes were 119 and 93 ps for Mg and Be doped AlN epilayers, respectively.

to neutral Be acceptor could not be observed, which would have provided a direct measure of the energy level of Be_{Al} acceptor in AlN. Much more work is required to obtain Be-doped AlN epilayers that exhibit a higher *p*-type conductivity than Mg-doped layers.

3.4 Probing exciton-phonon interaction in AlN by photoluminescence

AlN has attracted tremendous interest as a semiconductor material for deep UV (DUV) optoelectronic device applications because of its ultrahigh direct bandgap (~6.1 eV). Recent advances in epitaxial growth techniques have made it possible to grow high quality AlN epilayers on different substrates [3,18,51,100,101]. A few active DUV devices based on pure AlN have also been demonstrated, including light emitting diodes with an emission wavelength of 210 nm (Ref. 66) and metal-semiconductor-metal and Schottky barrier photodetectors for DUV and extreme UV device applications [65,93,102]. The availability of device quality AlN epilayers also opens up new opportunities for probing fundamental parameters in AlN to a degree previously unattainable. Due to the ionic nature of III-nitrides, Frohlich interaction, which is the Coulomb interaction between electrons (holes) and longitudinal electric field produced by the zone-center longitudinal optical (LO) phonons, is stronger compared to deformation-potential or piezoelectric interaction in these materials. The coupling of carriers with LO phonons strongly influences the optical and transport properties of III-nitrides [103].

The A_1 (LO) phonon in AlN has an energy of about 110 meV as determined by the Raman spectroscopy measurement [104]. There have been previous reports on carrier-phonon interaction in GaN [105,106], InGaN/GaN, and GaN/AlGaN quantum wells [107]. To the best of our knowledge, no experimental work has been reported on the strength of such interactions in AlN due to the lack of high quality materials and proper characterization tools to match the ultrahigh band gap of AlN in the past. In this letter, we report on the observation of phonon replicas associated with the free exciton recombination and polarization resolved PL measurement of the exciton-phonon coupling strength (S) in wurtzite AlN.

AlN homo- and hetero-epilayers with thicknesses of about 0.5 μm were synthesized by MOCVD on both (0001) sapphire (Al_2O_3) and AlN bulk crystal substrates (supplied by Crystal IS, Inc.). A thin layer of AlN buffer was deposited at 550 °C prior to the growth of the heteroepilayer. Trimethyl aluminum and ammonia (NH_3) were used as Al and nitrogen sources. AlN epilayers were grown at 1200 °C with a V/III ratio of around 150. PL signals were collected in two different configurations of the polarization of emitted light, e.g., the electrical field of the PL emission is directed either parallel ($\vec{E} \parallel \vec{c}$) or perpendicular ($\vec{E} \perp \vec{c}$) to the wurtzite *c*-axis. A frequency quadrupled Ti-sapphire laser with a repetition rate of 76 MHz and 100 fs pulse width operating at 197 nm was focused onto the sample surface through a microscope objective. The collected PL signal was then dispersed by a 1.3 m monochromator and detected by a microchannel-plate photomultiplier tube.

Low temperature (10 K) PL spectra of an AlN epilayer grown on *c*-plane sapphire are shown in Fig. 3.11 for both $\vec{E} \parallel \vec{c}$ and $\vec{E} \perp \vec{c}$ configurations. The PL spectrum collected in the $\vec{E} \parallel \vec{c}$ configuration shown in Fig. 3.11 exhibits the main free exciton emission line at 6.06 eV (Ref. 108) and two weaker peaks at 5.95 and 5.84 eV. The energy separation between the successive emission lines is 110 meV, which corresponds to the value of the LO phonon energy in AlN [104]. We thus assign the two lower energy peaks to the $n = 1$ and $n = 2$ phonon replicas of the main exciton transition line ($n = 0$) in order by decreasing energy. We observed a similar trend of phonon assisted excitonic emission in the $\vec{E} \perp \vec{c}$ configuration, as illustrated in Fig. 3.11(b). In the latter case, though the intensity of the main exciton emission line ($n = 0$) is much lower than that in the $\vec{E} \parallel \vec{c}$ configuration due to the unique fundamental band structure of AlN [64], the relative intensities of phonon assisted emission lines are much higher and LO phonon replicas up to $n = 3$ have been resolved. The appearance of the phonon replica lines is a

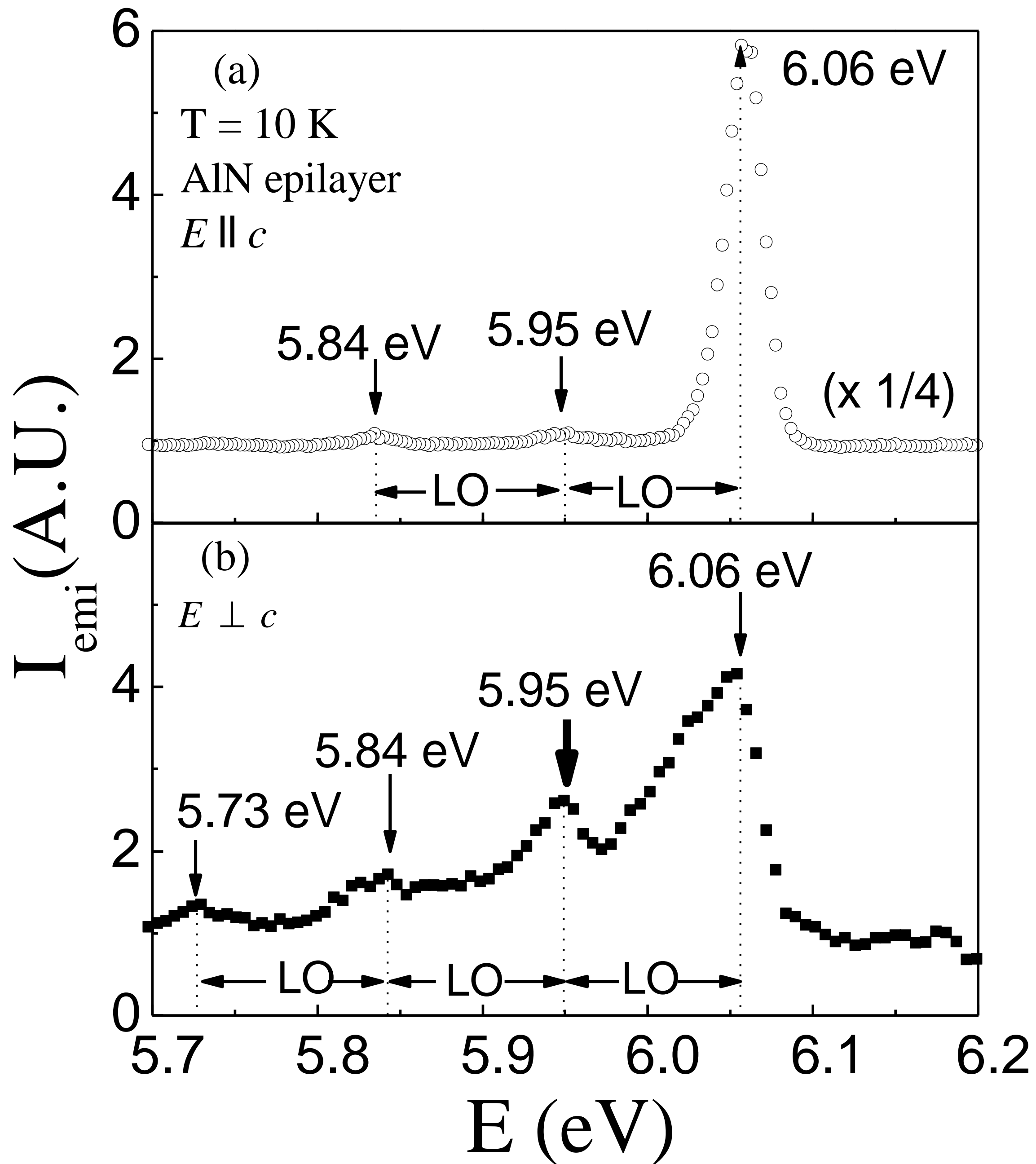

Fig. 3.11 Low temperature (10 K) PL spectra of an AlN hetero-epilayer collected with the polarization of emitted light (a) parallel ($\vec{E} \parallel \vec{c}$) and (b) perpendicular ($\vec{E} \perp \vec{c}$) to the crystallographic c-axis.

clear indicator of a strong carrier-phonon interaction in AlN. It is also noted that the observed phonon lines have an energy separation corresponding to the A_1 (LO) phonon in AlN (110 meV) and no other phonon replica lines have been observed. This is consistent with the fact that the electron-LO phonon Frohlich interaction is the strongest in AlN [103].

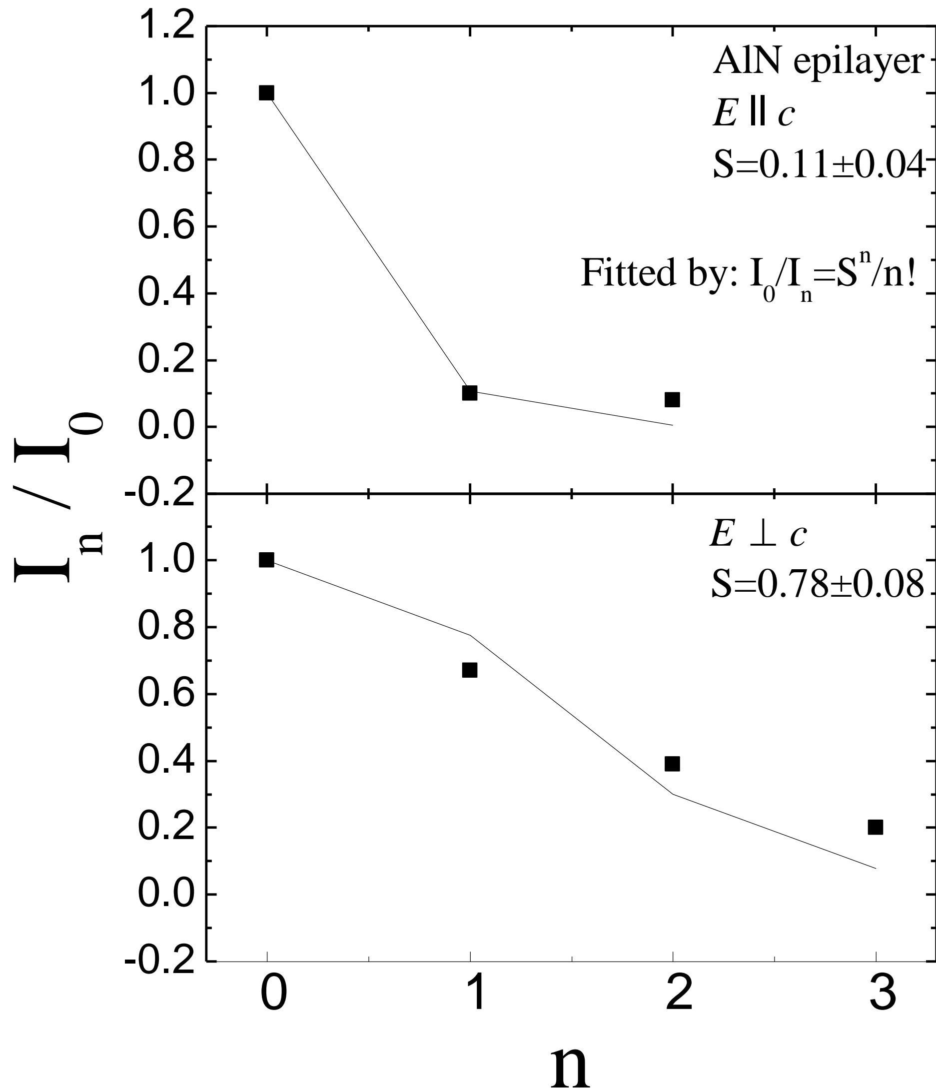

Fig. 3.12 Normalized PL intensities of nth order phonon replicas with respect to the zero phonon line measured in an AlN hetero-epilayer in two different polarization configurations.

The distribution of emission intensities among the main peak (n = 0) and the phonon replicas (n = 1 and n = 2) depends on the exciton-phonon coupling strength, which is expressed by Huang–Rhys factor, S, within the Franck–Condon approximation. At low temperatures, the emission intensity of the nth phonon replica (I_n) and the main emission line (I_0) are related by [109-111]

$$I_n = I_0 (S^n / n!) , \tag{3.6}$$

where n = 0,1,2,3,…, which represent the number of LO phonons involved.

Fig. 3.12 plots I_n/I_0 for both $\vec{E} \parallel \vec{c}$ and $\vec{E} \perp \vec{c}$ configurations. It is interesting to note that the coupling constant, S, in AlN varies greatly between the two polarization configurations of emitted light. The S-parameter obtained by fitting the observed I_n/I_0 with Eq. (1) is $S^{\perp} = 0.78$ in the $\vec{E} \perp \vec{c}$ configuration, which is much higher than the value of $S^{\parallel} = 0.11$ measured in $\vec{E} \parallel \vec{c}$ configuration.

For the free exciton in materials with wurtzite structures, the exciton-phonon coupling constant may be expressed in terms of the fundamental quantities including optical and static dielectric constants (k_o,k_s), the hole to electron effective mass ratio ($\alpha = m_h/m_e$), Bohr radii of electron and hole (a_e,a_h), and LO phonon energy $\hbar\omega_{\mathrm{LO}}$ (= 110 meV) as follows [112]:

$$S = \frac{5}{16}\frac{e^2}{\hbar\omega_{LO}}\left(\frac{1}{\kappa_\infty} - \frac{1}{\kappa_0}\right)\left[\frac{1}{a_h} + \frac{1}{a_e} - \frac{16(\alpha^2 + 3\alpha + 1)}{5a_e(\alpha+1)^3}\right], \tag{3.7}$$

It can be seen that between the two polarization configurations in AlN, the difference in the coupling parameter (S) predominantly originates from the value of α since a_h and a_e are also related with α through the relationship of $a_{h(e)} = a_{ex}/(1+m_{h(e)}/m_{e(h)})$, where a_{ex}[= $(1/m_h+1/m_e)m_0k_sa_0$] (Ref. 113) is the ground state exciton Bohr radius. More specifically, the value of α is about 42 in the $\vec{E} \perp \vec{c}$ configuration and is about 11 in the $\vec{E} \parallel \vec{c}$ configuration [62]. We have attempted to utilize Eq. (2) to estimate the hole effective mass anisotropy from the measured S values of $\vec{E} \perp \vec{c}$ and $\vec{E} \parallel \vec{c}$ configurations. The deduced value of $m_h^{\perp}/m_h^{\parallel}$ from the measured $S^{\perp}$ and $S^{\parallel}$ is about a factor of 2 larger than the calculated value, which is about 3.2 [62]. We thus believe that Eq. (2) is able to provide a qualitative explanation to the measured S values. However, it has to be cautioned to use it to explain experimental results quantitatively.

The measured S-parameters in AlN in both polarization configurations are much larger than a previously reported value of about 0.007 in GaN epilayers in which the PL emission is polarized predominantly in the $\vec{E} \perp \vec{c}$ configuration [114]. In addition to possible differences in material qualities, several factors may also account for this enhanced coupling in AlN over GaN. These include (1) the much larger value of α (~42 in AlN in the $\vec{E} \perp \vec{c}$ configuration versus ~8.9 in GaN in both polarization configurations) [113], (2) smaller exciton Bohr radii (~12 Å in AlN versus ~27 Å in GaN due to the differences in the effective masses and dielectric constants) [115,116], and (3) stronger ionic bonding between Al–N over Ga–N.

A comparison between heteroepilayers and homoepilayers has also been carried out and the results are shown in Fig. 3.13. In the AlN homoepilayer, emission lines at 6.03, 5.92, and 5.81 eV are due to the recombination of the free exciton and its 1LO and 2LO phonon replica, while the dominant emission line at 6.01 eV is associated with the donor-bound exciton (I_2)

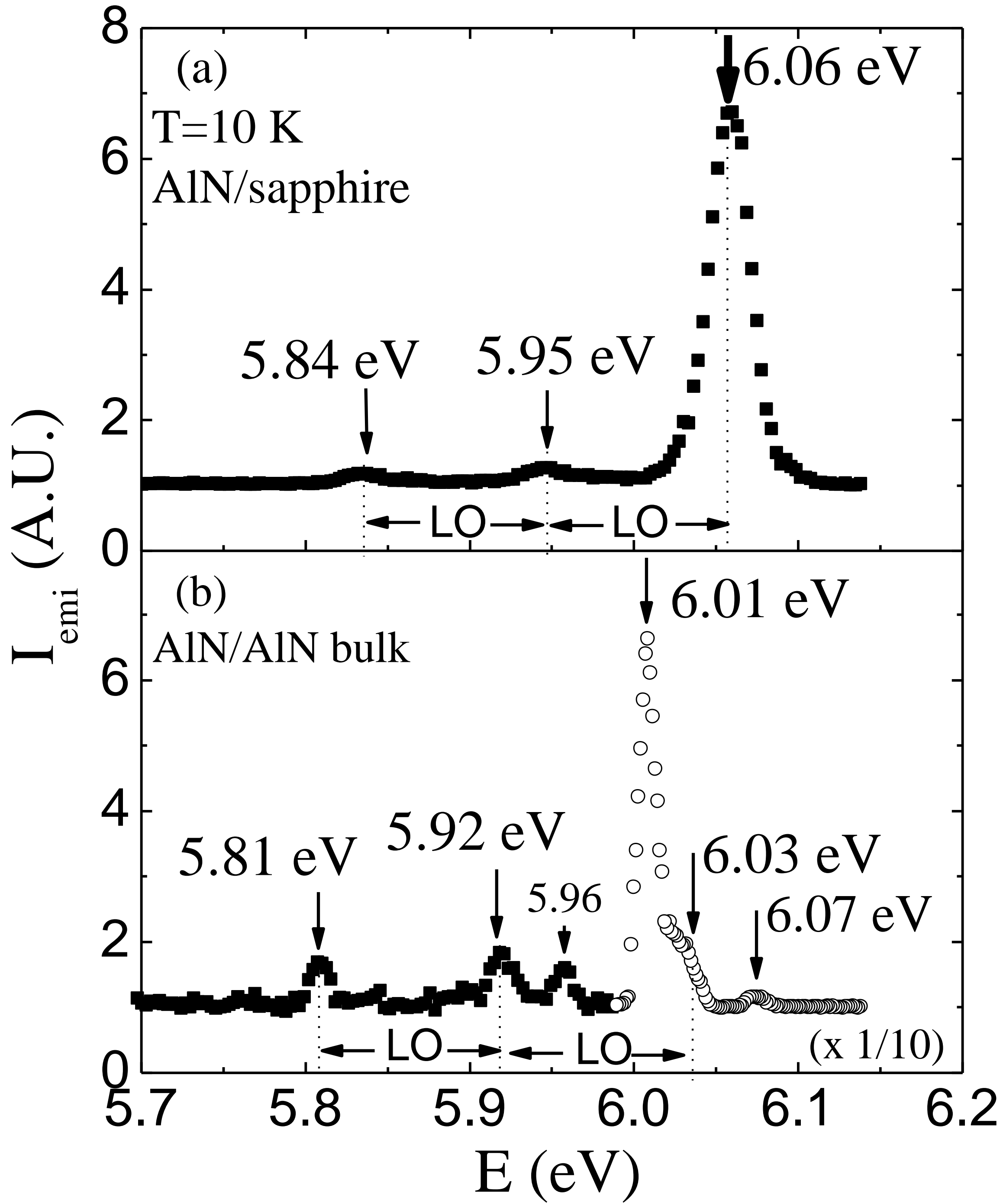

Fig. 3.13 Low temperature (10 K) PL spectra of (a) an AlN hetero-epilayer grown on sapphire and (b) an AlN homo-epilayer grown on bulk AlN substrate.

[117]. The exciton-phonon coupling constant is found to be slightly larger in heteroepilayers (S = 0.11 for heteroepilayer versus 0.09 for homoepilayer). A previous study has indicated that the emission intensities of phonon replica lines in GaN are lower in epilayers containing higher density of impurities [118]. Due to the possible diffusion of residual impurities in the AlN bulk substrate to the epilayer; our homoepilayers also contain higher density of unintentional donors than the heteroepilayers, as corroborated by the fact that the I_2 emission is dominant in homoepilayers [Fig. 3.13(b)]. In materials with high impurity concentrations, the scattering of exciton-polariton may be enhanced by impurity or related defects. Such scattering may assist in momentum transfer, and hence recombination becomes possible without the participation of phonons, which reduces the number of phonons involved, therefore weakening the coupling. Reduced efficiency of phonon assisted exciton emissions due to the enhanced scattering by defects has also been observed in p-type GaN [119]. Moreover, a previous observation of strong LO phonon replica emission lines relative to the zero-phonon line in Ga-face GaN epilayers (lower defect density) and almost no phonon replica in N-face GaN (higher defect density) is consistent with this argument because different polarities affect the growth modes and therefore the incorporation of defects [120].

In summary, exciton-phonon interactions in AlN have been investigated and it has been found that the coupling constant in AlN depends on the polarization configuration, and are 0.78 and 0.11 for the $\vec{E} \perp \vec{c}$ and $\vec{E} \parallel \vec{c}$ configuration, respectively. Moreover, the coupling constant is larger in AlN than in GaN. The larger hole to electron effective mass ratio in AlN, especially in the $\vec{E} \perp \vec{c}$ polarization configuration, is one of the predominant factors that accounts for the observed strong exciton-LO phonon coupling strength in AlN. The strong carrier-phonon

interaction in AlN may be exploited to maximize the benefits of phonon-assisted transitions in AlN based optoelectronic devices.

3.5 Origin of 2.78 eV PL emission and yellow coloration in bulk AlN

Free-standing, native nitride substrates with low dislocation densities and high crystalline quality are highly desirable for the epitaxial growth of next generation III-nitride devices such as short-wavelength light emitting diodes, laser diodes, solar blind ultraviolet (UV) detectors, surface acoustic wave devices, and high frequency microwave devices. In particular, the availability of bulk AlN crystals as a native substrate for III-nitride epitaxial growth will help to achieve practical deep UV (DUV) optoelectronic device structures by reducing dislocation density. Currently, several groups are developing various techniques for the growth of bulk AlN crystals [81,117,121-126]. Recent reports of homoepitaxial layer growth and device fabrication using bulk AlN substrates have already demonstrated potential applications [117,125,126].

Despite recent progress made in nitride epilayers and devices on AlN substrates, critical issues remain. For DUV applications, bulk AlN substrates should be transparent from the visible to DUV region. However, all sizeable bulk AlN substrates exhibit a yellow or dark amber color. A correlation between the yellow coloration of bulk AlN and a broad absorption band centered around 2.86 eV was previously reported [127]. Samples with relatively low oxygen contamination have an absorption band starting around 2.0 eV with a maximum at around 2.86 eV. However, the yellow coloration completely disappears in transparent AlN containing high levels of oxygen contamination ($\sim10^{19}$–10^{20} cm^{-3}). The disappearance of the yellow coloration was accompanied by a reduced absorption band centered at 2.86 eV. More recently, a similar broad absorption centered around 2.8 eV was reported in bulk AlN crystals with oxygen levels $\sim1\times10^{19}$ cm^{-3}, again with the absorption being more prominent in samples containing fewer oxygen impurities [128]. Thus, the yellow appearance of bulk AlN is widely believed to be

related to a broad absorption band centered around 2.86 eV. However, the physical origin of this absorption band has not been understood.

In this work, we studied the origin of the yellow appearance in AlN. Samples studied included c-AlN epilayers grown on sapphire by MOCVD, polycrystalline c-textured AlN grown by physical vapor transport, and bulk m-AlN single crystals produced by sublimation crystal growth using polycrystalline AlN wafers as seeds [117]. The epilayer, polycrystalline, and bulk AlN samples appear in transparent, light yellow, and amber colors under room light. These samples were determined to contain about 1.5×10^{17}, 1.0×10^{18}, and 2×10^{18} cm^{-3} of oxygen impurities, respectively, via SIMS measurements. Photoluminescence (PL) properties were investigated by employing our specially designed DUV laser spectroscopy system, which consists of a frequency quadrupled Ti-sapphire laser with a 76 MHz repetition rate. The excitation wavelength was set at 197 nm (6.31 eV) [67].

In Fig. 3.14(a), we compare the 300 K PL spectra of c-AlN epilayers, polycrystalline c-AlN, and bulk m-AlN with an above band-gap excitation. The AlN epilayer and polycrystalline AlN exhibit dominant free exciton (FX) emission peaks at 5.98 and 5.96 eV, respectively [92,100,117]. However, the FX transition at 5.95 eV and broad emission lines at 4.0 and 2.76 eV have comparable emission intensities in bulk m-AlN. The impurity band around 4.0 eV was previously identified as a donor-acceptor-pair type transition involving a shallow donor and an aluminum vacancy (V_{Al}) complex with 2/1 negative charges, either $(V_{Al}–O_N)^{2-/1-}$ or $(V_{Al}–Si_{Al})^{2-/1-}$ [44]. Fig. 3.14(b) compares the 10 K PL spectra of the same set of samples, which shows an obvious blue shift of the FX line to 6.06 (6.04) eV in the AlN epilayer sample (polycrystalline AlN). The 10 K spectra of all three samples display visible features at about 4.32 eV. The impurity transition at 2.76 eV is more prominent in bulk AlN at 10 K. Here, we will

concentrate our efforts to exploring the mechanism of the 2.76 eV emission line in AlN and understanding why bulk AlN substrates come with an undesirable yellow color.

In Fig. 3.15, we compare low temperature (10 K) PL spectra of all three samples with (a) above band gap excitation with a 197 nm (6.30 eV) laser line and (b) below band gap excitation with a 262 nm (4.739 eV) laser line. For below band gap excitation, the emission line at 4.32 eV is completely disappeared with the concomitant appearance of narrower and stronger emission

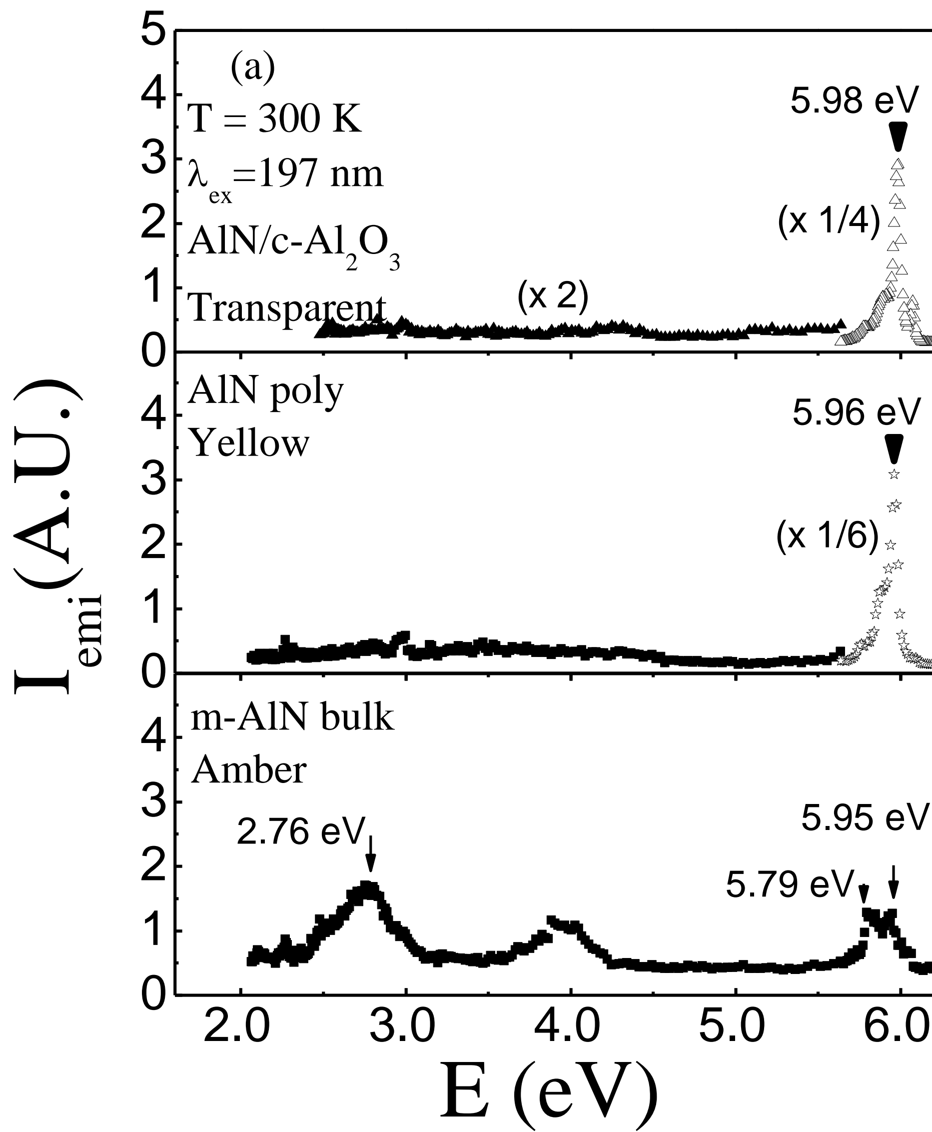

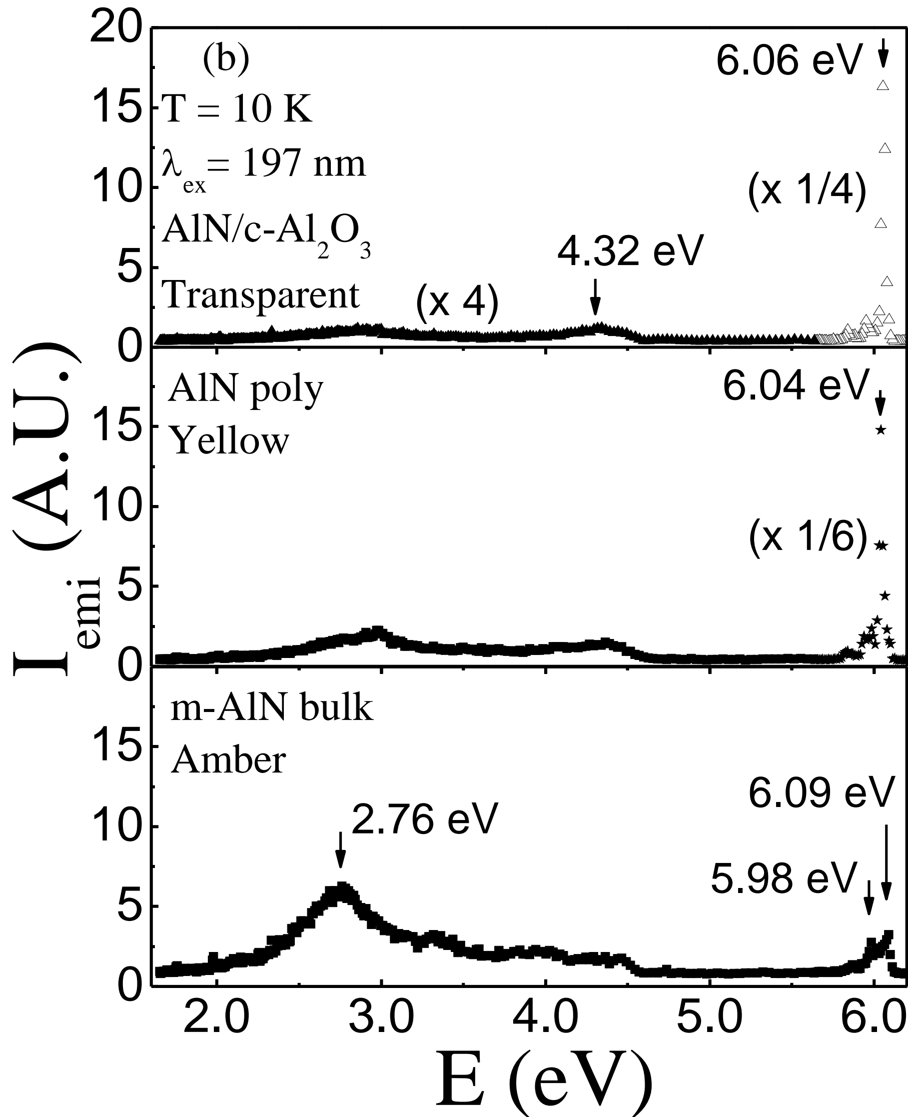

Fig. 3.14 (a) Room temperature (300 K) and (b) low temperature (10 K) PL spectra of AlN hetero-epilayer, polycrystalline AlN, and AlN bulk single crystal under above band-gap excitation scheme with 197 nm laser.

lines related to $(V_{Al}–O_N)^{2−/1−}$ or $(V_{Al}–Si_{Al})^{2−/1−}$ at 3.95 eV in all three samples. The emission line at 2.76 eV in the bulk m-plane sample is blue shifted to 2.78 eV with enhanced intensity and

narrowed spectral linewidth. Interestingly, the transparent AlN epilayer shows the lowest (sometimes negligible) emission at 2.78 eV, while the amber colored m-plane bulk AlN shows a remarkably strong emission at this energy. This indicates a stronger PL emission at 2.78 eV from more yellowish samples, which contain higher concentrations of oxygen impurities.

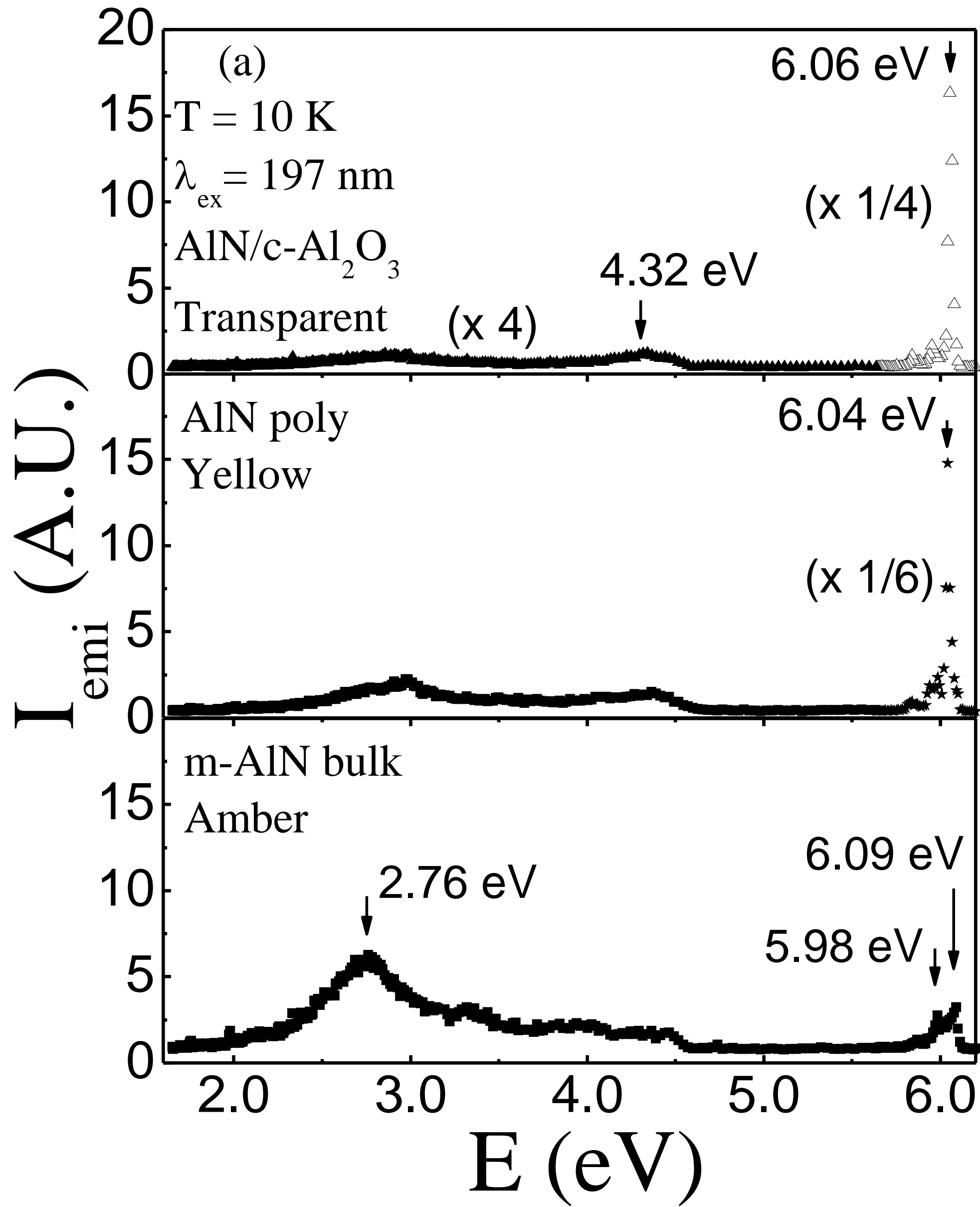

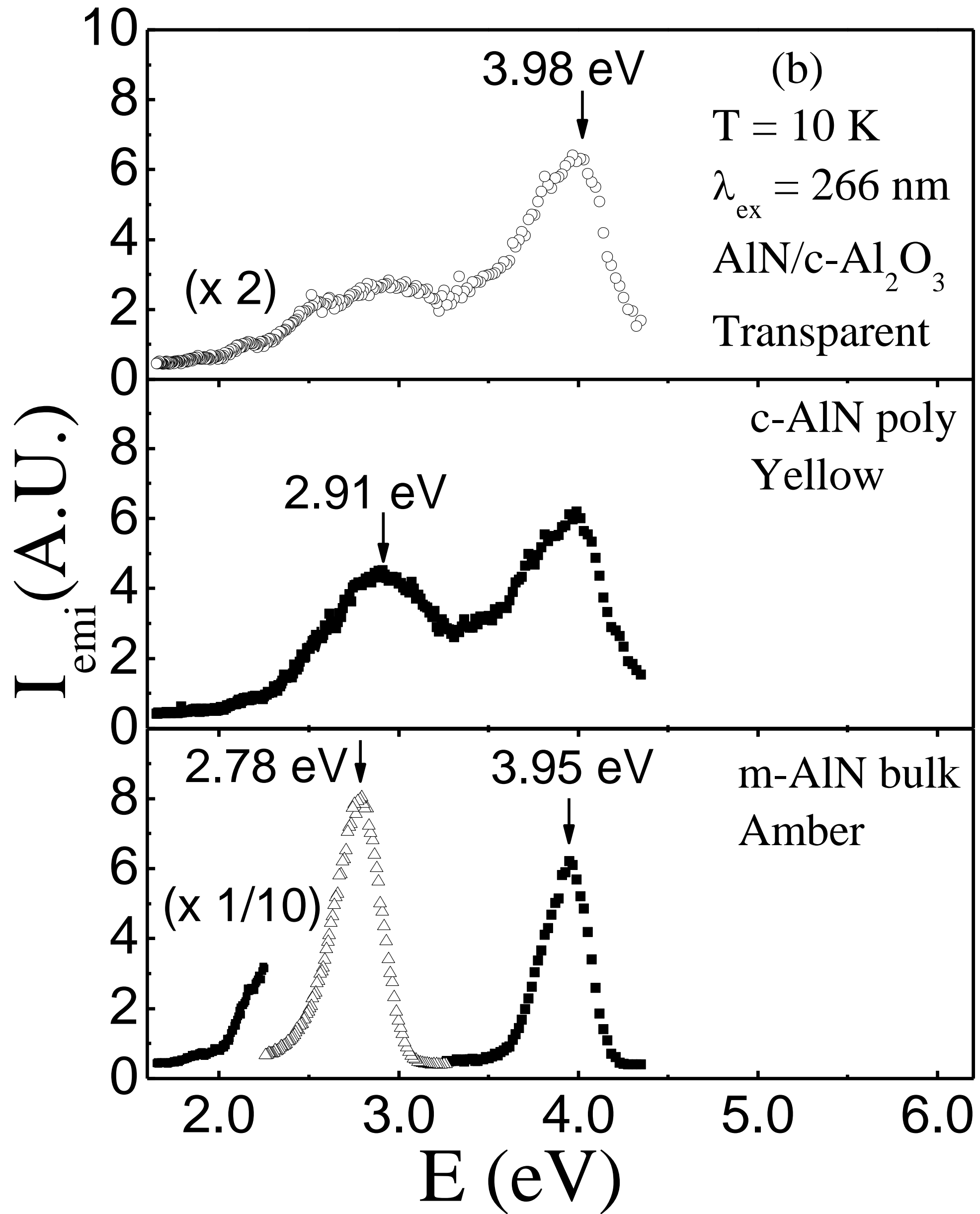

Fig. 3.15 Low temperature (10 K) PL spectra of AlN hetero-epilayer, polycrystalline AlN, and AlN bulk single crystal under: (a) above (197 nm) and (b) below (262 nm) band gap excitation.

The temperature dependence of the below band gap excitation PL spectra in the bulk m-AlN (measured around 2.78 eV) is shown in Fig. 3.16(a). The emission line is quite broad and

peak position does not change with temperature. The Arrhenius plot for the PL intensity of the 2.78 eV emission line from 10 to 400 K is shown in Fig. 3.16(b). The solid line is the least-squares fit of the experimental data with equation3.2 [129]. $I(T)$ and $I(0)$ are the PL intensities at temperature T and 0 K, a is a constant, and E_0 is the activation energy of PL intensity. We obtained thermal activation energy (E_0) of about 78 meV from the fitting. The physical meaning of this activation energy is not clear at this point.

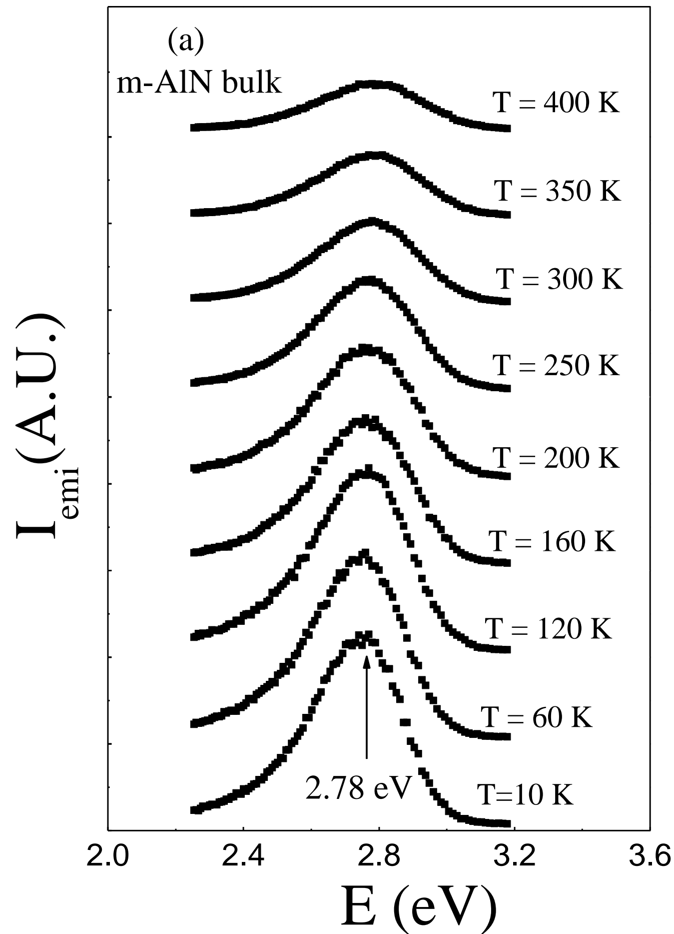

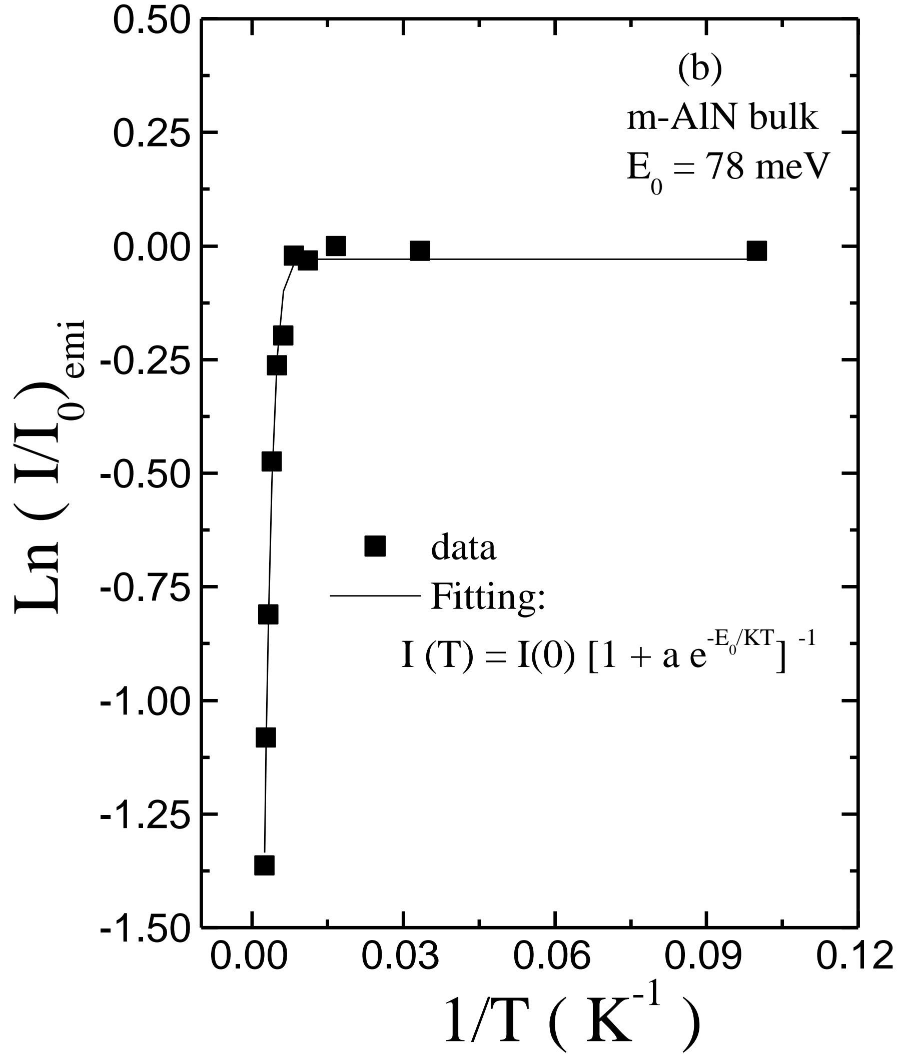

Fig. 3.16 (a) Temperature dependent PL spectra of m-AlN bulk around 2.78 eV with 262 nm excitation from 10 to 400 K. (b) The Arrhenius plot of the PL intensity of 2.78 eV emission line in m-AlN bulk.

In order to understand the mechanism of the 2.78 eV emission line in AlN, we have measured the excitation intensity (I_{exc}) dependence of this emission line, which is shown in Fig. 3.17(a). Blueshift of the peak position with an increase in I_{exc}, which is typical of donor-

acceptor-pair (DAP) type transition, was not observed here, suggesting that the 2.78 eV emission line is not a DAP type transition. Based on the energy positions we already know for V_N, V_{Al}, and V_{Al}-related complexes [44,45], the involvement of a conduction band or shallow donor is unlikely. The most plausible explanation that supports the PL spectral peak position data and the I_{exc}-dependence of PL intensity is a transition from the isolated aluminum vacancy $(V_{Al})^{3-/2-}$ to the valence band. $(V_{Al})^{3-/2-}$ is a deep center with two different charge states, triply negative charged V_{Al}^{3-}, and doubly negative charged V_{Al}^{2-}. This deep center changes its charge state from one to another by absorption (V_{Al}^{2-} to V_{Al}^{3-}) or emission (V_{Al}^{3-} to V_{Al}^{2-}) and readjusts its energy with an inward or outward relaxation of the neighboring atoms [41].

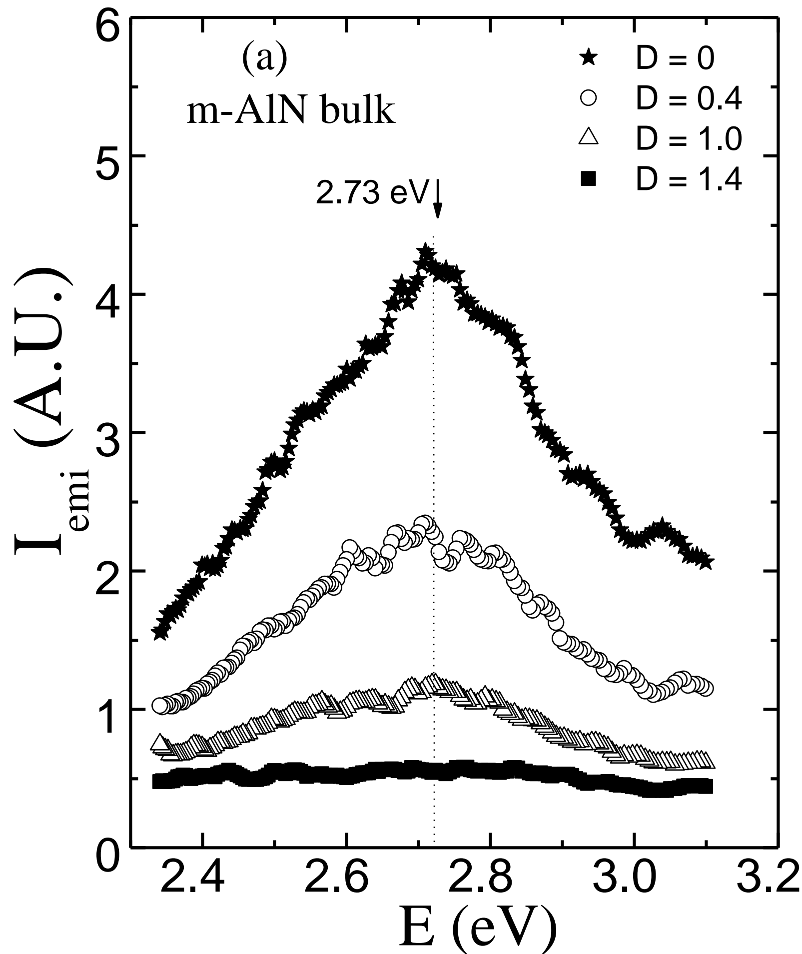

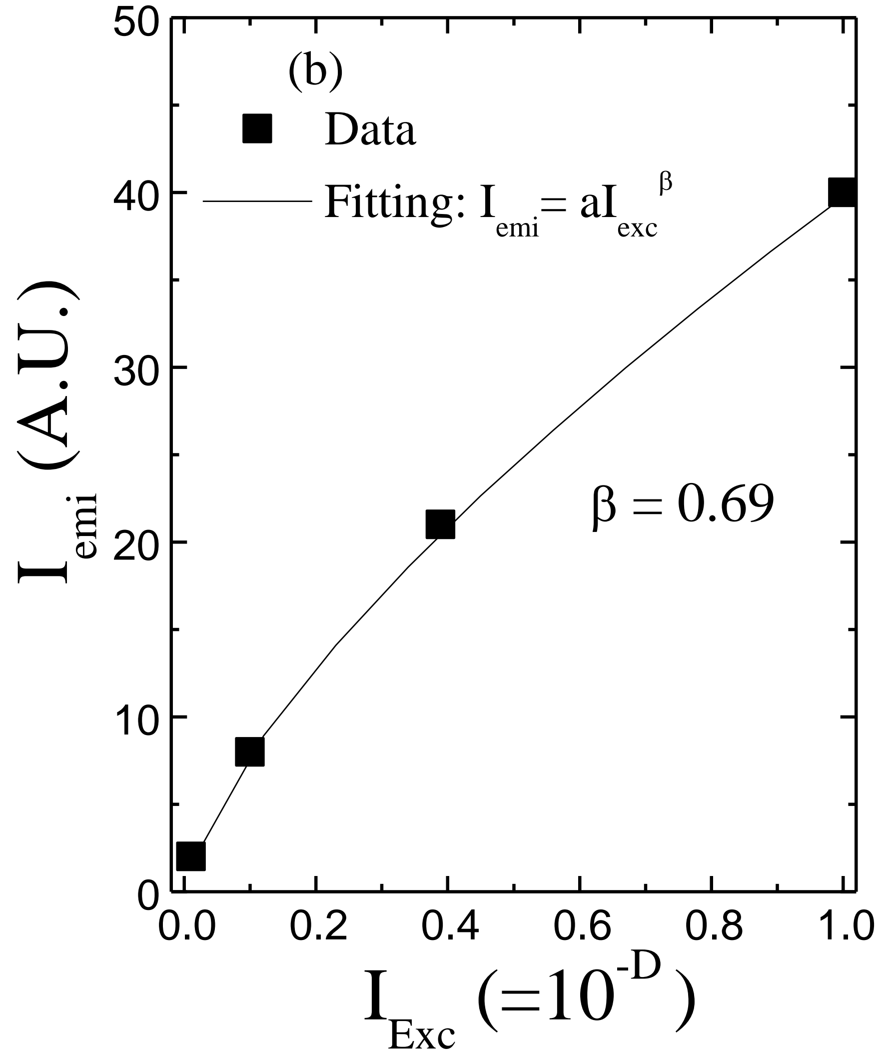

Fig. 3.17 (a) Excitation intensity dependent PL spectra measured on m-AlN bulk single crystal around 2.73 eV emission line with 197 nm excitation. (b) Peak emission intensity at 2.73 eV as a function of excitation intensity.

The proposed energy level diagram is shown in Fig. 3.19, which involves the levels introduced by both the charge states of $V_{Al}^{3-/2-}$; namely, a broad absorption band from 2.1 to 2.9 eV, and emission lines at ~2.78 and 3.2 eV. Upward and downward arrows indicate the

corresponding absorption and emission lines, respectively. The PL emission at 3.2 eV is a DAP type transition involving a shallow donor and a $V_{Al}^{3-/2-}$ deep acceptor, which is observed as a 3.4 eV line in actual measurement due to some Coulomb energy on the order of ~0.2 eV [44,45]. Note that the V_{Al}^{3-} state is unable to capture any more electrons and is only able to participate in the absorption process in which one of its electrons is excited to the conduction band or to the shallow donor to become V_{Al}^{2-}. For the absorption around 2.8 eV to happen, V_{Al} must be available in the V_{Al}^{2-} state. This absorption results in the excitation of electrons from the valence band to the V_{Al}^{2-} state and its transformation into a V_{Al}^{3-} state as illustrated in Fig. 3.18. All possible absorption and emission mechanisms involving the $V_{Al}^{3-/2-}$ deep center in AlN can be summarized in the following set of equations:

$V_{Al}^{2-} + h\nu = V_{Al}^{3-} + h^{+}$ (2.1-2.9 eV absorption responsible for yellow color), (3.8)

$V_{Al}^{3-} + h\nu = e^{-} + V_{Al}^{2-}$ (2.8-3.3 eV absorption from V_{Al}^{3-} to the conduction band), (3.9)

$D^{0} + V_{Al}^{2-} = V_{Al}^{3-} + D^{+} + h\nu$ (responsible for 3.4 eV PL emission), (3.10)

$V_{Al}^{3-} + h^{+} = V_{Al}^{2-} + h\nu$ (responsible for 2.78 eV PL emission) (3.11)

where D^{0} represents a shallow donor level.

The presence of oxygen impurities tends to create more V_{Al} as the formation energy (E_{form}) is reduced [41,130]. As more V_{Al}^{2-} states of $V_{Al}^{3-/2-}$ become available, optical absorption is more probable, as explained by Eq. (3.8) for 2.1 eV $\leq h\nu \leq$ 2.9 eV absorption and thus samples tend to appear more yellowish. After V_{Al}^{2-} state captures one more electron, it becomes V_{Al}^{3-} and the nearest neighbor lattice sites undergo a small inward relaxation compared to the V_{Al}^{2-} state, and gains some energy [41]. Based on the observed PL emission involving

the $V_{Al}^{3-/2-}$ level and the band-gap of AlN, we believe that the energy gained by this lattice relaxation is on the order of ~0.1 eV. As illustrated by Eqs. 3.8-3.11, electrons in the $V_{Al}^{3-/2-}$ levels can participate in either absorption or emission. When the electron in the V_{Al}^{3-} state recombines with a hole in the valence band, it becomes a V_{Al}^{2-} state by emitting a 2.78 eV photon, which is represented by Eq. (3.11). Again, the more oxygen is incorporated into the sample, the more V_{Al} form during the growth and hence the stronger the 2.78 eV emission. This was observed in the three samples studied here and is also in agreement with the previous observation of enhanced 2.71 and 2.88 eV peaks as oxygen concentration increases [131].

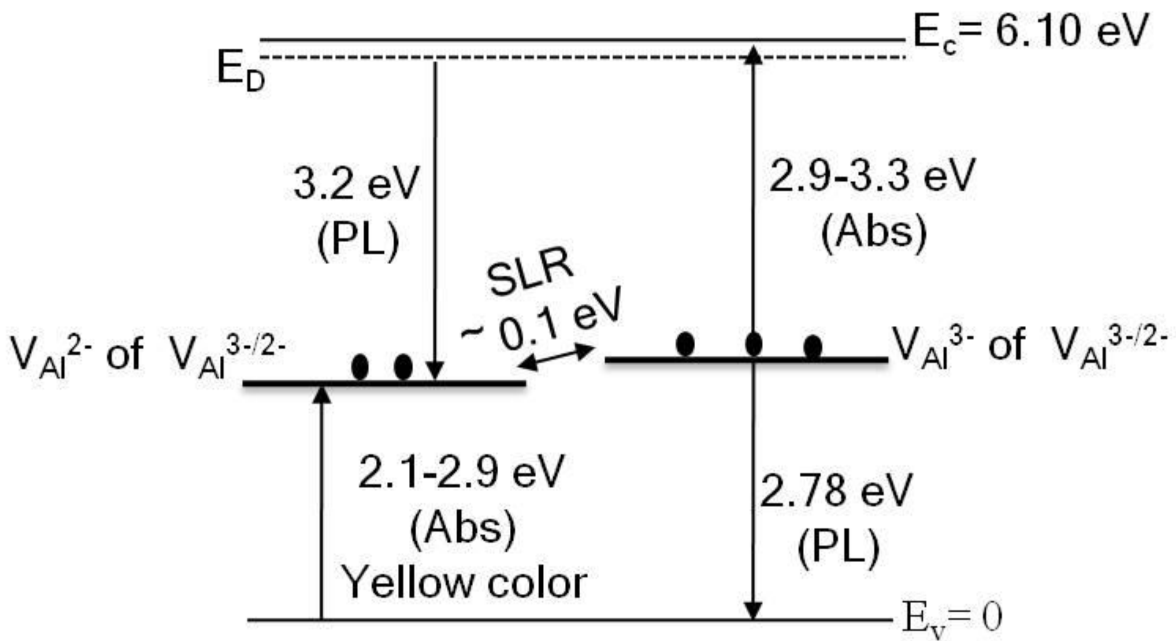

Fig. 3.18 Energy level diagram of AlN including two charge states, V_{Al}^{3-} and V_{Al}^{2-}, of $V_{Al}^{3-/2-}$ level with a small lattice relaxation (SLR) between these two states.

However, the situation will be different for AlN with higher concentrations of O impurities (~10^{19}–10^{20} cm^{-3}) (Refs. 117,127) than those of the samples we studied here (~10^{17}–10^{18} cm^{-3}). In the case of $[V_{Al}] \ll [O]$, no more isolated vacancies $V_{Al}^{3-/2-}$ will be available for the absorption process of Eq. (3.8) to occur. Instead, the oxygen atoms, which replace the N sites, form complexes with Al vacancies like $(V_{Al}–O_N)^{2-/1-}$ or $(V_{Al}–2O_N)^{1-/0}$. Thus, AlN materials with high O impurity concentrations in fact appear less yellow. This explanation is consistent with the previously reported results of transparent AlN, in which a $(V_{Al}–2O_N)^{1-}$ related absorption band around 4.7 eV emerged, while the 2.8 eV band completely disappeared in samples containing the highest oxygen concentrations (1.2×10^{21} cm^{-3}) [117,127].

In summary, we have carried out optical studies on different AlN samples by PL measurement to address the question of why bulk AlN crystals appear yellow in color. We propose that the absorption band centered around 2.8 eV, which corresponds to the excitation of electrons from the valence band to the V_{Al}^{2-} state of $(V_{Al})^{3-/2-}$, is responsible for the yellowish color of bulk AlN substrates. We observed a PL peak with a line width of ~0.3 eV at 2.78 (2.76) eV under below (above) band gap excitation, which we believe is caused by the recombination between electrons in the V_{Al}^{3-} state of the $(V_{Al})^{3-/2-}$ level and holes in the valence band. Understanding the origin of yellow coloration in bulk AlN will be crucial toward achieving high quality transparent bulk AlN substrate for III-nitride based optoelectronic devices.

3.6 Nature of deep center emissions in GaN

GaN materials are progressively becoming the most appropriate candidate for next generation lighting and other optoelectronic and electronic applications. The efficiency of GaN-based light-emitting diodes (LEDs) has been greatly improved and the GaN-based blue-violet laser with a lasing wavelength ~405 nm has already revolutionized optical data storage and readout capacity. Understanding the electronic and optical properties of GaN is imperative for improving the performance of GaN-based devices and for understanding the properties of InGaN and AlGaN ternary alloys, which have emerged as important semiconductor materials for applications in a wide spectral range-from infrared (IR) to deep ultraviolet.

There have been many reports on the structural, electrical, and optical properties of GaN materials and devices over the past two decades [2,132-136]. Studies on optical properties are mainly confined to band-edge emission and impurity bands in the visible spectral region. Among the impurity bands investigated, the yellow luminescence (YL) band in intentionally or unintentionally doped n-GaN is, by far, the most extensively studied. This band is believed to be a donor-acceptor-pair (DAP) type transition from a shallow donor to a deep acceptor. However, there are still controversies regarding the nature of the deep acceptor involved. Some of the earlier reports suggest the involvement of silicon on gallium site (Si_{Ga}) while others discussed possible involvement of carbon on nitrogen site (C_N) [41,137]. Based on the first principal calculations, positron annihilation, and doping experiments, it is now widely accepted that the deep acceptor is a complex consisting of a gallium vacancy and a nearest neighbor donor, namely an oxygen atom sitting on one of the neighboring nitrogen sites $(V_{Ga}–O_N)^{2-/1-}$ [41,44,45,138-143]. Additionally, deep levels around 1.2 eV were previously observed in different experiments [144-146] in n-GaN. A few other reports discussed a roughly 1.27 eV peak

that was observed due to the involvement of Mn [136,147]. However, the physical origin of the 1.23 eV emission and its possible connection with the YL band is not clear. In this work, we report on the observation of an emission line in the IR region (~1.23 eV) in GaN. Its physical mechanism and connection with the YL band is discussed.

GaN epilayers were grown on c-plane (0001) sapphire substrate by MOCVD. High crystalline quality of the material was confirmed with a narrow linewidth of (002) rocking curve from x-ray diffraction (300 arcsec). Hall measurements showed that the sample was n-type with a background electron concentration of 7×10^{16} cm^{-3} and mobility of 650 cm^2/V s. Atomic force microscopy revealed an atomically flat surface morphology with a roughness of 0.6 nm. Photoluminescence (PL) spectra were measured by exciting with a femtosecond laser, photon energy set at ~4.74 eV, which is a frequency tripled Ti-sapphire laser with a 76 MHz repetition rate [67].

The room temperature PL spectrum measured in the IR region is plotted in Fig. 3.19(a) from 0.9 to 1.5 eV. We observed a broad emission band with a peak at 1.23 eV. The emission peak energy is very close to values previously calculated by Neugebauer and Van de walle (1.1 eV) (Ref. 148) and Reynolds et al. (1.3 eV) (Ref. 149) for the electronic level of the gallium vacancy complex $(V_{Ga}–O_N)^{2-/1-}$ with respect to the top of the valence band (VB). The PL spectrum measured at 150 K in Fig. 3.19(b) consists of two well resolved peaks at 1.21 and 1.27 eV. The weak shoulder peak at 1.12 eV, which is about 90 meV below the 1.21 eV peak, is the LO phonon replica of the higher peak.

Based on the energy peak position, the 1.23 eV emission line in GaN may either be a band-to-impurity or a DAP transition. We measured the excitation intensity (I_{exc}) dependent PL spectra of this line. Figure 3.20(a) shows that the peak energy position stayed the same over two

orders of magnitude variation in I_{exc}. This indicates that the 1.23 eV band is a band-to-impurity type because the peak position of a DAP transition typically changes with I_{exc} since it is well known that the mean distance between DAPs and hence the emission wavelength decrease with I_{exc} [148]. Peak emission intensity, I_{emi}, at 1.23 eV as a function of I_{exc} is plotted in Fig. 3.20(b), where the solid squares denote the measured data. The solid line is the least square fit of the data with the equation of $I_{emi} = aI_{exc}^{\beta}$, where β is the fitting parameter, which was found to be 0.36.

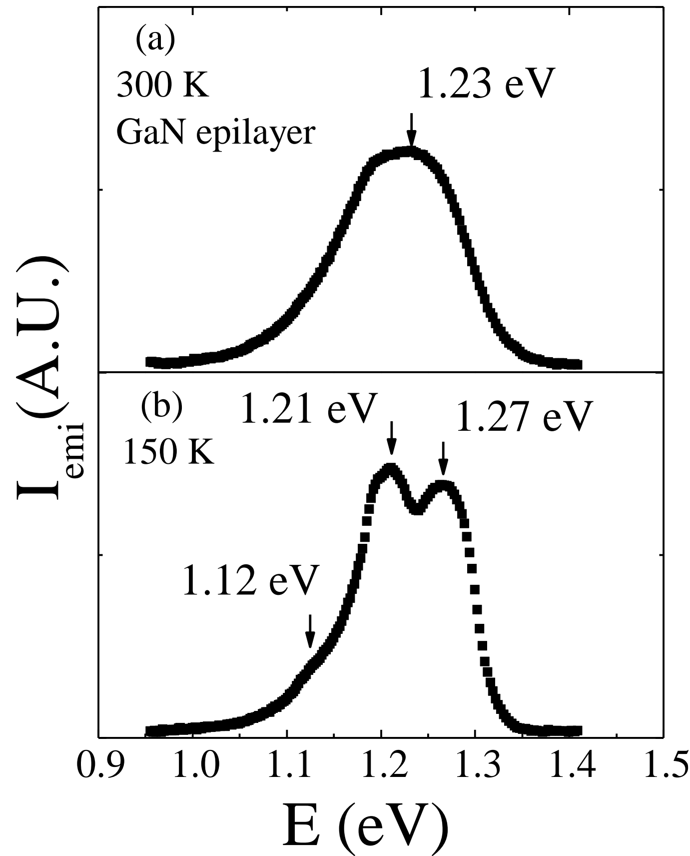

Fig. 3.19 (a) 300 K and (b) 150 K PL spectra of unintentionally doped n-GaN epilayer in the IR spectral region.

Room temperature PL spectra of the GaN epilayer in the visible region are shown in Fig. 3.21. The spectra consist of sharp and strong emission centered at 3.42 eV due to the band-to-band transition [151], as well as impurity transitions. The peak intensity of the band-edge related transition is more than 20 times stronger than that of impurity related transitions at 300 K, which reflects the high optical quality of the sample. The impurity part of the spectrum mainly shows two broad bands. The one centered around 2.85 eV is very weak and was previously identified as the blue luminescence band in GaN [136]. Like the IR PL spectrum shown in Fig. 3.19(b), we also observed two separate, clearly resolved emission lines within the single YL band. From

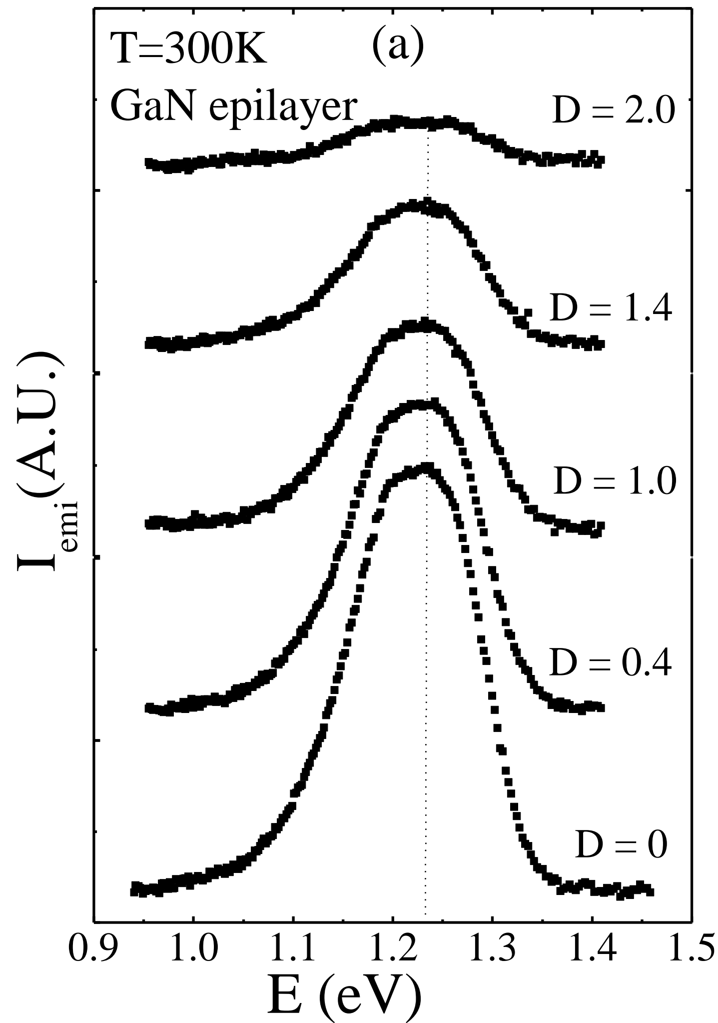

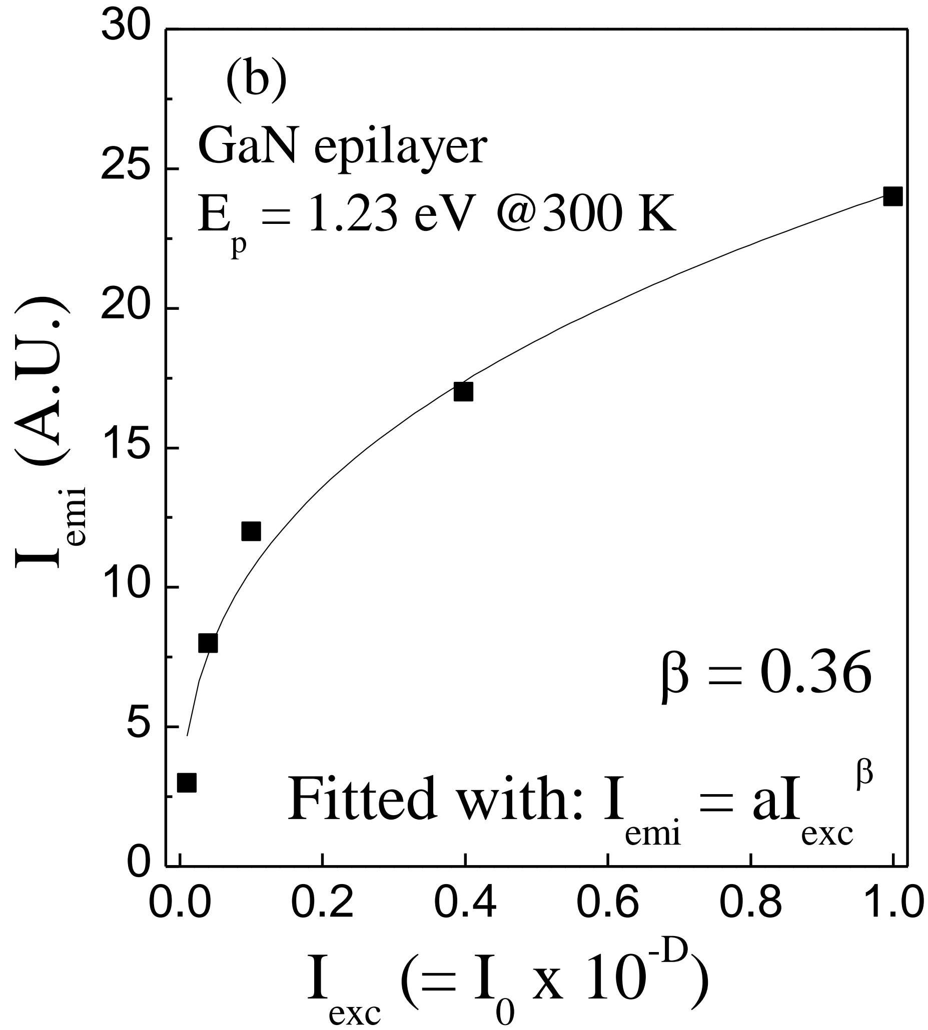

Fig. 3.20(a) Excitation intensity (I_{exc}) dependent PL spectra of GaN around 1.23 eV at 300 K and (b) PL emission intensity (I_{emi}) as a function of I_{exc} (solid squares) and least squares fit of data with $I_{emi} = aI_{exc}^{\beta}$ (solid line).

fitting, the peak positions of the two lines are at 2.13 and 2.30 eV. The energy difference between these two lines (0.17 eV) is close to the difference between the binding energies of $(V_{Ga}–O_N)^{2-/1-}$ for O replacing N from π- or σ-bonds (~0.16 eV) [152]. Because of the stable

wurtzite structure of GaN, two types of Ga–N bonds are distinguished: a longer single bond along the c-axis (π-bond) and three equivalent shorter bonds which make a very small angle with the basal plane (σ-bond). These bonds are about 1.9550 Å and 1.9486 Å, respectively [152]. Consequently, even with the same charge state, two geometries of the $(V_{Ga}–O_N)^{2-/1-}$ complex are possible. The oxygen atom may substitute the nitrogen from either the π- or σ-bond as illustrated

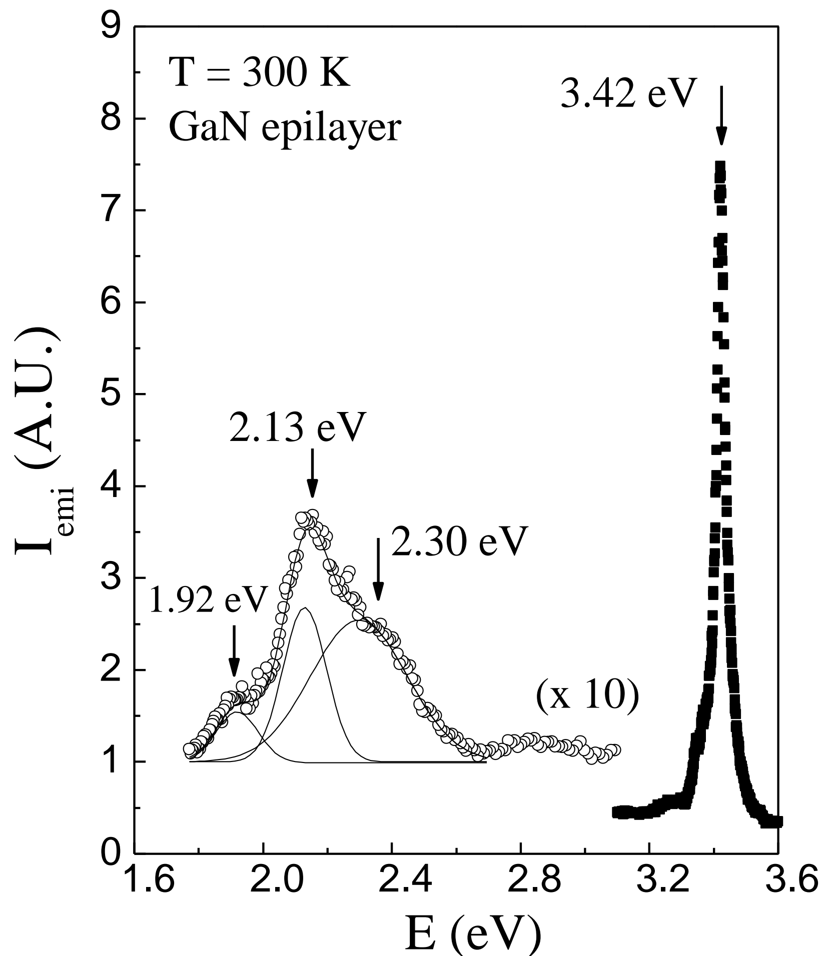

Fig. 3.21 Room temperature PL spectra of unintentionally doped n-GaN epilayer in UV and visible spectral regions.

in Fig. 3.22(a). Corresponding to those two configurations, $(V_{Ga}–O_N)^{2−/1−}$ possesses binding energies of different magnitudes, which offers two fine structures rather than a single level in the gap, giving rise to two emission lines. Relatively stronger intensity at the 2.13 eV branch indicates the availability of a higher population of σ-type complexes, which may be due to their larger binding energy (−2.01 eV for σ-bond versus −1.85 eV for π-bond) [148], and higher degeneracy. Several narrower peaks within the YL band with linewidths in the order of 0.1 eV were previously seen and are attributed to carrier-phonon interaction [153]. In most cases, these two lines are not well resolved due to broad linewidth.

The sum of the emission energies of the two lines in the YL band (2.13 and 2.30 eV) and the corresponding lines in the freshly observed IR band (1.27 and 1.21 eV) shown in Fig. 3.19

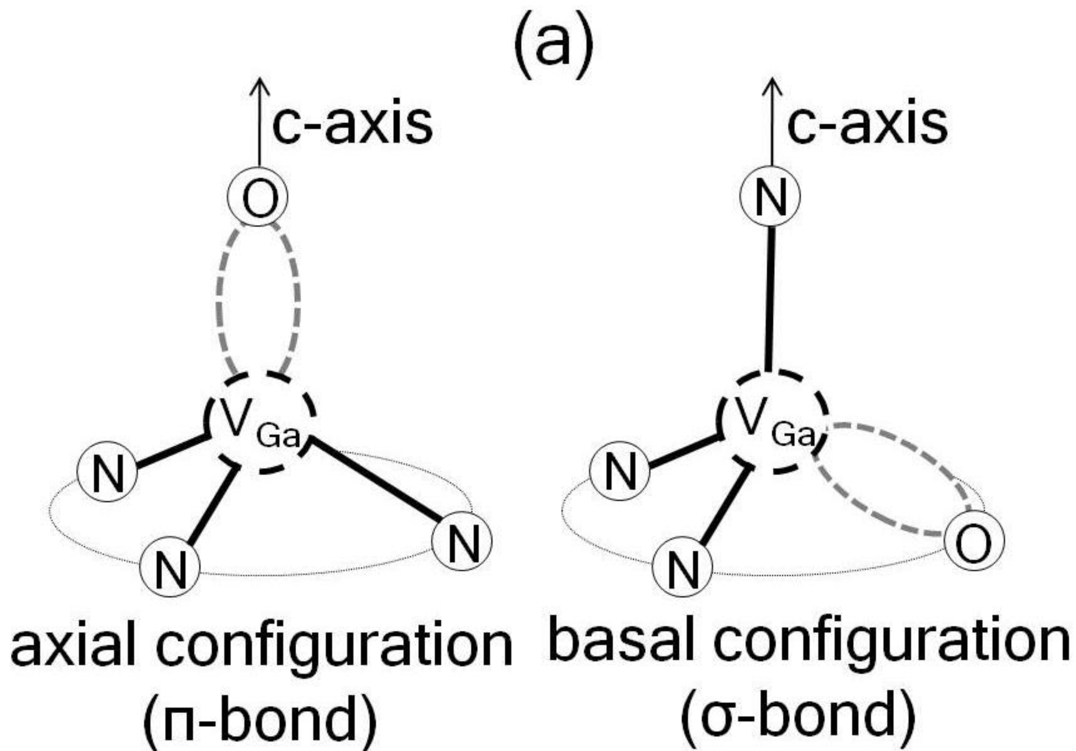

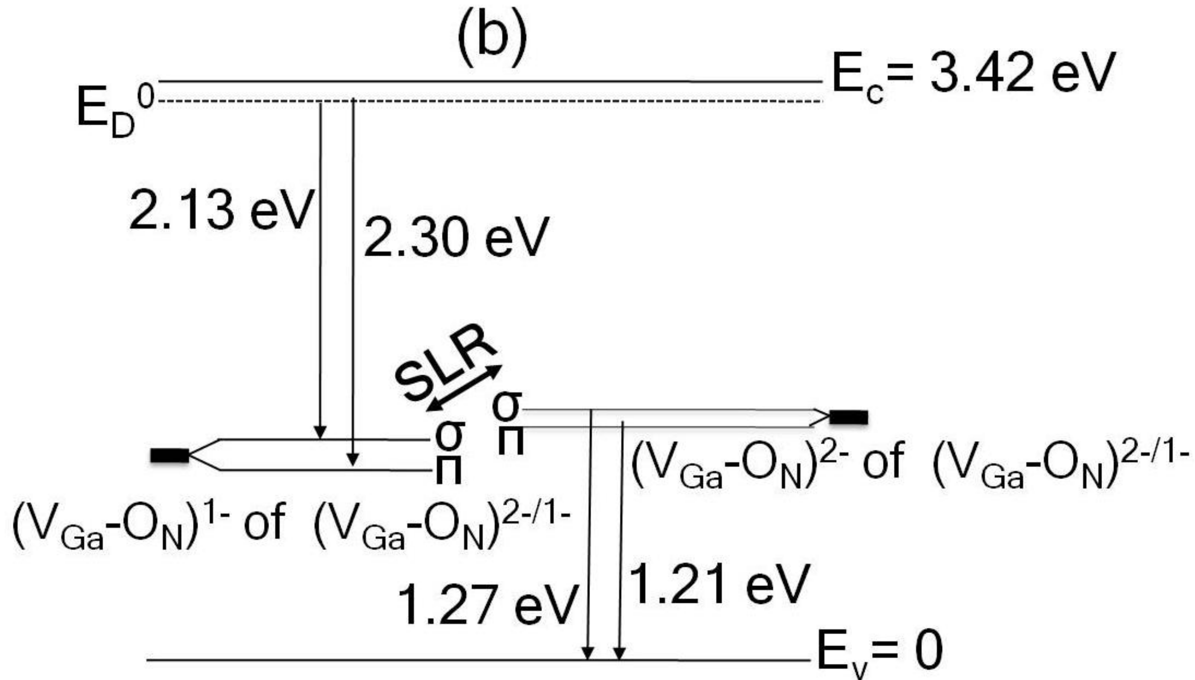

Fig. 3.22(a) Atomic geometries of the $(V_{Ga}\text{-}O_N)^{2-/1-}$ complex in GaN for oxygen replacing the nitrogen from (i) π-bonding (along c-axis) and (ii) σ-bonding (one of the other three equivalent positions). (b) Energy level diagram of GaN including the charge states $(V_{Ga}\text{-}O_N)^{2-}$ and $(V_{Ga}\text{-}O_N)^{1-}$ of $(V_{Ga}\text{-}O_N)^{2-/1-}$ center. SLR stands for small lattice relaxation.

are close to the energy gap of GaN. We suggest that the origin of the YL and IR bands share a common defect center in the gap. The involvement of the gallium vacancy complex $(V_{Ga}–O_N)^{2−/1−}$ in the YL band is a well established fact and the electronic level of $(V_{Ga}–O_N)^{2−/1−}$ has been reported to be around 1.1–1.3 eV (Refs. 148,149,153) from top of the VB. Therefore, we propose that the observed IR band is due to recombination between electrons in the $(V_{Ga}–O_N)^{2−}$ charge state of $(V_{Ga}–O_N)^{2−/1−}$ and holes in the VB. I_{exc}-dependent PL in Fig. 3.20 also supports the assignment that the IR band originates from a band-to-impurity type transition.

Figure 3.22(b) plots the energy levels for GaN at 300 K, featuring the shallow donor level (E_D^0) and the deep acceptor levels resulting from two charge states $(V_{Ga}–O_N)^{2−}$ and $(V_{Ga}–O_N)^{1−}$ of the gallium vacancy-oxygen impurity complex $(V_{Ga}–O_N)^{2−/1−}$. The energy level due to each charge state is further split into two fine structures due to Ga–N bond anisotropy. These structures are denoted by the π and σ configurations as shown in Fig. 3.22(a). The suggested mechanism of the two lines in the YL band (2.13 and 2.30 eV) can be described by the following equations:

$$D^0 + (V_{Ga}\text{-}O_N^{\sigma})^{1-} = D^+ + (V_{Ga}\text{-}O_N^{\sigma})^{2-} + h\nu \text{ (2.13 eV)} \quad (3.12)$$

$$D^0 + (V_{Ga}\text{-}O_N^{\pi})^{1-} = D^+ + (V_{Ga}\text{-}O_N^{\pi})^{2-} + h\nu \text{ (2.30 eV)} \quad (3.13)$$

where D^0 and D^+ denote shallow donors in the neutral and charged states, respectively. However, for the IR transitions (1.27 and 1.21 eV) to occur, we must have a significant population in the charge state of $(V_{Ga}–O_N)^{2−}$. Partial filling of the defect state $(V_{Ga}–O_N)^{2−/1−}$ during PL emission as illustrated in Eqs. 3.12 and 3.13 changes its charge state from $(V_{Ga}–O_N)^{1−}$ to $(V_{Ga}–O_N)^{2−}$. Consequently, the surrounding N and O_N atoms move inward [41,154] and gain some energy as shown in Fig. 3.22(b) [41]. Now the available $(V_{Ga}–O_N)^{2−}$ state can participate in the electron transition to the VB, giving 1.27 and 1.21 eV PL emissions as described by the followings:

$$(V_{Ga}\text{-}O_N^{\sigma})^{2-} + h^+ = (V_{Ga}\text{-}O_N^{\sigma})^{1-} + h\nu \text{ (1.27 eV)} \quad (3.14)$$

$$(V_{Ga}\text{-}O_N^{\pi})^{2-} + h^+ = (V_{Ga}\text{-}O_N^{\pi})^{1-} + h\nu \text{ (1.21 eV)} \quad (3.15)$$

In summary, high quality GaN epilayers were synthesized by MOCVD for studying the fundamental properties of deep center emissions. We observed an IR emission band with a peak at 1.23 eV due to the transition from $(V_{Ga}–O_N)^{2-}$ charge state of $(V_{Ga}–O_N)^{2-/1-}$ center to the VB. At lower temperatures (150 K), the IR band resolved into two lines, which correlate well with the two separate lines resolved within the YL band. Our results provide explicit evidence that both the YL band and the 1.23 eV line in GaN emission spectra are related to a common deep center, which is believed to be $(V_{Ga}–O_N)^{2-/1-}$.

Chapter 4 - General Conclusion

Optical properties of III-nitride epilayers, nanostructures, and bulk substrates were investigated by deep ultraviolet (DUV) time-resolved photoluminescence (PL) system. Continuous wave (CW) and time-resolved PL spectra and their temperature, excitation intensity (I_{exc}), and excitation photon energy dependence were investigated to extract the sample parameters.

The excitonic transitions related to all three valence bands (A, B, and C) were observed directly by polarization resolved PL studies of AlN. Valence band splitting parameters (crystal-field and spin-orbit splitting) of AlN were deduced from the observed excitonic emission energies using the Hopfield's quasicubic model for wurtzite crystals.

Optical properties of AlN homoepilayers in c-, a-, and m-plane orientations were investigated. These layers were found strain-free both from XRD and PL measurements. Impurity incorporation was less in m-plane growth mode. PL data demonstrated that emission from AlN homoepilayers in a-plane orientation was an order of magnitude stronger in bandedge region compared to c-homoepilayers, which is related to the enhanced light extraction due to the unique valence band structure of AlN. Photonic devices based on these homoepilayers with high crystalline quality has potential to deliver high efficiency and extended lifetime as the concentration of threading dislocation (TD) is reduced by several orders of magnitude in comparison to those in epilayers grown on foreign substrates.

The lacking of p-type AlN and Al-rich AlGaN alloys with reasonable free electron concentration impedes the implementation of III-nitride based UV and deep UV photonic devices in real practice. This is partly due to large activation energy of Mg, a universally accepted p-type dopant in III-nitrides. Theoretical investigations have suggested berrylium (Be)

to have lower activation energy in AlN than Mg. Be doped AlN epilayers were synthesized by MOCVD. Possibility of using Be as a p-type dopant in AlN has been studied experimentally by deep UV time-resolved photoluminescence. Our results from CW and time-resolved PL studies indicate that Be level in AlN is shallower than Mg level, which may be employed to partly address the p-type doing issue by increasing the room temperature free hole concentration.

Carrier-phonon interaction in III-nitride materials has been evaluated by Huang-Rhys factor, S, which measures the relative strength of excitonic emission lines and phonon-assisted lines observed in their PL spectra. Exciton-phonon interaction is quite strong in AlN and the strength differs significantly in two polarization configurations, $\vec{E} \perp \vec{c}$ and $\vec{E} \parallel \vec{c}$. Much stronger coopling in $\vec{E} \perp \vec{c}$ configuration than that in $\vec{E} \parallel \vec{c}$ configuration has been assigned to the much larger ratio of effective masses of hole to that of electron in $\vec{E} \perp \vec{c}$ configuration. When compared to GaN, the carrier-phonon coupling is much larger in AlN. Observation of stronger phonon replica in PL spectra has also been established as an indication of higher purity of the materials.

Although single crystal bulk AlN is substrate of choice for growing III-nitride UV and deep UV photonic devices, almost all sizeable bulk substrates appear yellow or dark amber in color. Mechanisms of undesired color in these materials have been investigated from optical studies. Absorption band starting around 2.0 eV with its maximum around 2.86 eV, which corresponds to the excitation of valence band electrons to the V_{Al}^{2-} charge state of isolated cation vacancy ($V_{Al}^{3-/2-}$), is found to be responsible for such yellow coloration. A nice correlation between concentration of oxygen impurities, degree of yellow coloration, and the intensity of 2.78 eV PL band was observed. Developing the growth recipe to avoid the formation of isolated

Al vacancies would be a critical step to achieve bulk AlN substrates with high VUV and DUV transparency.

Defects including the cation vacancies and their complexes with impurities [$V_{III}^{3-/2-}$, $(V_{III}\text{-}O_N)^{2-/1-}$ or $(V_{III}\text{-}2O_N)^{1-/0}$] can be formed in AlN and Al-rich AlGaN alloys in significantly high concentration to affect their properties due to low formation energies. These defects offer electronic states deep inside the bandgap. Understanding the optical and electrical properties of these defects is very critical in the development of AlGaN based DUV photonics. Optical transitions involving these defect levels and shallow donors (O or Si) were observed previously. In this thesis, a group of band-to-impurity transitions involving these deep level defects and the valence band have been discussed in the two extremes of AlGaN alloys. Corresponding to the different charge states of the deep centers, various transition lines were observed. In addition, taking the cation-anion bond anisotropy in directions parallel and perpendicular to the crystal c-direction into account, spectral lines related to each charge state of the deep centers (except $V_{Al}^{3-/2-}$) was further resolved into two fine structures, which were designated with π and σ, respectively.

References

1. J. Wu, W. Walukiewicz, K. M. Yu, J. W. Ager, E. E. Haller, H. Lu, W. J. Schaff, Y. Saito, and Y. Nanishi, Appl. Phys. Lett. **80**, 3967 (2002).
2. G. D. Chen, M. Smith, J. Y. Lin, H. X. Jiang, S. H. Wei, M. A. Khan, and C. J. Sun, Appl. Phys. Lett. **68**, 2784 (1996).
3. J. Li, K. B. Nam, M. L. Nakarmi, J. Li, J. Y. Lin, H. X. Jiang, P. Carrier, and S. H. Wei, Appl. Phys. Lett. **83**, 5163 (2003).
4. H. Amano, N. Sawaki, I. Akasaki, and Y. Toyoda, Appl. Phy. Lett. **48**, 353 (1985).
5. S. Nakamura, Jpn. J. Appl. Phys. **30**, L1705 (1991).
6. I. Akasaki and H. Amano, Jpn. J. Appl. Phys. **45**, 9001 (2006).
7. H. Amano, M. Kito, K. Hiramatsu and I. Akasaki, Jpn. J. Appl. Phys. **28**, L2112 (1989).
8. S. Nakamura, T. Mukai, M. Senoh and N. Iwasa, Jpn. J. Appl. Phys. **31**, L139 (1992).
9. H. X. Jiang and J. Y. Lin, in *AlN Epitaxial layers for UV Photonics*, edited by M. Razeghi and M. Henini, (Elsevier, 2004), Chapter 7.
10. A. Khan, K. Balakrishnan, and T. Katona, Nature Photonics **2**, 77 (2008).
11. C. Pernot, M. Kim, S. Fukahori, T. Inazu, T. Fujita, Y. Nagasawa, A. Hirano, M. Ippommatsu, M. Iwaya, S. Kamiyama, I. Akasaki, and H. Amano, Appl. Phys. Exp. **3**, 061004 (2010).
12. M. Kneissl, Z. Yang, M. Teepe, C. Knollenberg, O. Schmidt, P. Kiesel, N. M. Johnson, S. Schujman, and L. J. Schowalter, J. Appl. Phys. **101**, 123103 (2007).
13. S. G. Mueller, R. T. Bondokov, K. E. Morgan, G. A. Slack, S. B. Schujman, J. Grandusky, J. A. Smart, and L. J. Schowalter, Phys. Stat. Sol. (a) **206**, 1153 (2009).

14. K. Tsubouchi and N. Mikoshiba, IEEE Trans. Sonics and Ultrasonics **32**, 634 (1985).

15. F. Bernardini, V. Fiorentini, and D. Vanderbilt, Phys. Rev. B **56**, R10024 (1997).

16. F. Fichter, Z. Anorgan. Chem. **54**, 1, 322 (1907).

17. G. A. Slack, and T. F. McNelly, J. Cryst. Growth **34**, 263 (1977).

18. J. Li, K. B. Nam, M. L. Nakarmi, J. Y. Lin, and H. X. Jiang, Appl. Phys. Lett. **81**, 3365 (2002).

19. T. Onuma, K. Hazu, A. Uedono, T. Sota, and S. F. Chichibu, Appl. Phys. Lett. **96**, 061906 (2010).

20. H. Murotani, T. Kuronaka, Y. Yamada, T. Taguchi, N. Okada, and H. Amano, J. Appl. Phys, **105**, 083533 (2009).

21. R. Boger, M. Fiederle, L. Kirste, M. Maier, and J. Wagner, J. Phys. D **39**, 4616 (2006).

22. T. Ive, O. Brandt, H. Kostial, K. J. Friedland, L. D¨aweritz, and K. H. Ploog, Appl. Phys. Lett. **86**, 024106 (2005).

23. M. Hermann, F. Furtmayr, A. Bergmaier, G. Dollinger, M. Stutzmann, and M. Eickhof, Appl. Phys. Lett. **86**, 192108 (2005).

24. W. M. Yim, E. J. Stofko, P. J. Zanzucchi, J. I. Pankove, M. Ettenberg, and S. L. Gilbert J. Appl. Phys. **44**, 292 (1973).

25. X. Hu, J. Deng, J. P. Zhang, A. Lunev, Y. Bilenko, T. Katona, M. S. Shur, R. Gaska, M. Shatalov, and A. Khan, Phys. Stat. Sol. A **203**, 1815, (2006).

26. M. A. Khan, M. Shatalov, H. P. Maruska, H. M. Wang, and E. Kuokstis, Jpn. J. Appl. Phys. **44**, 7191 (2005).

27. H. Hirayama, Y. Tsukada, T. Maeda, and N. Kamata, Appl. Phys. Exp. **3**, 031002 (2010).

28. A. Fujioka, T. Misaki, T. Murayama, Y. Narukawa, and T. Mukai, Appl. Phys. Exp. **3**, 041001 (2010).

29. Y. Taniyasu and M. Kasu, Appl. Phys. Lett. **96**, 221110 (2010).

30. H. Tsuzuki, F. Mori, K. Takeda, M. Iwaya, S. Kamiyama, H. Amano, I. Akasaki, H. Yoshida, M. Kuwabara, Y. Yamashita, and H. Kan, J. Cryst. Growth **311**, 2860 (2009).

31. M. Shatalov, W. Sun, Y. Bilenko, A. Sattu, X. Hu, J. Deng, J. Yang, M. Shur, C. Moe, M. Wraback, and R. Gaska, Appl. Phys. Exp. **3**, 062101 (2010).

32. M. S. Shur and R. Gaska, Proc. of SPIE, Vol. 6894, 689419 (2008).

33. M. Albrecht, I. P. Nikitina, A. E. Nikolaev, Y. V. Melnik, V. A. Dmitriev, and H. P. Strunk, Phys. Stat. Sol. A **176**, 453 (1999).

34. A. Khan, S. Hwang, J. Lowder, V. Adivarahan, Q. Fareed, IEEE CFP09RPS-CDR 47th Annual International Reliability Physics Symposium, Montreal, 2009.

35. H. Amano, A. Miyazaki, K. Iida, T. Kawashima, M. Iwaya, S. Kamiyama, I. Akasaki, R. Liu, A. Bell, F. A. Ponce, S. Sahonta, and D. Cherns, Phys. Stat. Sol. A **201**, 2679 (2001).

36. K. X. Chen, Q. Dai, W. Lee, J. K. Kim, E. F. Schubert, J. Grandusky, M. Mendrick, X. Li, and J. A. Smart, Appl. Phys. Lett. **93**, 192108 (2008).

37. R. T. Bondokov, S. G. Mueller, K. E. Morgan, G. A. Slack, S. Schujman, M. C. Wood, J. A. Smart, and L. J. Schowalter, J. Cryst. Growth **310**, 4020 (2008).

38. Z. Ren, Q. Sun, S. Y. Kwon, J. Han, K. Davitt, Y. K. Song, A. V. Nurmikko, H.K. Cho, W. Liu, J. A. Smart, and L. J. Schowalter, Appl. Phys. Lett. **91**, 051116 (2007).

39. R. Gaska, C. Chen, J. Yang, E. Kuokstis, A. Khan, G. Tamulaitis, I. Yilmaz, M. S. Shur, J. C. Rojo and L. J. Schowalter, Appl. Phys. Lett. **81**, 4658 (2002).

40. S. A. Nikishin, B. A. Borisov, A. Chandolu, V. V. Kuryatkov, H. Temkin, M. Holtz, E. N. Mokhov, Y. Makarov, and H. Helava, Appl. Phys. Lett. **85**, 4355 (2004).

41. T. Mattila and R. M. Nieminen, Phys. Rev. B **55**, 9571 (1997).

42. S. F. Chichibu, T. Onuma, K. Hazu, and A. Uedono, Appl. Phys. Lett. **97**, 201904 (2010).

43. K. Irmscher, T. Schulz, M. Albrecht, C. Hartmann, J. Wollweber, and R. Fornari, Physica B 401, 323 (2007).

44. K. B. Nam, M. L. Nakarmi, J. Y. Lin, and H. X. Jiang, Appl. Phys. Lett. **86**, 222108 (2005).

45. N. Nepal, M. L. Nakarmi, J. Y. Lin, and H. X. Jiang, App. Phys. Lett. **89**, 092107 (2006).

46. A. Sedhain, L. Du, J. H. Edgar, J. Y. Lin, and H. X. Jiang, Appl. Phys. Lett. **95**, 262104 (2009).

47. A. Sedhain, J. Y. Lin, and H. X. Jiang, Appl. Phys. Lett. **96**, 151902 (2010).

48. K. B. Nam, M. L. Nakarmi, J. Y. Lin, and H. X. Jiang, Appl. Phys. Lett. **83**, 878 (2003).

49. C. G. Van de Walle and J. Neugebauer, J. Appl. Phys. **95**, 3851 (2004).

50. M. L. Nakarmi, K. H. Kim, M. Khizar, Z. Y. Fan, J. Y. Lin, and H. X. Jiang, Appl. Phys. Lett. **86**, 092108 (2005).

51. Y. Taniyasu, M. Kasu, and T. Makomoto, Nature **441**, 325 (2006).

52. A. Janotti, E. Snow, and C. G. Van de Walle, Appl. Phys. Lett. **95**, 172109 (2009).

53. B. A. Haskell, S. Nakamura, S. P. DenBaars, and J. S. Speck, Phys. Stat. Sol. B **244**, 2847 (2007).

54. M. C. Schmidt, K. C. Kim, H. Sato, N. Fellows, H. Masui, S. Nakamura, S. P. DenBaars, and J. S. Speck, Jpn. J. Appl. Phys. **46**, L126 (2007).

55. Krishnan Balakrishnan, Vinod Adivarahan, Qhalid Fareed, Mohamed Lachab, Bin Zhang, and Asif Khan, Jpn. J. Appl. Phys. **49**, 040206 (2010).

56. W. Becker, in *Advancd Time-Correlated Single Photon Counting Techniques*, (Springer Berlin, 2005).

57. S. H. Wei and A. Zunger, Appl. Phys. Lett. **69**, 2719 (1996).

58. P. Carrier and S. H. Wei, J. Appl. Phys. **97**, 033707 (2005).

59. G. I. M. Prinz, A. Ladenburger, M. Schirra, M. Feneberg, K. Thonke, R. Sauer, Y. Taniyasu, M. Kasu, and T. Makimoto, J. Appl. Phys. **101**, 023511 (2007).

60. L. Chen, B. J. Skromme, R. F. Dalmau, R. Schlesser, Z. Sitar, C. Chen, W. Sun, J. Yang, M. A. Khan, M. L. Nakarmi, J. Y. Lin, and H. X. Jiang, Appl. Phys. Lett. **85**, 4334 (2004).

61. E. Silveria, J. A. Freitas, Jr., O. J. Glembocki, G. A. Slack, and L. J. Schowalter, Phys. Rev. B **71**, 041201 (2005).

62. M. Suzuki, T. Uenoyama, and A. Yanase, Phys. Rev. B **52**, 8132 (1995).

63. C. Y. Yeh, Z. W. Lu, S. Froyen, and A. Zunger, Phys. Rev. B **46**, 10086 (1992).

64. K. B. Nam, J. Li, M. L. Nakarmi, J. Y. Lin, and H. X. Jiang, Appl. Phys. Lett. **84**, 5264 (2004).

65. B. N. Pantha, R. Dahal, M. L. Nakarmi, N. Nepal, J. Li, J. Y. Lin, H. X. Jiang, Q. S. Paduano, and D. Weyburne, Appl. Phys. Lett. **90**, 241101 (2007).

66. J. Li, Z. Y. Fan, R. Dahal, M. L. Nakarmi, J. Y. Lin, and H. X. Jiang, Appl. Phys. Lett. **89**, 213510 (2006).

67. http://www2.ece.ttu.edu/nanophotonics/

68. N. Nepal, M. L. Nakarmi, H. U. Jang, J. Y. Lin, and H. X. Jiang, Appl. Phys. Lett. **89**, 192111 (2006).

69. B. N. Pantha, N. Nepal, T. M. Al Tahtamouni, M. L. Nakarmi, J. Li, J. Y. Lin, and H. X. Jiang, Appl. Phys. Lett. **91**, 121117 (2007).

70. A. Wysmolek, M. Potemski, R. Stepniewski, J. Lusakowski, K. Pakula, J. M. Baranowski, G. Martinez, P. Wyder, I. Grzegory, and S. Porowski, Phys. Status Solidi A **216**, 11 (1999).

71. J. J. Hopfield, J. Phys. Chem. Solids **15**, 97 (1960).

72. B. Šantić, Semicond. Sci. Technol. **18**, 219 (2003).

73. K. Dovidenko, S. Oktyabrsky, J. Narayan, and M. Razeghi, J. Appl. Phys **79**, 2439 (1996).

74. R. Dahal, T. M. Al Tahtamouni, J. Y. Lin, and H. X. Jiang, Appl. Phys. Lett. **91**, 243503 (2007).

75. M. A. Khan, R. A. Skogman, J. M. Van Hove, S. Krishnankutty, and R. M. Kolbas, Appl. Phys. Lett. **56**, 1257 (1990).

76. S. Nakamura, T. Mukai, M. Senoh, S. Nagahama, and N. Iwasa, J. Appl. Phys. **74**, 3911 (1993).

77. F. A. Ponce and D. P. Bour, Nature London **386**, 351 (1997).

78. H. M. Ng, Appl. Phys. Lett. **80**, 4369 (2002).

79. T. M. Al Tahtamouni, A. Sedhain, J. Y. Lin, and H. X. Jiang, Appl. Phys. Lett. **90**, 221105 (2007).

80. T. J. Baker, B. A. Haskell, F. Wu, P. T. Fini, J. S. Speck, and S. Nakamura, Jpn. J. Appl. Phys. Part 2 **44**, L920 (2005).

81. Z. Gu, L. Du, J. H. Edgar, N. Nepal, J. Y. Lin, H. X. Jiang, and R. Witt, J. Cryst. Growth **297**, 105 (2006).

82. D. Zhang, J. H. Edgar, B. Liu, H. E. Huey, H. X. Jiang, J. Y. Lin, M. Kuball, F. Mogal, J. Chaudhuri, and Z. Rek, J. Cryst. Growth **262**, 89 (2004).

83. P. B. Perry and R. F. Rutz, Appl. Phys. Lett. **33**, 319 (1978).

84. M. Bickermann, B. M. Epelbaum, and A. Winnacker, Phys. Status Solidi C **0**, 7 (2003).

85. P. Lu, R. Collazo, R. Dalmau, X. Li, J. Tweedie, and Z. Sitar, MRS Symposia No. 1040E (Materials Research Society, Pittsburgh, 2007).

86. Z. Chen, R. S. Q. Fareed, M. Gaevski, V. Adivarahan, J. W. Yang, and A. Khan, Appl. Phys. Lett. **89**, 081905 (2006).

87. Y. Taniyasu, M. Kasu, and N. Kobayashi, Appl. Phys. Lett. **81**, 1255 (2002).

88. M. L. Nakarmi, K. H. Kim, K. Zhu, J. Y. Lin, and H. X. Jiang, Appl. Phys. Lett. **85**, 3769 (2004).

89. B. Borisov, V. Kuryatkov, Yu. Kudryavtsev, R. Asomoza, S. Nikishin, D. Y. Song, M. Holtz, and H. Temkin, Appl. Phys. Lett. **87**, 132106 (2005).

90. J. Li, T. N. Order, M. L. Nakarmi, J. Y. Lin, and H. X. Jiang, Appl. Phys. Lett. **80**, 1210 (2002).

91. T. Tanaka, A. Watanabe, H. Amano, Y. Kobayashi, I. Akasaki, S. Yamazaki, and M. Koike, Appl. Phys. Lett. **65**, 593 (1994).

92. M. L. Nakarmi, N. Nepal, C. Ugolini, T. M. Al Tahtamouni, J. Y. Lin, and H. X. Jiang, Appl. Phys. Lett. **89**, 152120 (2006).

93. R. Dahal, T. M. Al Tahtamouni, Z. Y. Fan, J. Y. Lin, and H. X. Jiang, Appl. Phys. Lett. **90**, 263505 (2007).

94. F. Mireles and S. E. Ulloa, Phys. Rev. B **58**, 3879 (1998).

95. R. Q. Wu, L. Shen, M. Yang, Z. D. Sha, Y. Q. Cai, Y. P. Feng, Z. G. Huang, and Q. Y. Wu, Appl. Phys. Lett. **91**, 152110 (2007).

96. N. Nepal, M. L. Nakarmi, K. B. Nam, J. Y. Lin, and H. X. Jiang, Appl. Phys. Lett. **85**, 71 (2004).

97. J. R. Haynes, Phys. Rev. Lett. **4**, 361 (1960).

98. E. I. Rashba and G. E. Gurgenishvili, Fiz. Tverd. Tela (Leningrad) **4**, 1029 (1962); Sov. Phys. Solid State **4**, 759 (1962).

99. R. A. Mair, J. Li, S. K. Duan, J. Y. Lin, and H. X. Jiang, Appl. Phys. Lett. **74**, 513 (1999).

100. K. B. Nam, J. Li, M. L. Nakarmi, J. Y. Lin, and H. X. Jiang, Appl. Phys. Lett. **82**, 1694 (2003).

101. M. Horita, J. Suda, and T. Kimoto, Appl. Phys. Lett. **89**, 112117 (2006).

102. A. BenMoussa, J. F. Hochedez, R. Dahal, J. Li, J. Y. Lin, H. X. Jiang, A. Soltani, and J.-C. De Jaeger, Appl. Phys. Lett. **92**, 022108 (2008).

103. X. B. Zhang, T. Taliercio, S. Kolliakos, and P. Lefebvre, J. Phys.:Condens. Matter **13**, 7053 (2001).

104. L. Bergman, M. Dutta, C. Balkas, R. F. Davis, J. A. Christman, D. Alexson, and R. J. Nemanich, J. Appl. Phys. **85**, 3535 (1999).

105. G. Popovici, G. Y. Xu, A. Botchkarev, W. Kim, H. Tang, A. Salvador, H. Morkoc¸ R. Strange, and J. O. White, J. Appl. Phys. **82**, 4020 (1997).

106. D. C. Raynolds, D. C. Look, B. Jogai, and R. J. Molnar, Solid State Commun. **108**, 49 (1998).

107. M. Smith, J. Y. Lin, H. X. Jiang, A. Khan, Q. Chen, A. Salvador, A. Botchkarev, W. Kim, and H. Morkoc, Appl. Phys. Lett. **70**, 2882 (1997).

108. N. Nepal, K. B. Nam, M. L. Nakarmi, J. Y. Lin, H. X. Jiang, J. M. Zavada, and R. G. Wilson, Appl. Phys. Lett. **84**, 1090 (2004).

109. B. Di Bartolo and R. Powell, *Phonons and Resonances in Solids* (Wiley, New York, 1976), Chap. 10.

110. K. W. Böer, *Survey of Semiconductor Physics* (Van Nostrand Reinhold, New York, 1990), Chap. 20.

111. H. Zhao and H. Kalt, Phys. Rev. B **68**, 125309 (2003).

112. H. L. Malm and R. R. Haering, Can. J. Phys. **49**, 2970 (1971).

113. D. L. Dexter and R. S. Knox, *Excitons* (Interscience, New York, 1965), pp. 52–54.

114. W. Liu, M. F. Li, S. J. Xu, K. Uchida, and K. Matsumoto, Semicond. Sci. Technol. **13**, 769 (1998).

115. G. Steude, B. K. Meyer, A. Göldner, A. Hoffmann, F. Bertram, and J. Christen, Appl. Phys. Lett. **74**, 2456 (1999).

116. H. Morkoc, *Nitride Semiconductors and Devices* (Springer, New York, 1999).

117. A. Sedhain, N. Nepal, M. L. Nakarmi, T. M. Al Tahtamouni, J. Y. Lin, H. X. Jiang, Z. Gu, and J. H. Edgar, Appl. Phys. Lett. **93**, 041905 (2008).

118. I. A. Buyanova, J. P. Bergman, B. Monemar, H. Amano, and I. Akasaki, Mater. Sci. Eng., B **50**, 130 (1997).

119. H. Y. An, O. H. Cha, J. H. Kim, G. M. Yang, K. Y. Lim, E. K. Suh, and H. J. Lee, J. Appl. Phys. **85**, 2888 (1999).

120. M. Sumiya, T. Ohnishi, M. Tanaka, A. Ohtomo, M. Kawasaki, M. Yoshimoto, H. Koinuma, K. Ohtsuka, and S. Fuke, Mater. Res. Soc. Symp. Proc. **537**, G623 (1999).

121. M. Tanaka, S. Nakahata, K. Sogabe, H. Nakata, and M. Tobioka, Jpn. J. Appl. Phys, Part 2 **36**, L1062 (1997).

122. R. Schlesser and Z. Sitar, J. Cryst. Growth **234**, 349 (2002).

123. V. Noveski, R. Schlesser, B. Raghothamachar, M. Dudley, S. Mahajan, S. Beaudoin, and Z. Sitar, J. Cryst. Growth **279**, 13 (2005).

124. Y. N. Makarov, O. V. Avdeev, I. S. Barash, D. S. Bazarevskiy, T. Y. Chemekova, E. N. Mokhov, S. S. Nagalyuk, A. D. Roenkov, A. S. Segal, Y. A. Vodakov, M. G. Ramm, S. Davis, G. Huminic, and H. Helava, J. Cryst. Growth **310**, 881 (2008).

125. J. C. Rojo, L. J. Schowalter, R. Gaska, M. Shur, M. A. Khan, J. Yang, and D. D. Koleske, J. Cryst. Growth **240**, 508 (2002).

126. J. C. Rojo, L. J. Schowalter, G. Slack, K. Morgan, J. Barani, S. Schujman, S. Biswas, B. Raghothamachar, M. Dudley, M. Shur, R. Gaska, N. M. Johnson, and M. Kneissl, *MRS Symposia Proceedings* No. 722, K1.1 (Materials Research Society, Pittsburgh, 2002).

127. G. A. Slack, L. J. Schowalter, D. Morelli, and J. A. Freitas, Jr., J. Cryst. Growth **246**, 287 (2002).

128. M. Bickermann, B. M. Epelbaum, and A. Winnacker, J. Cryst. Growth **269**, 432 (2004).

129. D. Bimberg, M. Sondergeld, and E. Grobe, Phys. Rev. B **4**, 3451 (1971).

130. C. Stampfl and C. G. Van de Walle, Phys. Rev. B **65**, 155212 (2002).

131. M. Morita, K. Tsubouchi, and N. Mikoshiba, Jpn. J. Appl. Phys., Part 1 **21**, 1102 (1982).

132. S. Nakamura and G. Fasol, *The Blue Laser Diode: GaN Based Light Emitters and Lasers* (Springer, Berlin, 1997).

133. J. I. Pankove and J. A. Hutchby, J. Appl. Phys. **47**, 5387 (1976.

134. S. Nagahama, N. Iwasa, M. Senoh, T. Matsushita, Y. Sugimoto, H. Kiyoku, T. Kozaki, M. Sano, H. Matsumura, H. Umemoto, K. Chocho, T. Yanamoto, and T. Mukai, Phys. Status Solidi A **188**, 1 (2001).

135. L. Liu and J. H. Edgar, Mater. Sci. Eng. R **37**, 61 (2002).

136. M. A. Reshchikov and H. Morkoç, J. Appl. Phys. **97**, 061301 (2005.

137. T. Ogino and M. Aoki, Jpn. J. Appl. Phys., Part 1 **19**, 2395 (1980).

138. S. Limpijumnong and C. G. Van de Walle, Phys. Rev. B **69**, 035207 (2004).

139. I. Gorczyca, N. E. Christensen, and A. Svane, Phys. Rev. B **66**, 075210 (2002).

140. K. Saarinen, T. Laine, S. Kuisma, J. Nissilä, P. Hautojärvi, L. Dobrzynski, J. M. Baranowski, K. Pakula, R. Stepniewski, M. Wojdak, A. Wysmolek, T. Suski, M. Leszczynski, I. Grzegory, and S. Porowski, Phys. Rev. Lett. **79**, 3030 (1997).

141. J. Oila, V. Ranki, J. Kivioja, K. Saarinen, P. Hautojärvi, J. Likonen, J. M. Baranowski, K. Pakula, T. Suski, M. Leszczynski, and I. Grzegory, Phys. Rev. B **63**, 045205 (2001).

142. A. Uedono, S. F. Chichibu, Z. Q. Chen, M. Sumiya, R. Suzuki, T. Ohdaira, and T. Mikado, J. Appl. Phys. **90**, 181 (2001).

143. K. Saarinen, V. Ranki, T. Suski, M. Bockowski, and I. Grzegory, J. Cryst. Growth **246**, 281 (2002).

144. W. Götz, N. M. Johnson, R. A. Street, H. Amano, and I. Akasaki, Appl. Phys. Lett. **66**, 1340 (1995).

145. G. C. Yi and B. W. Wessels, Appl. Phys. Lett. **68**, 3769 (1996).

146. I. Shalish, L. Kronik, G. Segal, Y. Rosenwaks, Y. Shapira, U. Tisch, and J. Salzman, Phys. Rev. B **59**, 9748 (1999).

147. R. Y. Korotkov, J. M. Gregie, and B. W. Wessels, *GaN and Related Alloys*, MRS Symposia Proceedings No. 639 (Materials Research Society, Pittsburgh, 2000), p. G3.7.

148. J. Neugebauer and C. G. Van de Walle, Appl. Phys. Lett. **69**, 503 (1996).

149. J. Jenny, R. Jones, J. E. Van Nostrand, D. C. Reynolds, D. C. Look, and B. Jogai, Solid State Commun. **106**, 701 (1998).

150. D. G. Thomas, J. J. Hopfield, and W. M. Augustyniak, Phys. Rev. **140**, A202 (1965).

152. M. Smith, J. Y. Lin, H. X. Jiang, and M. A. Khan, Appl. Phys. Lett. **71**, 635 (1997.

152. K. Lawniczak-Jablonska, T. Suski, I. Gorczyca, N. E. Christensen, K. E. Attenkofer, R. C. C. Perera, E. M. Gullikson, J. H. Underwood, D. L. Ederer, and Z. L. Weber, Phys. Rev. B **61**, 16623 (2000).

153. J. S. Colton, P. Y. Yu, K. L. Teo, E. R. Weber, P. Perlin, I. Grzegory, and K. Uchida, Appl. Phys. Lett. **75**, 3273 (1999).

154. J. Neugebauer and C. G. Van de Walle, Phys. Rev. B **50**, 8067 (1994).

Appendix A - Publications

1. ***A. Sedhain***, J. Li, J. Y. Lin, and H. X. Jiang, "Nature of deep center emission in GaN", Appl. Phys. Lett. **96**, 151902 (2010)
2. B. Pantha, ***A. Sedhain***, J. Li, J. Y. Lin, H. X. Jiang, "Probing the relationship between structural and Optical Properties of Si-doped AlN", Appl. Phys. Lett. **96**, 131906 (2010)
3. I. W. Feng, J. Li, ***A. Sedhain***, J. Y. Lin, H. X. Jiang, and J. Zavada, "Enhancing erbium emission by strain engineering in GaN heteroepitaxial layers", Appl. Phys. Lett. **96**, 031908 (2010)
4. ***A. Sedhain***, L. Du, J. H. Edgar, J. Y. Lin, and H. X. Jiang, "The origin of 2.78 eV emission and yellow coloration in bulk AlN substrates", Appl. Phys. Lett. **95**, 262104 (2009)
5. B. Pantha, J. Li, ***A. Sedhain***, J. Y. Lin, H. X. Jiang, "Electrical and Optical Properties of p-type InGaN", Appl. Phys. Lett. **95**, 261904 (2009)
6. ***A. Sedhain***, J. Li, J. Y. Lin, and H. X. Jiang, "Probing exciton-phonon interaction in AlN epilayers by photoluminescence", Appl. Phys. Lett. **95**, 061106 (2009)
7. ***A. Sedhain***, C. Ugolini, J. Y. Lin, H. X. Jiang, and J. M. Zavada, "Photoluminescence properties of erbium doped InGaN epilayers", Appl. Phys. Lett. **95**, 041113 (2009)
8. N. Nepal, J. M. Zavada, R. Dahal, C. Ugolini, ***A. Sedhain***, J. Y. Lin, and H. X. Jiang, "Optical enhancement of room temperature ferromagnetism in Er-doped GaN epilayers", Appl. Phys. Lett. **95**, 022510 (2009)
9. N. Nepal, J. M. Zavada, D. S. Lee, A. J. Steckl, ***A. Sedhain***, J. Y. Lin, and H. X. Jiang, "Deep UV photoluminescence of Tm-doped AlGaN alloys", Appl. Phys. Lett. **94**, 111103 (2009)

10 ***A. Sedhain***, T. M. Al Tahtamouni, J. Li,1 J. Y. Lin, and H. X. Jiang “Beryllium acceptor binding energy in AlN”, Appl. Phys. Lett. **93**, 141104 (2008)

11 J. Liu, J. Li, ***A. Sedhain***, J. Lin, and H. X. Jiang,”Structure and Photoluminescence Study of TiO2 Nanoneedle Texture along Vertically Aligned Carbon Nanofiber Arrays”, The Journal of Physical Chemistry C **112**, 17127 (2008)

12 ***A. Sedhain***, N. Nepal, M. L. Nakarmi, T. M. Al Tahtamouni, J. Li, J. Y. Lin, and H. X. Jiang, Z. Gu, and J. H. Edgar “Photoluminescence properties of AlN homoepilayers with different orientations”, Appl. Phys. Lett. **93**, 041905 (2008)

13 N. Khan, ***A. Sedhain***, J. Li, J. Y. Lin, and H. X. Jiang, “High mobility InN epilayers grown on AlN epilayer templates”, Appl. Phys. Lett. **92**, 172101 (2008)

14 T. M. Al Tahtamouni, ***A. Sedhain***, J. Y. Lin, and H. X. Jiang, “Growth and optical properties of a-plane AlN and Al-rich AlN/AlxGa1-xN quantum wells grown on r-plane sapphire substrates”, Phys. Stat. Sol. C **5**, 1568 (2008)

15 T. M. Al tahtamouni, ***A. Sedhain***, J. Y. Lin, and H. X. Jiang, "Si-doped high Al-content AlGaN epilayers with improved quality and conductivity using indium as a surfactant", Appl. Phys. Lett. **92**, 092105 (2008)

16 ***A. Sedhain***, J. Y. Lin, and H. X. Jiang, “Valence band structure of AlN probed by photoluminescence”, Appl. Phys. Lett. **92**, 041114 (2008)

17 N. Khan, N. Nepal, ***A. Sedhain***, J. Y. Lin, and H. X. Jiang, “Mg acceptor level in InN epilayers probed by photoluminescence”, Appl. Phys. Lett. **91**, 012101 (2007)

18 T. M. Al Tahtamouni, ***A. Sedhain***, J. Y. Lin, and H. X. Jiang, “Growth and photoluminescence studies of a-plane AlN/AlxGa1−xN quantum wells”, Appl. Phys. Lett. **90**, 221105 (2007)

19 X. H. Ji, S. P. Lau, S. F. Yu, H. Y. Yang, T. S. Herng, ***A. Sedhain***, J. Y. Lin, H. X. Jiang, K. S. Teng, and J. S. Chen, "Ultraviolet photoluminescence from ferromagnetic Fe-doped AlN nanorods," Appl. Phys. Lett. **90**, 193118 (2007

Book Chapter

"AlN–Properties and Applications" ***A. Sedhain***, J. Y. Lin, and H. X. Jiang, Chapter – 2 in "*Handbook of Photoluminescent Semiconductor Materials*" Leah Bergman and Jeanne McHale, Taylor & Francis Group, LLC (In Press)